

Design and implementation of a fs-Transmission Electron Microscope for time-resolved studies of strongly correlated systems and nanostructures

THÈSE N° 6601 (2015)

PRÉSENTÉE LE 17 AVRIL 2015

À LA FACULTÉ DES SCIENCES DE BASE

LABORATOIRE POUR LA MICROSCOPIE ET LA DIFFUSION D'ÉLECTRONS

PROGRAMME DOCTORAL EN CHIMIE ET GÉNIE CHIMIQUE

ÉCOLE POLYTECHNIQUE FÉDÉRALE DE LAUSANNE

POUR L'OBTENTION DU GRADE DE DOCTEUR ÈS SCIENCES

PAR

Luca PIAZZA

acceptée sur proposition du jury:

Prof. A.-C. Corminboeuf, présidente du jury

Prof. F. Carbone, directeur de thèse

Prof. B. E. Barwick, rapporteur

Prof. K. Kern, rapporteur

Prof. J. Weissenrieder, rapporteur



ÉCOLE POLYTECHNIQUE
FÉDÉRALE DE LAUSANNE

Suisse
2015

— *The world is moving so fast these days
that the man who says it can't be done
is generally interrupted by someone doing it* —

Elbert Hubbard

Acknowledgements

I would like to express my special appreciation and thanks to my advisor Professor Fabrizio Carbone, for his constant support during these four years and for constantly encouraging my research and my personal growth.

I would also like to thank Professor Clémence Corminboeuf, Professor Klaus Kern, Professor Brett Barwick and Professor Jonas Weissenrieder for serving as my committee members.

In such little time it wouldn't have been possible for me to obtain the results that appear now published without the contribution of a large group of people with which I have collaborated. It's impossible to name all of them but I'm certainly proud to have shared the laboratory in particular with Professor Barwick, Dr. LaGrange and Dr. Reed. The possibility to interact with them and have access to their advice has been priceless.

Last but not least I would like to thank my colleagues and friends who shared with me this intense period of time.

Lausanne, 13 Mars 2015

L. P.

Contents

Acknowledgements	5
Abstract	11
Introduction	15
Outline	18
1 fs-Transmission Electron Microscopy	21
The fs-TEM components	24
Performances in pulsed mode	25
Temporal resolution	29
Conclusions	32
2 Ultrafast diffraction and EELS	39
The sample and the experimental setup	44
<i>in-situ</i> static measurement	44

Contents

Ultrafast electron diffraction	46
Ultrafast EELS	48
Discussion of the results	51
Conclusions	54
3 Photo-induced near-field electron microscopy	59
Photons and electrons team up	60
Energy-momentum conservation	63
Quantization and the interference of a plasmonic near-field	66
SPP imaging	67
Plasmonic nanoresonators	71
Experimental estimate of Planck's constant	74
Energy-space SPP mapping	75
Sample preparation	81
Experimental apparatus	81
Finite-element simulations	84
4 Perspectives in ultrafast electron microscopy	91
The electron microscope components	91
Proposal for a high-energy excitation in solids.	95
Introduction	95

Contents

The role of the excitation in time-resolved experiments.	98
Quantitative analysis of an X-ray pump-TEM probe experiment	102
Conclusions	110
Conclusions	119
Curriculum vitae	123

Abstract

The integration of ultrafast laser systems with transmission electron microscopes led to the extension of conventional electron microscopy to the 4th dimension, time, and new techniques as photo-induced near-field electron microscopy became available.

This novel class of instruments offers to the experimenter the possibility to apply in one single instrument different and complementary ultrafast techniques as imaging, electron diffraction and energy-loss spectroscopy, allowing the investigation of the properties of matter with renovated efficiency obtaining time-resolved informations of both structural and electronic structures.

In this thesis we report the design and implementation of the world-first ultrafast electron microscope based on a thermionic gun and we characterize the performances of the machine.

Strongly correlated electron materials are an optimal playground for this instrument, the challenge being the ability to decouple the several degrees of freedom characterized by similar energy scale. We applied ultrafast diffraction and electron energy loss spectroscopy to the study of the metallic phase of a layered manganite, and we study the electronic and lattice response to a femtosecond photo-excitation.

Taking advantage of the capabilities of PINEM to visualize electromagnetic fields at the ultrafast timescale we report the first simultaneous observation of the particle-like and wave-like behavior of a plasmon-polariton confined

Abstract

on the surface of a silver nanowire.

Finally we present a discussion about the possible evolution of ultrafast electron microscopy, analyzing the feasibility of the integration of an ultrafast-transmission electron microscope with a free electron laser for performing high-energy excitations in solids.

Keywords

Ultrafast electron microscopy

Ultrafast diffraction

Ultrafast spectroscopy

Strongly correlated materials

Nanoplasmonics

Sommario

L'integrazione tra laser ultraveloci e microscopi elettronici a trasmissione ha portato all'estensione della microscopia elettronica convenzionale nella quarta dimensione, quella temporale, e alla nascita di nuove tecniche sperimentali quali la microscopia elettronica di campo evanescente foto-indotto (photo-induced near-field electron microscopy, PINEM).

Questa nuova classe di sistemi offre allo sperimentatore in un singolo strumento l'accesso a differenti tecniche ultraveloci complementari tra loro quali l'acquisizione di immagini, la diffrazione di elettroni e la spettroscopia elettronica a perdita di energia, agevolando notevolmente lo studio delle proprietà della materia e offrendo la possibilità di ottenere informazioni sulle dinamiche sia della struttura cristallina che di quella elettronica del campione.

In questa tesi riportiamo l'implementazione del primo microscopio elettronico ultraveloce al mondo basato su una sorgente termoionica e la caratterizzazione delle sue prestazioni.

I materiali fortemente correlati sono un ottimo campo di prova per questo strumento. L'obiettivo sperimentale è quello di riuscire a disaccoppiare i diversi gradi di libertà del sistema, compito reso complesso dal fatto che molti di essi sono caratterizzati da energie simili. La spettroscopia elettronica ultraveloce e la diffrazione di elettroni sono state applicate allo studio della fase metallica di un composto di manganite ed è stata studiata la risposta

Sommario

elettronica e reticolare ad uno stimolo luminoso ultrabreve.

Visto che la tecnica PINEM è in grado di visualizzare campi elettromagnetici in una scala temporale ultraveloce, riportiamo inoltre la prima osservazione simultanea del comportamento ondulatorio e corpuscolare di un plasmone-polarone confinato sulla superficie di un nanofilo di argento.

Infine, presentiamo una discussione sulla possibile evoluzione della microscopia elettronica ultraveloce, analizzando la possibilità di integrare un microscopio elettronico ultraveloce ed un laser ad elettroni liberi per stimolare eccitazioni ad alta energia in campioni solidi.

Parole chiave

Microscopia elettronica ultraveloce

Diffrazione ultraveloce

Spettroscopia ultraveloce

Materiali fortemente correlati

Nanoplasmonica

Introduction

Walking through the historical path of the technology-driven human society it is noticeable that to every improvement to the ability “to see” and analyze clearer nature’s details corresponds a scientific revolution that gradually influences collective consciousness drive improvements to living standards.

During the transition between medieval and modern era the astronomic revolution represents one of the most important steps in the direction of modern society. At the beginning of the seventeenth century, Galileo Galilei (Pisa, 1564-1642) optimized the design of the telescope and posed the basics for a cultural revolution that concerned all of the European continent. His scientific results have been inherited by Isaac Newton (London, 1643-1727) that, between the other things, laid the foundations of modern optics and invented the reflecting telescope whose scheme is still used today in the most important astronomical observation facilities.

Aside from the observation of big and distant objects, the magnification properties of well-designed lens systems endorsed the study of the sub-millimeter world, disclosing details about nature inaccessible to the limited resolution power of human eye. In 1665 Robert Hooke in his work *Micrographia* first described a copious amount of details about microscopic living creatures and introduced the word “cell” to describe what in his understanding represented the basic component of vegetable life structures. At the same time, the dutch Antonie van Leeuwenhoek was the first to visualize elements like bacteria, blood flow in capillaries and muscle fibers, posing the foundations of micro-

Introduction

biology.

The precision in the production of optical components grew rapidly and at the beginning of the 20th century the resolving power of optical microscopes was already close to their theoretical value, limited by diffraction effects governed by the wavelength of visible light.

During the revolution stimulated by the discovery of quantum mechanics the idea introduced by Louis De Broglie that an electron had an associated wavelength of the order of picometer suggested that such a particle could be used to overcome the limits of optical microscopy.

In their seminal work in 1933, Max Knoll and Ernst Ruska [1] described the electron microscope they first conceived. It represented a big technological leap forward in the field and in few years what was a simple laboratory prototype became a successful commercial product capable unveiling details in the nanometer scale and whose design remains conceptually unchanged until nowadays.

The 1986 Nobel's price in Physics is the seal on half century of success leading to several declinations of modern electron microscopes that have applications in different fields, from biology to material science, from medicine to physics, to nanotechnology.

In its evolution the increased performances of the electron optical elements and the electron sources grew alongside the research for better devices able to register the informations collected from the samples. The need for ever increasing performances of these devices was justified to reduce the exposure times to limit the irradiation damage of the samples and avoid degradation of the data due to mechanical instabilities of the machine, critical for high resolution applications.

Since early times the possibility of acquiring shorter and shorter snapshots of the specimen has been supported by the interest in observing not only static images but also the evolution of the properties of the specimen itself

after some dynamical process had been initiated. Many designs for sample holders today allow the interaction with the specimen applying light, electric and magnetic fields, controlling its temperature, its pressure and observing its behavior in gaseous or liquid environments.

The first approach for obtaining fast acquisition times involved the research for efficient and sensitive acquisition devices able to record signal in short amounts of time. Nowadays electronic sensors used for delicate biological samples in cryo-microscopy are able to reach the microsecond timescale [2].

For even shorter time scales is necessary a different approach, following the steps of ultrafast laser optics. The main idea is to not reduce the acquisition time of the sensor but to deliver to it a packet of informations relative to a precise instant in the time evolution of some process stimulated in the sample. For applying this idea in electron microscopes, conventional continuous-wave electron sources had to be rethought in order to produce a pulsed electron beam.

The evolution in this field dates back several decades [3, 4, 5, 6] but recently the popularity increased drastically thanks to the evolution of stable ultrafast laser sources, pushing the technology of time-resolved microscopy from the domain of μs down until the sub-ps regime.

The work reported in this thesis has been accomplished at the LUMES laboratory at the Polytechnique Fédérale de Lausanne (EPFL) and has been the base for the following publications:

- *Principles and Implementation of an Ultrafast Transmission Electron Microscope*, **L. Piazza**, M. Cottet, D.J. Masiel, T. LaGrange and F. Carbone, Proceedings of Microscopy & Microanalysis, 18 (Suppl 2), 2012
- *Design and implementation of a fs-resolved transmission electron microscope based on thermionic gun technology*, **L. Piazza**, D.J. Masiel,

Introduction

T. LaGrange, B.W. Reed, B. Barwick, F. Carbone, Chemical Physics, 423 7984, 2013

- *Ultrafast structural and electronic dynamics of the metallic phase in a layered manganite* **L. Piazza**, C. Ma, H. X. Yang, A. Mann, Y. Zhou, J. Q. Li, F. Carbone, Structural Dynamics, 1 014501, 2014
- *A proposal for fs-electron microscopy experiments on high-energy excitations in solids*, **L. Piazza**, P. Musumeci, O.J. Luiten, F. Carbone, Micron, 63 4046, 2014
- *Simultaneous observation of the quantization and the interference pattern of a plasmonic near-field*, **L. Piazza**, T.T.A. Lummen, E. Quinonez, Y. Murooka, B.W. Reed, B. Barwick, F. Carbone, Nature Communications 6, 6407 (2015).

Outline

The outline of the thesis is the following:

- In Chapter 1 we present the description of the time-resolved ultrafast electron microscope installed in the LUMES laboratory at the cole Polytechnique Fdrale de Lausanne (EPFL) and the characterization of its performances.
- In Chapter 2 we describe the results of the study on a strongly correlated material, layered manganites, performed via ultrafast electron diffraction and ultrafast electron energy loss spectroscopy.
- In Chapter 3 we present the simultaneous observation of particle-like and wave-like behavior of surface plasmon polaritons on silver nanowires, obtained by photo-induced nearfield electron microscopy.

- In Chapter 4 some perspectives on the future evolution of the hardware of an ultrafast electron microscope are presented, together with the scientific study for a proposal for an hybrid instrument obtained coupling fs-TEM with an X-ray free electron laser beamline.

References

- [1] M Knoll and E Ruska. “Das Elektronenmikroskop”. In: *Zeitschrift für Physik* 78.5-6 (1932), pp. 318–339.
- [2] <http://www.gatan.com/products/tem-imaging-spectroscopy/k2-camera>.
- [3] G V Spivak, O P Pavlyuchenko, and V I Petrov. “Electron microscopic observation of alterations of the domain structure of magnetic films”. In: *Bulletin of the Academy of Sciences of the USSR Physical Series* 30 (1966), pp. 822–826.
- [4] A Takaoka and Ura Katsumi. “Stroboscopic TEM with time resolution of 30 μ s”. In: *Journal of electron microscopy* (1983).
- [5] O Bostanjoglo et al. “Nanosecond electron microscopes”. In: *Ultramicroscopy* 81.3-4 (2000), pp. 141–147.
- [6] Wayne E King et al. “Ultrafast electron microscopy in materials science, biology, and chemistry”. In: *Journal of applied physics* 97.11 (2005), p. 111101.

Chapter 1

fs-Transmission Electron Microscopy

The extension of transmission electron microscopy to the fourth dimension, time, has taken several steps to reach the ns to fs resolution domain [1, 2, 3, 4, 5], proving to be dramatically effective in the investigation of light induced phenomena in a variety of systems [6, 7, 8, 9, 10, 11] and spanning areas of research like physical chemistry [12, 13], biophysics [14], nanophotonics [15], condensed matter physics [16] and materials science [17, 18]. Unlike a conventional TEM, high time resolution electron microscopes take advantage of laser generated ultrashort pulses of electrons to probe the specimen. To achieve femtosecond time resolution with the low energy spread desired for real-space imaging, the simplest technique is to allow each electron pulse to contain at most one electron [19]. This requirement imposes the use of a very low average current in the TEM, thus sacrificing signal in order to obtain the best possible spatial and temporal coherence.

Currently, there are two main approaches to time resolved electron mi-

Parts of this chapter are taken from *Design and implementation of a fs-resolved transmission electron microscope based on thermionic gun technology*, L. Piazza *et al*, Chemical Physics, 423 7984, 2013.

croscopy: femtosecond ultrafast electron microscopy (UEM) which uses stroboscopic “single” electron pulses to study ultrafast dynamics [19, 20] and the dynamic transmission electron microscope (DTEM) which uses electron pulses containing more than 10^8 electrons to acquire “single-shot” images with nanosecond exposure times [17, 21, 22]. This letter focuses on a new microscope that is optimized for operation in the femtosecond mode, or UEM, that utilizes a combination of a thermionic source with a Wehnelt and an extra condenser lens. In fs-resolved machines, it is important to keep the current density very low to avoid the temporal broadening of the electron pulses during propagation due to space charge. In this low current or “single” electron regime, the average beam current is a few orders of magnitude lower when compared to the conventional continuous wave (CW) electron beam in thermionic mode. For example, when operating at 1 MHz with 1 ps electron pulses, a current is present in the microscope only for 1 μ s out of every second. This greatly decreases the signal that is available for imaging, diffraction or spectroscopy. Unfortunately, the increase in the electron energy spread and pulse duration, caused by space charge and Boersch effects, happens at the source and in the accelerator section, where the electrons are moving relatively slowly.

In a standard TEM design, the current throughput between the gun and the sample is typically only a few percent at most (and often much less). Thus if an average pulse has a single electron when it reaches the sample, very likely it had tens or even hundreds to thousands of electrons when it was emitted, and the presence of these unused electrons may substantially worsen the time and energy resolution. To optimize the performance in fs mode, two things must be done: (1) adjust the conditions at the electron gun so that it only emits a small excess of electrons beyond those that are used to form an image or spectrum and (2) modify the condenser lens system to capture a very large fraction of the emitted electrons. To satisfy the first task, we systematically vary the laser pulse energy, laser pulse duration and the bias voltage on the Wehnelt electrode (which, for a thermionic source, acts as a feedback-stabilized electron focusing and suppression optical element).

As we vary these parameters, we measure the signal level, pulse duration, and energy spread in order to understand how to optimize performance for any given experiment. To do the second, we add a large, weakly focusing condenser lens, called the C0 lens since it precedes the standard C1 condenser lens, similarly to the design described in [23].

The Wehnelt is an electrostatic lens which works by decelerating, then re-accelerating the electron beam while it is still at a very low energy, greatly increasing dispersion. Any electrostatic lens in the upper regions of the accelerator would similarly tend to degrade the pulse duration. Whereas the C0 lens is a magnetic lens operating on the fully accelerated beam and thereby has much less detrimental effects on the pulse duration. The C0 lens is crucial for the operation of the Wehnelt based UEM, because, as we show below, the shortest duration electron pulses are obtained with zero or low Wehnelt bias; this in turn does not efficiently couple the electrons down the column, which dramatically reduces the electron counts.

The C0 lens is used to get a majority of the electrons that exit the accelerator to reach the sample, thus recovering the signal lost because of the Wehnelt settings. Moreover, ad hoc combinations of electron-pulse duration and coherence can be achieved by independently controlling the Wehnelt and C0 voltages. In fact, since brightness is conserved, signal increases at the expense of spatial coherence and hence can reduce spatial resolution. It should be mentioned as well that in previous reports describing the C0 lens operation with nanosecond electron pulses the primary advantage was its ability to increase current for single shot imaging; in the application reported here, this lens's primary use is to prevent space-charge effects in the gun region by providing a combination of electron-collection and acceleration that optimizes the duration and energy spread of fs-electron bunches. As we shall show below, the impact of such a modification on the performance in static imaging mode is minimal. With this modified system, we show that few-hundred-fs time resolution can be achieved with sufficient electron counts for imaging, diffraction, and EELS.

This approach delivers similar results to a UEM with a modified FEG module which uses the extractor and suppressor lens system to control the emission properties of the photo-current; here, we show that in our microscope the simpler combination of the Wehnelt and C0 allows the direct control of electron pulse duration and beam current. This ability allows the microscope to be optimized for the demands of each experiment. It has to be noted that conventional field-emission guns come with voltage controllers that often forbid independent tuning of the extractor/suppressor lenses, resulting in a somewhat limited tunability of the instrument [20].

The fs-TEM components

The femtosecond laser used in the setup is a "KMLabs Wyvern X" Ti:Sapph amplified laser pumped by three Finesse CW green pump lasers for a total maximum pump power of about 40 W. It delivers 5 W of average power at 800 nm wavelength, 80 fs pulse duration, and repetition rates between 200 kHz and 2 MHz. The beam is split into two paths: one is frequency tripled to generate the UV probe beam, while the other is used to pump the specimen. The laser pulses are sent to the microscope to allow fs time-resolved electron microscopy (dynamical) operation. The microscope is a modified JEOL 2100 TEM with a Gatan Quantum GIF electron energy loss spectrometer (EELS). Two optical ports have been added to the microscope, two mirrors have been placed inside the column and an additional magnetic lens has been placed between the acceleration region and the C1 lens. The upper optical window located in an additional column section allows the UV (266 nm) laser pulses to enter the microscope, where it is reflected on a movable holed aluminum mirror. After the UV is reflected up the column it hits a 30 μm flat LaB₆ tip, creating electron pulses through the photoelectric effect. A second optical window located near the specimen allows an additional laser beam to enter the column, where it hits a mirror that is placed on the top of the objective lens pole-piece. This second laser beam after reflection on the mirror

is focused onto the specimen. The additional C0 magnetic lens allows the electrons to be more efficiently coupled down the column. A schematic of the modification is presented in Figure 1.1. In the right panel of Figure 1.1 two high-resolution images taken in thermionic emission mode before (top) and after (bottom) the modification are shown. After the modification, a slight blurring is visible towards the edges of the image, resulting in a slightly lower spatial resolution. However, lattice fringes are visible in both images proving that the modification itself only has a minor impact on the conventional performance of the TEM. When the C0 lens voltage is increased, an increased electron intensity is achieved at the expense of the spatial resolution. Also, for dynamical operation a 30 μm flat LaB₆ tip is used instead of the standard conic one, also resulting in a somewhat reduced spatial resolution. For these reasons, in a realistic time-resolved experiment, a spatial resolution around 1 nm is to be expected. It is important to stress at this point that in time-resolved experiments the overall final spatial resolution does not depend solely on the imaging capability of the microscope but also on the mechanical response of the sample to the exciting pulses and the possible photo-emitted charge present on its surface [24, 25].

Performances in pulsed mode

While the microscope can be operated in thermionic mode, where it gives performances similar to a standard machine, we will focus here on its operation in femtosecond pulsed mode operation. The two parameters that require optimization while in femtosecond pulsed mode are total current and the energy resolution (width of the zero loss peak (ZLP)). One important characteristic of the JEOL 2100 TEM is that the voltage on the Wehnelt can be adjusted directly and does not rely on the feedback current provided by the electron beam. That is, there is a static bias voltage continuously applied to the Wehnelt that can be independently varied, which is crucial for optimizing pulsed electron parameters. This voltage can be adjusted from

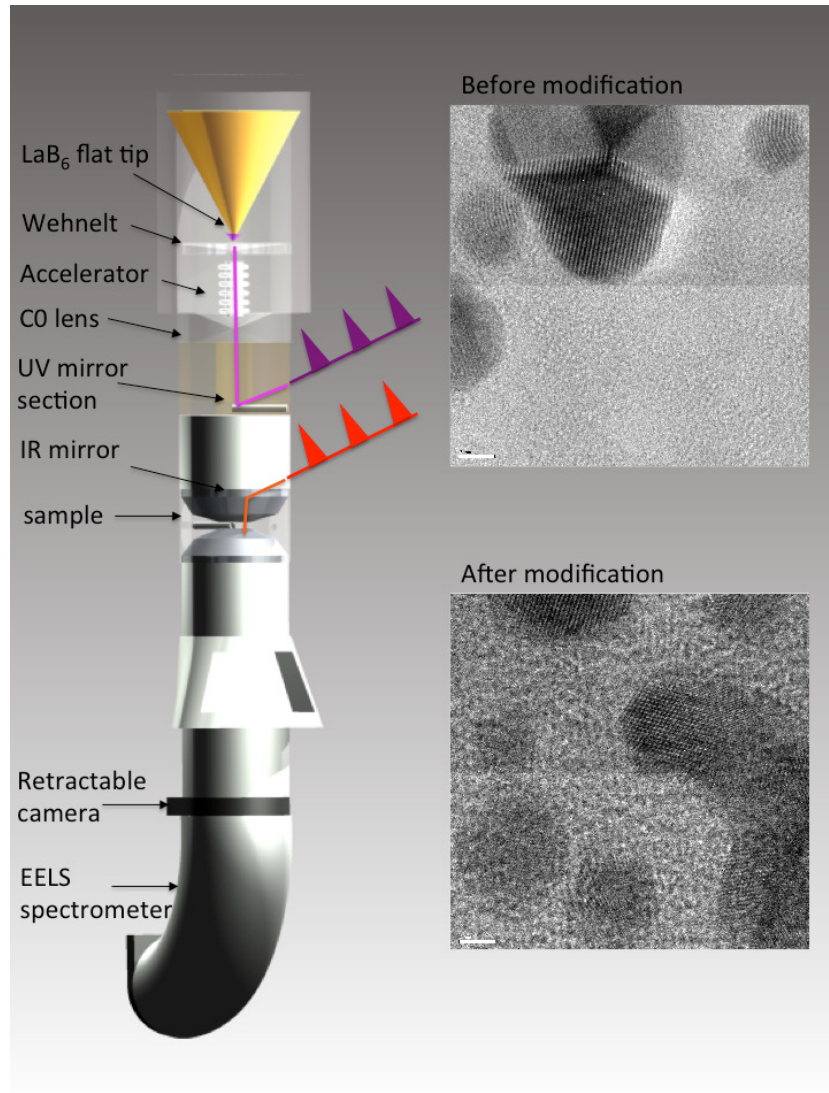


Figure 1.1: Modified TEM: the critical sections where conventional parts have been modified are transparent. In the right panel a static atomic resolution image taken on a gold nano-particle TEM resolution standard is shown before and after the modification of the instrument. Image adapted from [26].

around 0 V to roughly 1000 V, even with the emission current equal to zero, and the change in this voltage when the filament emits in thermionic mode is relatively small. The characteristic response time of the resistive feedback is much longer than the photo-emitted pulse duration. When a high bias voltage is used on the Wehnelt, electrons emitted from the center of the tip are selected and coupled down the column. This typically results in better beam coherence and lower energy spread in the ZLP, but because the Wehnelt voltage tends to decelerate the electrons at the cathode, the pulse suffers from space-charge effects, resulting in longer pulses. On the contrary, if very low or no bias voltage is applied to the Wehnelt, electrons from a larger region of the cathode are accepted, the energy spread of the ZLP is larger and the coherence of the beam is lower, but electron pulses with durations of a few hundred fs can be obtained (as will be shown in Figure 1.4). In Figure 1.2, the effect of the bias voltage on the beam properties is visible. In all the experiments the strength of the C0 lens is kept at its optimal value to maximize counts. The UV beam from the laser is directed to the cathode via a 1 m focal length optical lens. The spot-size at the LaB₆ tip is estimated to be between 100 and 150 μm in diameter. The repetition-rate of these experiments was 1 MHz. In Figure 1.2 A, the electron counts as a function of the UV power used to photo-emit electrons from the cathode are shown; a 0 V bias on the Wehnelt lens was set. An image of the tip is taken for different UV power values, top panels of Figure 1.2. The electron counts are estimated on the detector by integrating the intensity of all the pixels in the images and then converting pixel counts to electron counts. At low UV power, the electron counts are found to increase linearly with the laser power as expected for the photoelectric effect. However, a saturation in the counts is observed beyond 150 electrons/pulse on the detector. It is interesting to notice that above 1 mW of illuminating UV power, corresponding to approximately 30 electrons per pulse, the image of the tip becomes blurred (Figure 1.2 A and central top panel), and the energy width of the ZL peak begins to significantly broaden, Figure 1.2 B. The width in energy of the ZL peak displayed as a function of the UV power for two different Wehnelt bias voltages also shows a divergence beyond 1 mW of UV power for the 0 V bias

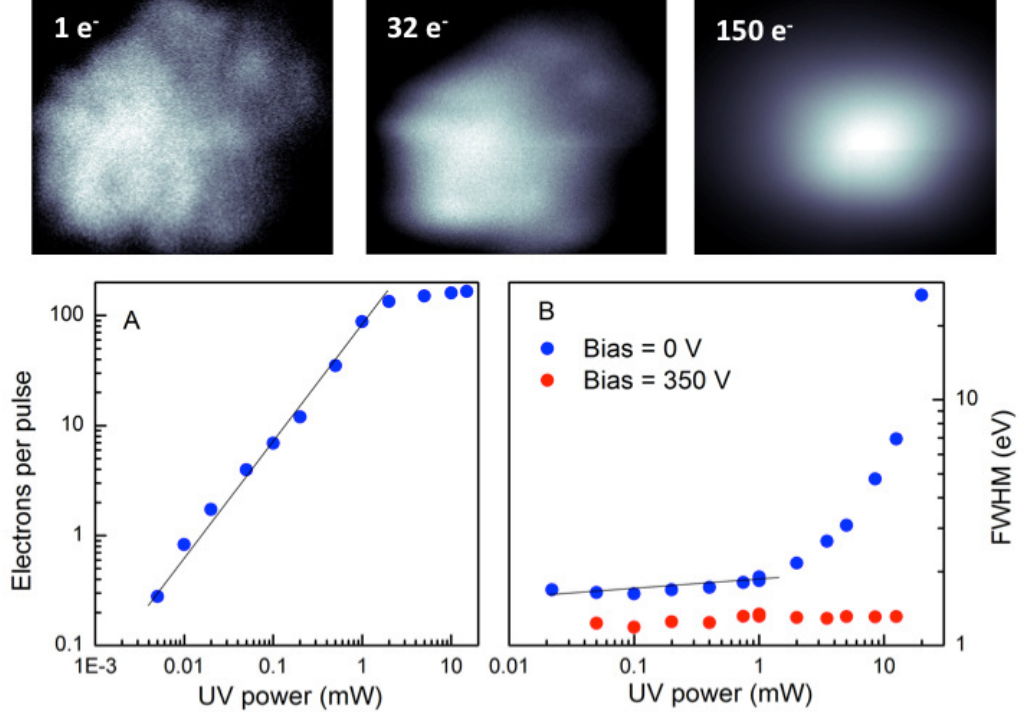


Figure 1.2: A. Beam current as a function of UV power. B. Dependence of the FWHM of the ZL peak on the UV power for two different Wehnelt bias voltages. In the top panels of the figure, the images of the tip taken for three different illuminating UV powers are shown. Image adapted from [26].

setting. At higher UV power, the width of the ZL becomes several eV, and the image of the tip becomes a cloud of charge with no details distinguishable (Figure 1.2, top right panel), testifying to the abrupt onset of space-charge effects already at very low currents.

It is interesting to notice that for a high voltage on the Wehnelt (350 V, Figure 1.2 B), a higher number of electrons in the pulses does not result in a broader energy distribution. This suggests, and will be verified below, that the electron pulses have fairly long durations, so that the space-charge effects are less severe due to a low instantaneous electron density. This is consistent with the fact that a higher bias voltage reduces the acceleration of the electrons at the cathode, as discussed above. Instead, at low bias

voltages, the energy spread of the beam drastically increases with electron density, suggesting that in realistic time-resolved operation a very low current has to be maintained to keep both a short pulse duration and a narrow energy distribution. The so-called "single electron regime" is attained by lowering the UV power on the cathode until the ZLP reaches its minimum width, 1 eV (corresponding to an UV illumination of less than 1 mW at 1 MHz repetition rate in Figure 1.2 B).

Temporal resolution

The duration of the electron pulses is characterized via photon-induced near field electron microscopy (PINEM) [15, 27, 28, 29, 30, 31, 32, 33]. When electrons and photons are overlapped spatially and temporally on a nanostructure, the evanescent field photo-induced at the edges of the latter interacts with the electrons allowing them to absorb and emit photons from the pump laser beam [15]. This results in sideband peaks spaced by an energy corresponding to the pump photon energy on both the energy gain and loss sides of the ZLP [15]. Because the surface charge density waves that mediate this interaction typically have very short lifetimes relative to the excitation pulse durations, the temporal duration of the PINEM effect is a cross-correlation between the laser pulse and the electron pulse, while they are both in the vicinity of the nanostructure. To measure the pulse duration using the PINEM effect a specimen of silver nanowires, whose average diameter was around 100 nm with average lengths of a few μm was used (see Figure 1.3 D).

The laser pulse duration was varied from 100 fs to 2 ps, at a wavelength of 800 nm (1.55 eV photons), with a repetition rate of 1 MHz and a fluence as high as 10 mJ/cm². The delay between the IR pump pulses and the photo-emitting UV pulses is changed via a computer-controlled optical delay-line. In Figure 1.3 A the time-energy dependence of the EEL spectrum through

the silver nanowire sample is displayed. The bias voltage in the Wehnelt lens was set to 300 V. In Figure 1.3 B the energy spectrum before the arrival of the laser pulses (red line) and at the time of coincidence between electrons and photons (blue line) is shown. The sideband peaks of the PINEM effect are clearly distinguishable and are separated by 1.55 eV as expected. We can count up to 18 peaks on each side of the zero-loss peak, corresponding to a gain or a loss in the kinetic energy of the electrons by as much as 27.9 eV. In Figure 1.3 C, the temporal evolution of one of the satellite peaks is displayed. The FWHM of the whole cross-correlation is around 1.5 ps, similar to what was reported in [15].

In Figure 1.3 D, an image of the silver nanowires taken integrating for 2 seconds the photoelectron beam is shown. These spectra show that our instrument has around 1 eV energy-resolution in pulsed operation, similar to the resolution of the conventional CW TEM and sufficient to look at both low-energy loss plasmons [13] and multiplets effects in core levels [34].

The electron pulse duration can be varied by changing either the initial laser pulse duration or bias voltage on the Wehnelt. In particular, the electron pulse duration is very sensitive to the bias voltage, for the reasons discussed above. In Figure 1.4, the evolution of the PINEM cross-correlation is shown as a function of the laser pulse duration and the bias voltage. In Figure 1.4 A, the temporal evolution of the ZLP of the PINEM spectrum for a bias voltage of 300 V is shown at different values of the laser pulse duration. Clearly, when the laser pulses are longer than the electron pulses, a longer cross-correlation is observed (magenta trace, 2.5 ps). Instead, a sharper effect is observed when the laser and electron pulses durations are equally matched. This happens at a value around 750 fs, delivering a good estimate of the electron bunch duration. In Figure 1.4 B, the temporal evolution of the PINEM signal for a bias voltage of 0 V at different durations of the laser pulses is displayed. In this case, an electron/light cross-correlation as short as 480 fs is observed, confirming the idea that the best time-resolution, i.e. shorter electron pulses, is obtained for the maximum acceleration from the cathode (no bias voltage

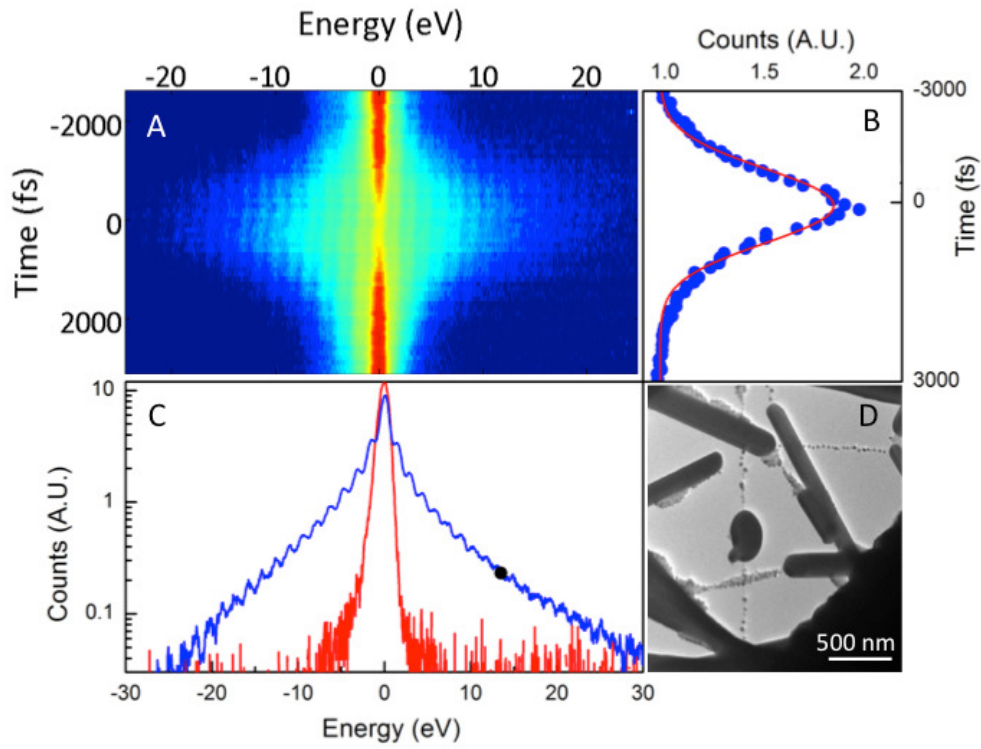


Figure 1.3: A Time/energy landscape of the PINEM effect on silver nanotubes. B temporal profile of one of the PINEM sidebands. C Energy profile of the PINEM spectrum. D Image of the silver nanowires. Image adapted from [26].

on the Wehnelt lens).

The dependence of the cross correlation FWHM on the laser pulses width is shown in Figure 1.4 C for the two bias voltages used, and in Figure 1.4 D the duration of the electron pulses is plotted against the bias voltage. An extra experiment was performed at a high bias (600 V), delivering pulses as long as 5 ps. To the best of our knowledge, the dependence of the PINEM effect on the initiating laser duration has never been reported, and it also provides an interesting insight in the relation between the photo-induced field duration and its interaction with the electrons. It is not immediately obvious for instance why a longer laser pulse produces a shorter cross-correlation. One possible explanation may be that the PINEM effect is highly nonlinear, and is enhanced when a strong electric field is present during the whole duration of the electron pulse, i.e. giving the sharpest effect when light and electron pulses durations coincide.

The overall duration of the PINEM effect strongly depends on the voltage placed on the Wehnelt. Moreover, when changing the Wehnelt voltage, a shift of the temporal coincidence between electrons and photons is also observed, as a consequence of the different acceleration times for the photo-emitted electrons. The temporal broadening is overcome by reducing the Wehnelt bias voltage to zero, which results in greatly reduced signal. However, this signal can be recovered by using the C0 lens to better couple the electrons down the column.

Conclusions

In conclusion, we demonstrate the ability to modify a commercial Wehnelt-based JEOL 2100 TEM for fs-pulsed operation. Having flexible control of the Wehnelt lens bias voltage and the addition of an electromagnetic lens right after the acceleration stage, we demonstrate the ability to obtain fs time-resolution, 1 eV energy resolution while maintaining a good overall brightness

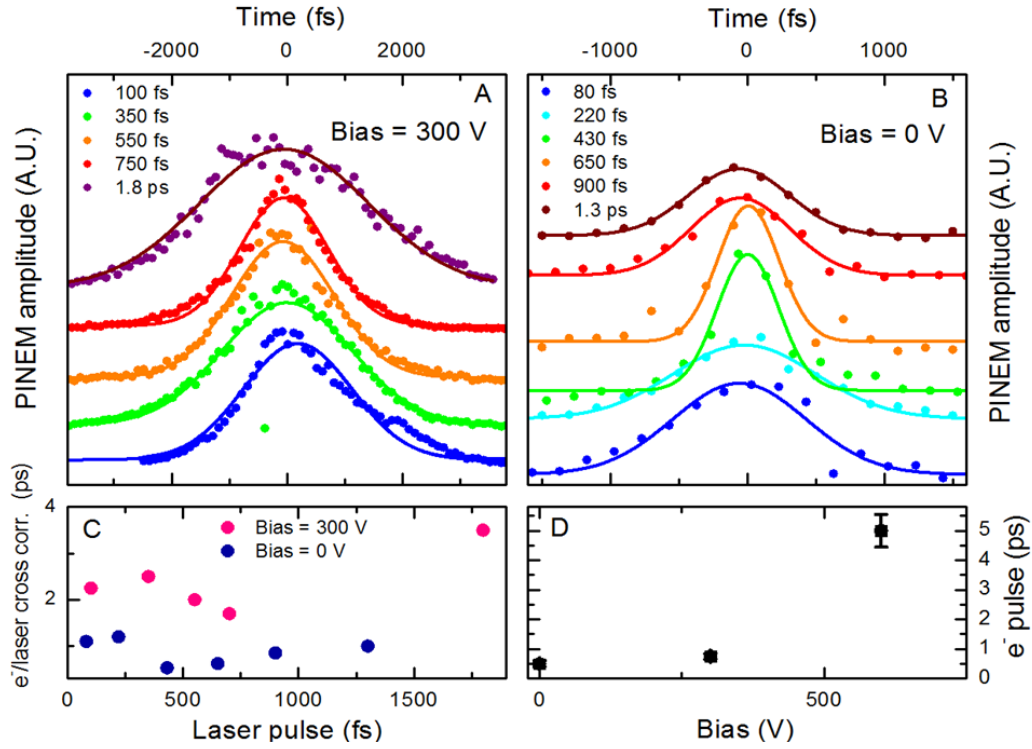


Figure 1.4: A Temporal profile of the amplitude of a PINEM sideband as a function of the laser pulses duration at a bias voltage of 300 V. The peak intensity of the pump is kept constant. B Temporal profile of a PINEM sideband as a function of the laser pulses duration at a bias voltage of 0 V. C FWHM of the PINEM temporal profile as a function of the laser pulse duration for two bias voltages. D The shortest electron pulse duration obtained at the different bias voltages is plotted against the bias. Image adapted from [26].

of the instrument. Also, the electron pulses properties in terms of duration and energy spread can be independently controlled via the bias voltage and the control of the photo-emission yield, making this tool highly versatile.

References

- [1] G V Spivak, O P Pavlyuchenko, and V I Petrov. “Electron microscopic observation of alterations of the domain structure of magnetic films”. In: *Bulletin of the Academy of Sciences of the USSR Physical Series* 30 (1966), pp. 822–826.
- [2] O Bostanjoglo and T Rosin. “Stroboscopic study on ultrasonic activity in electron-microscope”. In: *Mikroskopie*. Vol. 32. & CO SPENGER-GASSE 39, A-1051, 1976, pp. 190–190.
- [3] Bradley J Siwick et al. “Ultrafast electron optics: Propagation dynamics of femtosecond electron packets”. In: *Journal of applied physics* 92.3 (2002), pp. 1643–1648.
- [4] M Aidelsburger et al. “Single-electron pulses for ultrafast diffraction”. In: *Proceedings of the National Academy of Sciences of the United States of America* 107.46 (2010), pp. 19714–19719.
- [5] Yihua Wang and N Gedik. “Electron Pulse Compression With a Practical Reflectron Design for Ultrafast Electron Diffraction”. In: *IEEE Journal of Selected Topics in Quantum Electronics* 18.1 (2012), pp. 140–147.
- [6] Ahmed H Zewail. “Four-dimensional electron microscopy”. In: *Science* 328.5975 (2010), pp. 187–193.
- [7] F Carbone et al. “A perspective on novel sources of ultrashort electron and X-ray pulses”. In: *Chemical physics* 392.1 (2012), pp. 1–9.
- [8] F Carbone. “Modern electron microscopy resolved in space, energy and time”. In: *European Physical Journal Applied Physics* 54.3 (2011), p. 33503.

- [9] Giulia Fulvia Mancini et al. “Design and implementation of a flexible beamline for fs electron diffraction experiments”. In: *Nuclear instruments & methods in physics research. Section A, Accelerators, spectrometers, detectors and associated equipment* 691.0 (2012), pp. 113–122.
- [10] J B Hastings et al. “Ultrafast time-resolved electron diffraction with megavolt electron beams”. In: *Applied physics letters* 89.18 (2006), pp. 184109–189900.
- [11] Shigeki Tokita et al. “Single-shot ultrafast electron diffraction with a laser-accelerated sub-MeV electron pulse”. In: *Applied physics letters* 95.11 (2009), p. 111911.
- [12] Fabrizio Carbone, Oh-Hoon Kwon, and Ahmed H Zewail. “Dynamics of chemical bonding mapped by energy-resolved 4D electron microscopy”. In: *Science* 325.5937 (2009), pp. 181–184.
- [13] Fabrizio Carbone et al. “EELS femtosecond resolved in 4D ultrafast electron microscopy”. In: *Chemical physics letters* 468.4–6 (2009), pp. 107–111.
- [14] David J Flannigan, Brett Barwick, and Ahmed H Zewail. “Biological imaging with 4D ultrafast electron microscopy”. In: *Proceedings of the National Academy of Sciences of the United States of America* 107.22 (2010), pp. 9933–9937.
- [15] Brett Barwick, David J Flannigan, and Ahmed H Zewail. “Photon-induced near-field electron microscopy”. In: *Nature* 462.7275 (2009), pp. 902–906.
- [16] Brett Barwick et al. “4D imaging of transient structures and morphologies in ultrafast electron microscopy”. In: *Science* 322.5905 (2008), pp. 1227–1231.
- [17] Judy S Kim et al. “Imaging of transient structures using nanosecond in situ TEM”. In: *Science* 321.5895 (2008), pp. 1472–1475.

- [18] P Musumeci et al. “Laser-induced melting of a single crystal gold sample by time-resolved ultrafast relativistic electron diffraction”. In: *Applied physics letters* 97.6 (2010), p. 063502.
- [19] Vladimir A Lobastov, Ramesh Srinivasan, and Ahmed H Zewail. “Four-dimensional ultrafast electron microscopy”. In: *Proceedings of the National Academy of Sciences of the United States of America* 102.20 (2005), pp. 7069–7073.
- [20] Hyun Soon Park et al. “Atomic-scale imaging in real and energy space developed in ultrafast electron microscopy”. In: *Nano letters* 7.9 (2007), pp. 2545–2551.
- [21] T LaGrange et al. “Single-shot dynamic transmission electron microscopy”. In: *Applied physics letters* 89.4 (2006), p. 044105.
- [22] Thomas LaGrange et al. “Nanosecond time-resolved investigations using the in situ of dynamic transmission electron microscope (DTEM)”. In: *Ultramicroscopy* 108.11 (2008), pp. 1441–1449.
- [23] B W Reed et al. “Solving the accelerator-condenser coupling problem in a nanosecond dynamic transmission electron microscope”. In: *The Review of scientific instruments* 81.5 (2010), p. 053706.
- [24] Hyuk Park and J M Zuo. “Implications for Ultrafast Reflection Electron Diffraction from Temporal and Spatial Evolution of Transient Electric Fields”. In: *MRS Proceedings* 1230 (2009), pp. 1230–MM03–07.
- [25] Sascha Schäfer, Wenxi Liang, and Ahmed H Zewail. “Structural dynamics and transient electric-field effects in ultrafast electron diffraction from surfaces”. In: *Chemical physics letters* 493.1–3 (2010), pp. 11–18.
- [26] L Piazza et al. “Design and implementation of a fs-resolved transmission electron microscope based on thermionic gun technology”. In: *Chemical physics* 423.0 (2013), pp. 79–84.
- [27] Sang Tae Park, Milo Lin, and Ahmed H Zewail. “Photon-induced near-field electron microscopy (PINEM): theoretical and experimental”. In: *New journal of physics* 12.12 (2010), p. 123028.

- [28] Sang Tae Park and Ahmed H Zewail. “Relativistic effects in photon-induced near field electron microscopy”. In: *The journal of physical chemistry. A* 116.46 (2012), pp. 11128–11133.
- [29] Ayca Yurtsever, Renske M van der Veen, and Ahmed H Zewail. “Sub-particle ultrafast spectrum imaging in 4D electron microscopy”. In: *Science* 335.6064 (2012), pp. 59–64.
- [30] Ayca Yurtsever, J Spencer Baskin, and Ahmed H Zewail. “Entangled nanoparticles: discovery by visualization in 4D electron microscopy”. In: *Nano letters* 12.9 (2012), pp. 5027–5032.
- [31] Ayca Yurtsever and Ahmed H Zewail. “Direct visualization of near-fields in nanoplasmonics and nanophotonics”. In: *Nano letters* 12.6 (2012), pp. 3334–3338.
- [32] Sang Tae Park, Oh-Hoon Kwon, and Ahmed H Zewail. “Chirped imaging pulses in four-dimensional electron microscopy: femtosecond pulsed hole burning”. In: *New journal of physics* 14.5 (2012), p. 053046.
- [33] Sang Tae Park and Ahmed H Zewail. “Enhancing image contrast and slicing electron pulses in 4D near field electron microscopy”. In: *Chemical physics letters* 521 (2012), pp. 1–6.
- [34] Fabrizio Carbone et al. “Electronic structure of MnSi: The role of electron-electron interactions”. In: *Physical Review B: Condensed Matter and Materials Physics* 73.8 (2006), p. 085114.

Chapter 2

Ultrafast diffraction and electron energy loss spectroscopy of layered manganites

In the last decade both theoretical and experimental results revealed that the properties of several classes of materials are dominated by spatially not homogeneous states. This situation appears when several physical interactions — charge, spin, lattice and/or orbital — survive in a common volume of the parameter space. The behavior of such materials in these circumstances causes interesting effects, such as *colossal magneto-resistance*, and it also appear relevant to understand high-temperature superconductivity.

The complexity of the electronic configurations can lead to unusual macroscopic properties, potentially characterized by giant responses to small perturbations. From a technological point of view, not only charge and spin can

Parts of this chapter are taken from *Ultrafast structural and electronic dynamics of the metallic phase in a layered manganite*, L. Piazza *et al*, Structural Dynamics, 1 014501, 2014, an extended introduction and more considerations are added.

Chapter 2. Ultrafast diffraction and EELS

be exploited (semiconductor electronics and spintronics) but also the degrees of freedom relative to lattice and orbital configurations.

Compounds of Manganese of the form $AMnO_3$ (where A can be one between La, Ca, Ba, Sr, Pb, Nd and Pr) are characterized by the perovskite crystal structure ($CaTiO_3$) and are known since more than sixty years (cite van Santen and Jonker, 1950). The colossal magnetoresistance effect they exhibit has not been observed in other bulk metallic systems. Comparable dependence to external magnetic fields arises only in the case of pure crystals at very low temperatures where the mean free path of the conducting electrons is greatly reduced by the magnetic field inducing circular trajectories.

Depending on the actual composition manganites exhibit several different phenomena, including charge and orbital ordering, ferromagnetism and anti-ferromagnetism. If the state A is partially occupied by atoms with different valence, Mn^{3+} and Mn^{4+} can coexist along different lattice directions giving rise to domains in the microscopic scale that can be observed in a transmission electron microscope.

Some manganite compounds crystallize in structures that present a layered arrangement. In such compounds the conductive MnO_2 planes are separated from each other by AO layers.

Layered manganites, as some other 2D materials, provide a unique playground for observing charge ordering phenomena due to the lowered dimensionality of their electronic structure [1, 2, 3]. These states of matter are of current interest both for their fundamental properties and their potential exploitation in microelectronics. In particular, manganites have a rich phase diagram originating from the presence of several competing energy scales; this results in a broad versatility which has already seeded multiple applications [4].

The phase diagram of these compounds can be explored manipulating one of several macroscopic parameters. Transitions between different magnetic,

charge and orbital ordered states, can be driven by temperature [5], pressure [6], magnetic field [7], and chemical doping [5]. Recent experiments have shown that light pulses can also make these systems cross the different critical lines of their phase diagram [8]. In particular, the dynamics of charge and orbital ordering have been investigated by directly triggering specific lattice distortions via resonant THz radiation pulses, [9] and orbital waves have also been detected via high temporal resolution optical experiments [10]. Moreover, the temporal evolution of the net magnetization upon photo-excitation has been observed by ultrafast optical Kerr rotation experiments [11, 12], yielding quantitative information about the spin-orbit interaction in $\text{La}_{0.6}\text{Sr}_{0.4}\text{MnO}_3$.

So far, most of the time-resolved studies in these materials have been carried out via optical [13, 14], and X-ray probes [15, 16, 17, 18, 19]; the latter have allowed the observation of the structural rearrangement in the solid upon melting the charge and orbital ordering [17, 18], as well as the formation of metastable states with exotic properties accessible only in the picosecond (ps) time scale [20]. Combined dynamical information about the crystal and electronic structure have been obtained via resonant X-ray diffraction at the L absorption edge of Mn ions, very sensitive to the material's spin state, showing that in the metastable photo-induced phase, magnetism could be suppressed while maintaining the orbital ordering in the system [16].

Charge and orbital organized patterns in solids give rise to spatial modulations of the crystalline order visible as superlattices in diffraction, often accompanied by distinct fingerprints in the electronic structure. As demonstrated in [16], the ability to monitor the evolution of both the crystal and electronic structure in a broad momentum and energy range provides a privileged point of view on these phenomena and their evolution through the critical lines of the phase diagram.

Charge and orbital ordering in layered materials have been observed also by electron diffraction and microscopy, both statically [21] and with fs resolution [22]. Ultrafast electron microscopy offers the advantage of delivering

Chapter 2. Ultrafast diffraction and EELS

momentum-resolved information through diffraction and broad-band electron energy loss spectroscopy in a very direct fashion and from very tiny amounts of material [23, 24, 25]. In the bi-layered $\text{PrSr}_{0.2}\text{Ca}_{1.8}\text{Mn}_2\text{O}_7$, a peculiar checkerboard pattern made of ordered orbital stripes has been observed via transmission electron microscopy (TEM) [21], and optical spectroscopy [26], and originates from a 1:1 ratio of Mn^{3+} and Mn^{4+} ions in the ground state. The evolution of the orbital and charge ordering in this material can be tuned with chemical doping or temperature, giving rise to a very rich phase diagram [27].

For the reasons exposed a sample from this class has been chosen to perform combined static and time-resolved electron diffraction and time-resolved electron energy loss spectroscopy. We show that laser light can be used in-situ in a TEM to drive a $\text{PrSr}_{0.2}\text{Ca}_{1.8}\text{Mn}_2\text{O}_7$ sample in different regions of its phase diagram, and then perform an ultrafast investigation of its metallic phase. Pressure waves can be launched in thin samples via light-induced temperature jumps, resulting in a modulation of the crystal structure that can be followed by ultrafast diffraction and imaging experiments [28, 29], while the consequent modulation of the electronic structure can be monitored with ultrafast spectroscopy [23, 24]. Coherent structural motions of a $\text{PrSr}_{0.2}\text{Ca}_{1.8}\text{Mn}_2\text{O}_7$ single crystal induced by the photo-induced temperature jump were detected as periodic modulations of the Bragg peak intensities. In the same instrument, the resulting modulation of the loss function was recorded over a broad energy range (2 eV to 70 eV), evidencing the response of the different electronic states to specific atomic motions. Such an interplay was understood via density functional theory (DFT) calculations of the EELS spectra, performed considering an equilibrated electronic structure at different lattice parameters.

This study provides the necessary background information to further investigate the more complex regions of the phase diagram, and confirms the ability of the ultrafast temperature-modulation approach to provide a direct view of light induced thermal phenomena in a solid.

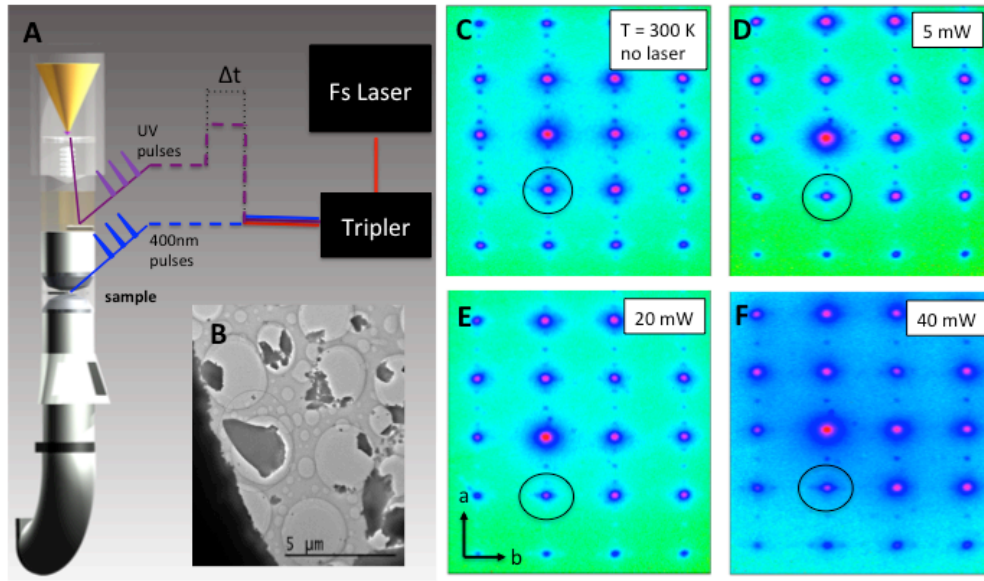


Figure 2.1: A Experimental set-up. The TEM column is depicted, the parts where the optical paths are found are transparent. B Image of the $\text{PrSr}_{0.2}\text{Ca}_{1.8}\text{Mn}_2\text{O}_7$ single crystalline nanoparticles. C Static unperturbed diffraction pattern at $T=300$ K. In the black circle the charge/orbital ordering satellites are evidenced. D, E, F static diffraction pattern for the sample irradiated by 5, 20 and 40 mW of laser light at 1 MHz respectively. Image adapted from [30].

The sample and the experimental setup

A polycrystalline sample of $\text{PrSr}_{0.2}\text{Ca}_{1.8}\text{Mn}_2\text{O}_7$ was prepared by the solid-state reaction technique. The compound was prepared via a mixture of Pr_6O_{11} , CaCO_3 , SrCO_3 and MnO_2 , in the desired proportions, heated to around 900°C in air for 12 hours, then ground and sintered at 1450°C for 24 hours. The TEM samples used in the present study were prepared by crushing the well-characterized polycrystalline, and then the resultant ethanol suspensions were dispersed on a holey carbon-covered Cu grid. The crystallinity, shape and orientation of the different micrometer-sized flakes were checked by imaging and diffraction in our TEM (see Figure 2.1 A, B, C) and by observing the shape and orientation of the Kikuchi lines (see Figure 2.2).

Two samples were selected on the basis of the optimal shape and thickness for diffraction and EELS experiments. The sample for diffraction was 100 nm thick, while the one used for EELS was twice as thin (50 nm), to prevent severe multiple scattering effects [31]. The samples were then mounted on a double tilt holder and inserted in our fs-TEM [32] (the set-up is depicted in Figure 2.1 A).

The experimental setup and its performances in term of temporal, spatial and energy resolution are described in Chapter 1. Briefly, fs electron and photo-exciting pulses are generated by a Wyvern X Ti:Sapp amplified laser capable of 5 W average power at rep-rates between 200 kHz and 2 MHz. The pulse duration was set at 80 fs and the photon energy was frequency doubled to obtain 400 nm linearly polarized pump pulses containing up to $1\ \mu\text{J}$ of energy at 1 MHz repetition-rate.

in-situ static measurement

To perform a static *in-situ* observation the pump beam was focused on the sample in a $100\ \mu\text{m}$ spot, and the fluence was chosen to provide an average

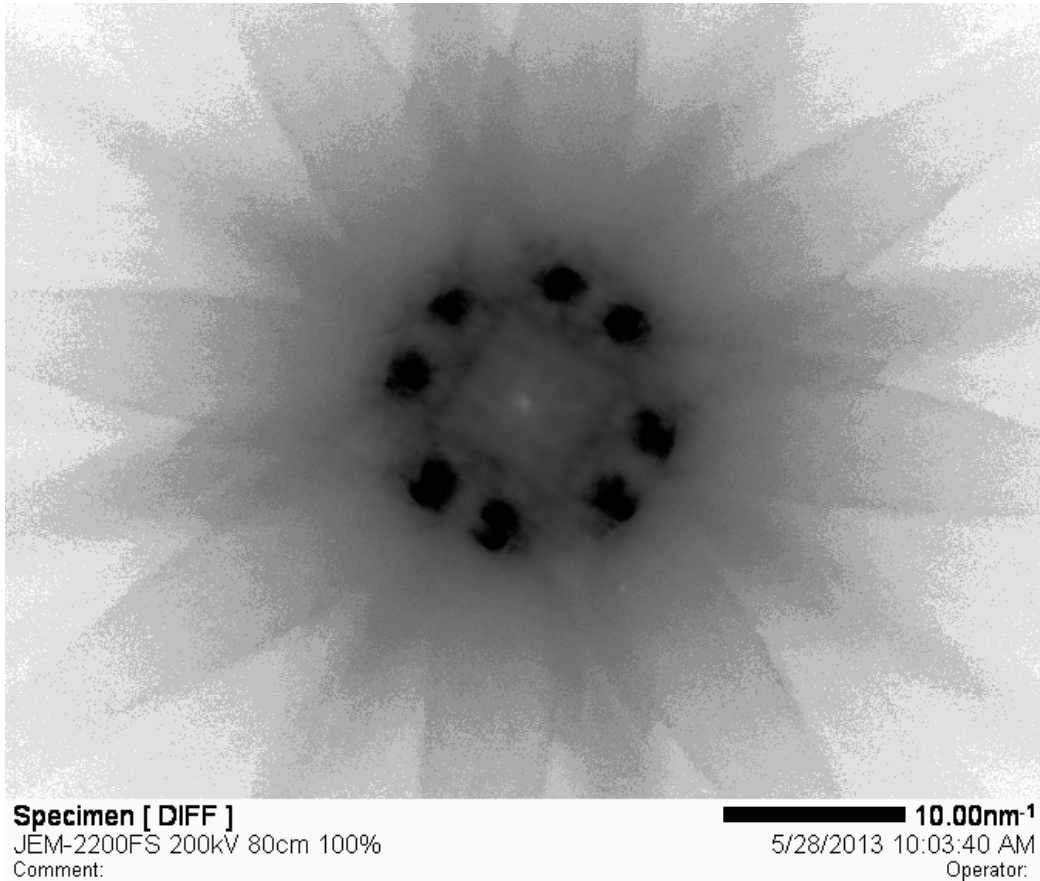


Figure 2.2: An example of Kikuchi lines observed in a $\text{PrSr}_{0.2}\text{Ca}_{1.8}\text{Mn}_2\text{O}_7$. The orientation of the sample can be inferred and optimized from the image. In this case the electron beam is aligned with the $[0\ 0\ 1]$ zone axis of the crystal flake. Image acquired at the Interdisciplinary Center for Electron Microscopy (CIME) at EPFL, using a Jeol JEM-2200fs electron microscope equipped with a 200kV field emission source.

heating of the specimen sufficient to drive the material into its metallic phase, by suppressing the charge/orbital ordering that is naturally present at room temperature [21]. In Figure 2.1, C, D, E, F and in the inset of Figure 2.3 A, the diffraction patterns for the unperturbed sample, the sample excited by 5 mW at 1 MHz (corresponding to a fluence of $16 \mu\text{J}/\text{cm}^2$), the sample excited by 20 mW, 40 mW, and 100 mW respectively are displayed.

The charge/orbital ordering satellites, indicated in the figure, are found to first rotate at intermediate laser fluence, corresponding to an average heating that brings the sample temperature from 300 K to about 320 K, while they have completely disappeared for an average pump power of 100 mW ($320 \mu\text{J}/\text{cm}^2$; the latter is the fluence used in our time-resolved experiments at which the sample is deeply in its metallic phase, at a temperature above 350 K). Upon irradiating the sample with the laser at 1 MHz repetition-rate, an increase in the sample temperature was observed and stabilized within few minutes, indicating that a new equilibrium was reached at a temperature higher than room temperature itself. In this condition, it was verified that the system relaxes to such a new thermal equilibrium between subsequent pulses, as testified by the flat temporal dependence of the diffraction intensity before time-zero, in Figure 2.3.

Ultrafast electron diffraction

Snapshots of the crystal structure at different time-delays between the pump and the probe are obtained via fs electron diffraction. The sample is oriented in such a way that the electron beam impinges along the direction perpendicular to the ab -plane of the material. The diffraction patterns, in Figure 2.1 C,D,E,F and Figure 2.3 inset, show the lattice parameters $a, b = 5.46 \text{ \AA}$, and the satellites at $q_a, q_b \simeq 0.45$. In the metallic phase (Figure 2.3 inset), the satellites are absent.

Light excitation is performed via 400 nm laser pulses, in the interband tran-

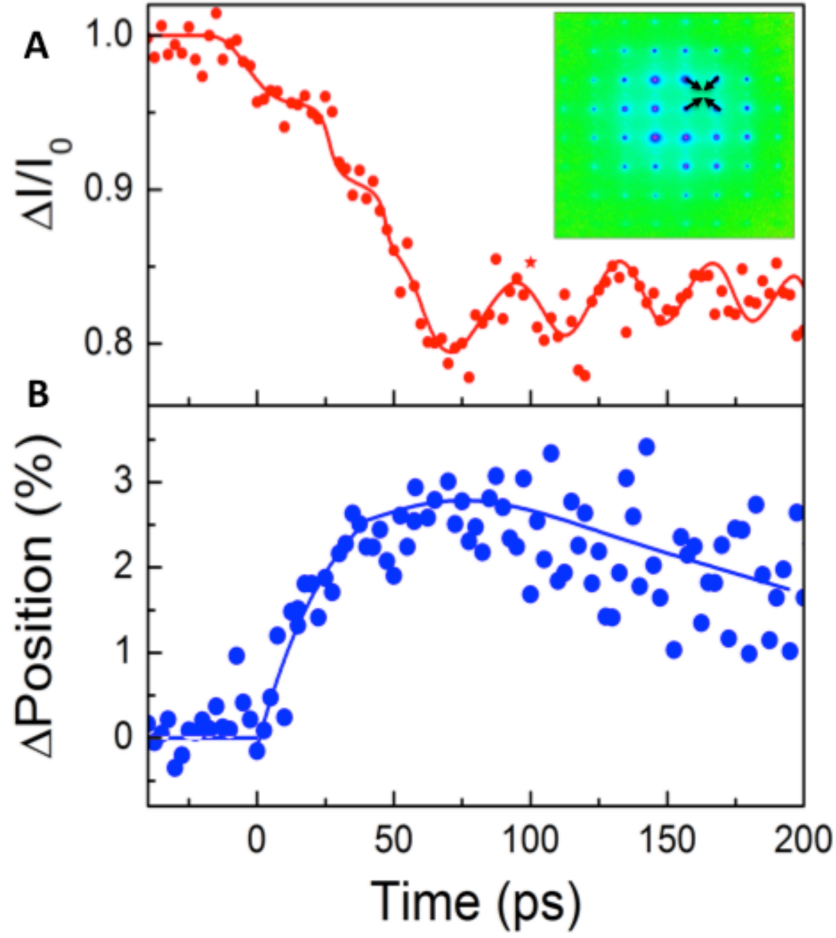


Figure 2.3: A Temporal evolution of the Bragg diffraction intensity. In the inset, the diffraction pattern for the sample irradiated by 100 mW of laser light at 1 MHz is shown. No charge/orbital ordering is evident in these conditions. B temporal evolution of the in-plane diagonal. Image adapted from [30].

sitions region of the optical conductivity [26]. At positive time delays, the Bragg peak intensities are found to decrease, according to the behavior dictated by the Debye-Waller effect. The transient data along the in-plane diagonal of the unit cell are depicted in Figure 2.3. An exponential intensity drop of as much as 18% with a time constant of 31 ps is observed; this, according to the Debye formula: $\ln(I/I_0) = -s^2 \langle u^2 \rangle / 3$ would correspond to an average atomic displacement induced by the temperature jump of around 3% of the interatomic distance. In Figure 2.3 B, the change of the in-plane diagonal is shown; an expansion of 3% of the equilibrium value is indeed observed within the same time-scale (obtained via an exponential fit to be 31 ps). The distortion of the c -axis lattice parameter also contributes to the DW effect and is expected to be of the same size.

In the dynamics of the Bragg peak intensity, an oscillation originating from the pressure-wave launched by the photo-excitation is visible. In this scenario, the sample behaves like the membrane of a drum, vibrating at particular frequencies that coincide with the film's eigenmodes [29]; in our measurements, these oscillations have a period of 48 ps. It is possible to estimate the Young modulus (Y) along the c -axis knowing the thickness and the density of the material through the formula that relates Y to the oscillation period of an ideal freely vibrating nanofilm: $\frac{1}{\tau_p} = \frac{n}{2d} \left(\frac{Y}{\rho} \right)^{1/2}$, with $n = 1$ for the fundamental tone. For the single crystal used for diffraction, assuming a density that for manganites typically is around 6.5g/cm³ [33], we obtain a value of 113 GPa.

Ultrafast EELS

In electron energy loss spectroscopy, multiple scattering effects complicate the assignment of the different spectroscopic features by inducing broad satellite peaks [31]. To avoid this problem, thinner samples must be used. For this reason, the mesoscopic sample we selected to perform ultrafast EELS was

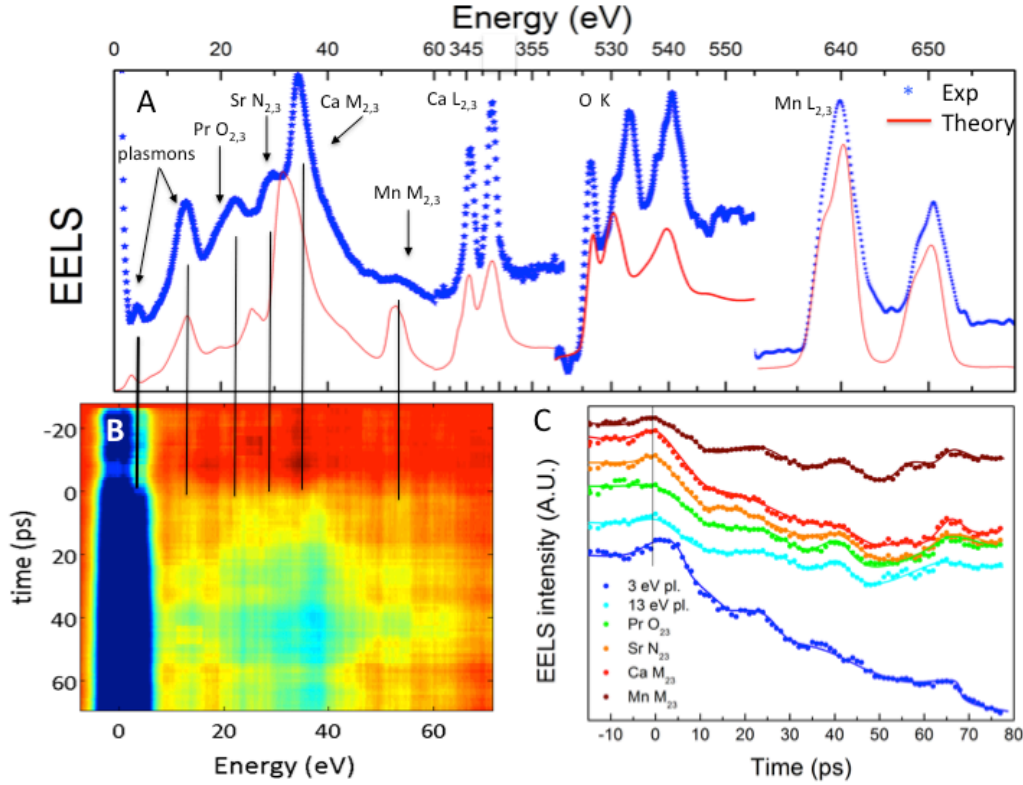


Figure 2.4: A Static EELS spectrum from 0 to 700 eV (blue symbols). The red curves are theoretical calculations; DFT calculations are used until 600 eV and atomic multiplet calculations for the Mn L-edge above 600 eV. B Energy-time map of the low loss EELS spectrum. The 3D plot is obtained by taking the difference between $EELS(t) - EELS(t < 0)$. C Temporal profile of the EELS intensity at selected energies, in correspondence with the specified electronic states. Image adapted from [30].

twice as thin (50 nm) the one observed in diffraction.

The static spectra of our $\text{PrSr}_{0.2}\text{Ca}_{1.8}\text{Mn}_2\text{O}_7$ sample are displayed in Figure 2.4 A in the range from 0 eV to 700 eV. Each region of this broad spectrum is modeled by theoretical calculations; in particular, in the low loss region, between 0 and 70 eV, two plasmon peaks at 3 eV and 13 eV are observed and are assigned to the partial and the highly-damped valence electron plasmon respectively. At higher energy, the shallower core levels are found, such as the Pr $\text{O}_{2,3}$ at 20 eV, the Sr $\text{N}_{2,3}$ at 29 eV, the Ca $\text{M}_{2,3}$ 34 eV and the Mn $\text{M}_{2,3}$ at 55 eV. This portion of the spectrum is modeled via state of the art DFT calculations via Wien2k code [34], see red line in Figure 2.4 A.

Chapter 2. Ultrafast diffraction and EELS

The calculations are in reasonable agreement with the experiment, despite a shift of some of the electronic states already observed in previous reports [35]. At 345 eV, the Ca $L_{2,3}$ is observed and the 3 eV spin-orbit splitting is evident on this edge. In the oxygen K-edge instead, the sharp peak at 524.4 eV originates from the hybridized states between O-2*p* and Mn-3*d* orbitals, while two pronounced peaks centered at about 532 eV and 540 eV come from the hybridization of the O-2*p* with Pr/Sr/Ca and Mn-4*s*/4*p* states. The splitting between the valence band and upper Hubbard band is invisible here, because it is smaller than the energy resolution ($\simeq 1$ eV in our fs-TEM). In the DFT calculations, red trace in Figure 2.4 A, only the strong feature originating from the Pr-O hybridization at 533 eV is not captured. To simulate the Mn L-edge, the atomic multiplets code is used [36]. The EELS spectrum is simulated by a mixed valence state $\text{Mn}^{3+} + \text{Mn}^{4+}$, in a crystal field environment of 2.4 eV as estimated by the Mn bands splitting in the high symmetry points of the fat bands diagram [37]. The broad experimental energy range provides a solid constraint to our modeling of the EELS spectra, which we use to understand the following time-resolved experiments.

Upon light excitation, as shown in diffraction, the film undergoes a periodic structural modulation as well as an overall dilatation due to the light induced temperature jump. The period of the modulation depends on the sample thickness, its Young modulus and density. For EELS experiments, the 50 nm thick sample used gives rise to a faster oscillation of the dynamical spectra with a period of 23 ps. The overall energy-time map of the experimental data is depicted in Figure 2.4 B, where black lines indicate the energies corresponding to the different electronic states observed in the static spectra. Each of these states shows a different temporal dynamics, reflecting a different sensitivity to the photo-induced structural distortions. This is better visible in Figure 2.4 C, where the temporal profile corresponding to each energy level is shown. Here, an overall decay of the peak intensity is observed after time zero, with a periodic modulation superimposed. It is interesting to notice that despite the overall effect is the weakest on the Mn M-edge at 53 eV, the periodicity is the clearest at this energy, suggesting that

the Mn orbitals are the most sensitive to the structural distortions. This is not surprising considering the large crystal field on the Mn ions, which we estimated from the band structure and the Mn L-edge static spectrum, and that is certainly affected by the shape and dimension of the cage surrounding the Mn ions.

Discussion of the results

To understand the dynamical EELS spectra, we performed DFT calculations of the low-loss as well as the oxygen K-edge region for different structural parameters, reflecting the changes estimated by diffraction, i.e. an overall lattice expansion by few percents of its equilibrium value. For comparison, we also calculate the spectrum for a compressed lattice, to verify the unambiguity of our interpretation.

In Figure 2.5 A, the difference spectra $\text{EELS}(\text{compr.}-ab) - \text{EELS}(\text{equil.})$, $\text{EELS}(\text{expand.}-ab) - \text{EELS}(\text{equil.})$, $\text{EELS}(\text{compr.}-c) - \text{EELS}(\text{equil.})$ and $\text{EELS}(\text{expand.}-c) - \text{EELS}(\text{equil.})$ are shown together with the experimental difference spectra $\text{EELS}(t < 0) - \text{EELS}(t = 0)$ and $\text{EELS}(t = 50\text{ps}) - \text{EELS}(t = 0)$. The sign of the transient change, i.e. a reduced EELS intensity, is captured by the calculations that consider an expanded lattice after time zero. The overall shape of the transient spectrum is also reasonably reproduced by the calculated difference spectra with a good coincidence between the position and relative strength of the negative peaks; the simulations consider a lattice expansion/compression in both ab and c direction of 2%, and estimate intensity changes of the EELS features in the order of 3%, and energy shifts in the order of 80-90 meV, close to what was observed in another layered solid, namely graphite [23].

The magnitude of these changes is in good agreement with the experimental observation; the largest energy shift is observed at the Ca edge, causing a positive peak in the low energy side of the edge, in the theoretical curve.

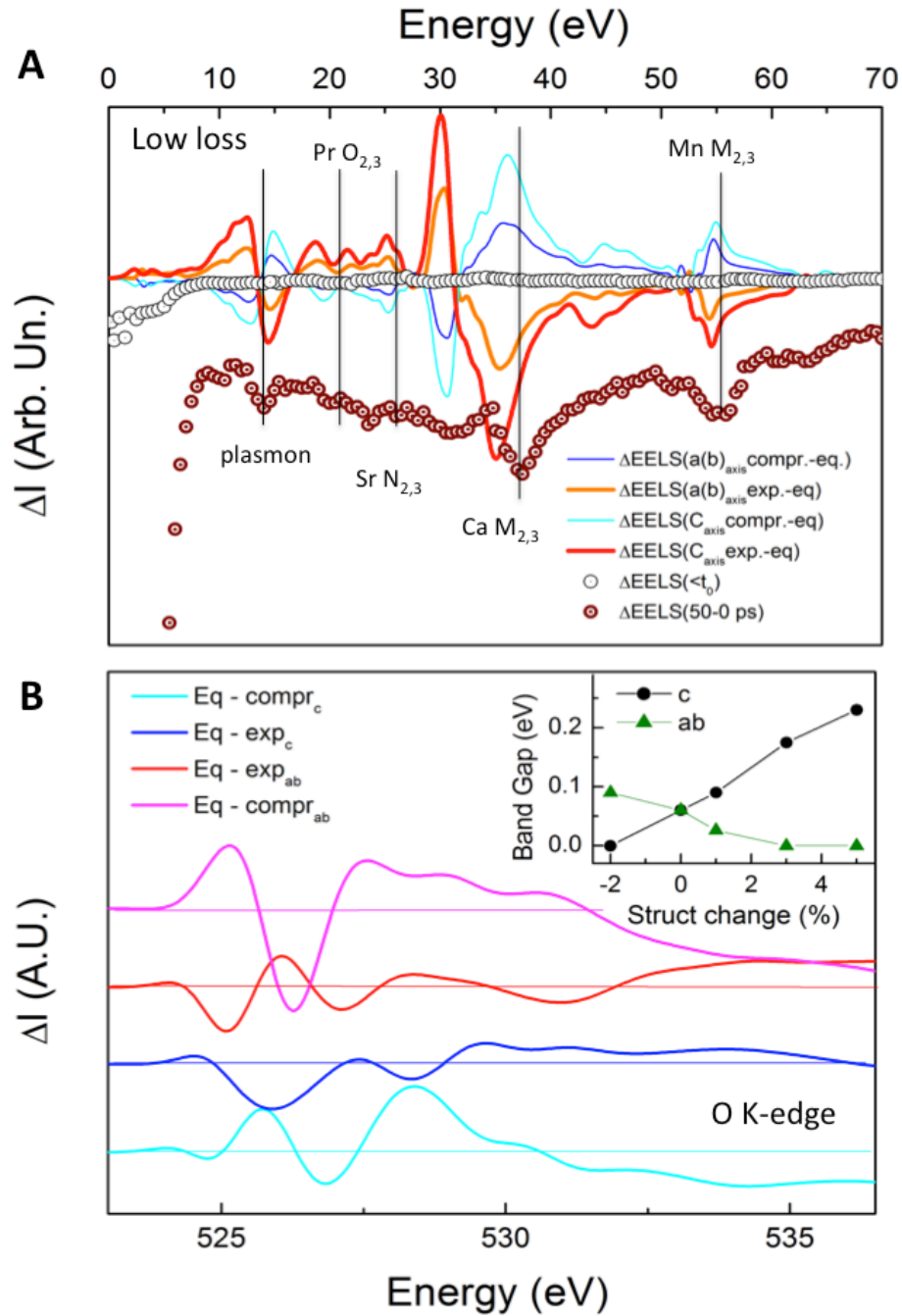


Figure 2.5: A The experimental differential EELS spectrum at $t=50$ ps is shown together with the calculated difference spectra for expanded/compressed ab -plane and c -axis. B Differential EELS spectra for the oxygen K-edge. The different lines are obtained by taking the difference between the K-edge spectrum at equilibrium and the spectrum for a compressed/expanded $a(b)$ or c -axis lattice parameters. In the inset, the evolution of the band gap as a function of the in-plane and out-of-plane lattice parameters change is shown. Image adapted from [30].

While the intensity change is captured by the experiment, the small energy shift (80 meV) is washed out by the overall energy resolution in time-resolved mode, around 2 eV. For this reason, the sharp positive peak is not visible in our transient data; the same situation was observed in previous time-resolved EELS data [38].

In Figure 2.5 B, the same simulation is performed for the oxygen K-edge spectrum. Interestingly, while in the low loss region of the spectrum (1-70 eV) an expansion of the in-plane or *c*-axis lattice parameters induces similar energy shifts and intensity changes of the different spectroscopic features, in the near-edge region of the oxygen K-edge, the behavior due to the in-plane or out of plane distortions is radically different. This is due to the fact that the O K-edge is very sensitive to the local Mn-O chemical bonding and consequently the orbital occupancy, while the low-loss spectra, including plasmons and other ionization edges, is mostly related to the bandwidth which depends on the volume expansion. In the charge/orbital ordered state, the orbital shape for Mn³⁺ sites is dominated by the low-lying in-plane ($3x^2-r^2$) / ($3y^2-r^2$)-type orbitals which can be rotated through pressure or temperature changes. Therefore, changes in the lattices parameters along different directions would result in different orbital reconstruction. In addition, our calculations also demonstrate that the expanded *a* and *b* lattice parameters lead to a decrease in the energy gap, while the expanded *c*-axis lattice parameter has the opposite effect, as shown in the inset of Fig 4 B.

These results show that photo-excitation can be used to span the phase diagram of a manganite. In this particular case, we used light as a source of both continuous heating (to drive the system into its metallic phase) and to induce an ultrafast temperature jump in the material. The response to such a temperature jump was monitored via a combination of diffraction and EELS to observe the interplay between structural and electronic effects in the metallic phase of the sample. The only other ultrafast EELS experiment ever performed on a solid reported a radically different behavior in the first few ps of the dynamics for the layered system graphite [23]. In that case,

a compression of the system was observed before thermal expansion would take place. This behavior was attributed to the anisotropic decay of the out-of-equilibrium electronic structure, due to the peculiar semi-metallic band structure of graphite [23]. The present results rule out this behavior as a general feature of layered compounds, while a strong similarity between the layered manganite and graphite is observed in the long-time scale (several ps). In both materials in fact, the light-induced thermal expansion is found to modulate the electronic structure in a similar way. In particular, the low-loss energy range of the EELS spectrum is shown to be able to discriminate between compression and expansion of the lattice, while being somewhat insensitive to the direction of the ionic motions, in-plane or out-of-plane. Based on these results, we also predict that distortions of the *ab*-plane or *c*-axis lattice parameters instead give very distinct spectroscopic signatures in the oxygen K-edge EEL spectrum.

Conclusions

These results provide a broad band direct observation of the interplay between the crystal and the electronic structure in a charge ordered manganite, and are the starting point for a deeper understanding of the different phase transitions in these materials. In fact, once the thermal effects are understood, it will be easier to distinguish dynamical electronic effects across charge ordering transitions. In particular, the fs dynamics of the orbital ordering rotation, as observed both via static conventional temperature dependent experiments, and the static photo-induced ones reported in Figure 2.1 is currently under investigation by the same technique.

References

- [1] K S Novoselov. “Nobel Lecture: Graphene: Materials in the Flatland”. In: *Reviews of modern physics* 83.3 (2011), pp. 837–849.
- [2] Myron Salamon and Marcelo Jaime. “The physics of manganites: Structure and transport”. In: *Reviews of modern physics* 73.3 (2001).
- [3] Andrea Damascelli, Zahid Hussain, and Zhi-Xun Shen. “Angle-resolved photoemission studies of the cuprate superconductors”. In: *Reviews of modern physics* 75.2 (2003), pp. 473–541.
- [4] A-M Haghiri-Gosnet and J-P Renard. “CMR manganites: physics, thin films and devices”. In: *Journal of physics D: Applied physics* 36.8 (2003), R127.
- [5] M Merz et al. “Orbital degree of freedom in single-layered $\text{La}_{1-x}\text{Sr}_x\text{MnO}_4$: Doping- and temperature-dependent rearrangement of orbital states”. In: *Physical review. B, Condensed matter* 74.18 (2006).
- [6] Y Moritomo et al. “Pressure effects on charge-ordering transitions in Perovskite manganites”. In: *Physical review. B, Condensed matter* 55.12 (1997), pp. 7549–7556.
- [7] C Martin et al. “Magnetic phase diagrams of $\text{L}_{1-x}\text{A}_x\text{MnO}_3$ manganites ($\text{L}=\text{Pr}, \text{Sm}$; $\text{A}=\text{Ca}, \text{Sr}$)”. In: *Physical review. B, Condensed matter* 60.17 (1999), pp. 12191–12199.
- [8] M Rini et al. “Time-resolved studies of phase transition dynamics in strongly correlated manganites”. In: *Journal of physics. Conference series* 148.1 (2009), p. 012013.
- [9] D Polli et al. “Coherent orbital waves in the photo-induced insulator–metal dynamics of a magnetoresistive manganite”. In: *Nature materials* 6.9 (2007), pp. 643–647.
- [10] Matteo Rini et al. “Control of the electronic phase of a manganite by mode-selective vibrational excitation”. In: *Nature* 449.7158 (2007), pp. 72–74.

- [11] K Miyasaka et al. “Ultrafast photoinduced magnetic moment in a charge-orbital-ordered antiferromagnetic $\text{Nd}_{0.5}\text{Sr}_{0.5}\text{MnO}_3$ thin film”. In: *Physical review. B, Condensed matter* 74.1 (2006), p. 012401.
- [12] T Ogasawara et al. “Photoinduced spin dynamics in $\text{La}_{0.6}\text{Sr}_{0.4}\text{MnO}_3$ observed by time-resolved magneto-optical Kerr spectroscopy”. In: *Physical review. B, Condensed matter* 68.18 (2003), p. 180407.
- [13] R D Averitt et al. “Ultrafast conductivity dynamics in colossal magnetoresistance manganites”. In: *Physical review letters* 87.1 (2001), p. 017401.
- [14] M Matsubara et al. “Ultrafast photoinduced insulator-ferromagnet transition in the perovskite manganite $\text{Gd}_{0.55}\text{Sr}_{0.45}\text{MnO}_3$ ”. In: *Physical review letters* 99.20 (2007), p. 207401.
- [15] M Först et al. “Driving magnetic order in a manganite by ultrafast lattice excitation”. In: *Physical review. B, Condensed matter* 84.24 (2011), p. 241104.
- [16] H Ehrke et al. “Photoinduced Melting of Antiferromagnetic Order in $\text{La}_{0.5}\text{Sr}_{1.5}\text{MnO}_4$ Measured Using Ultrafast Resonant Soft X-Ray Diffraction”. In: *Physical review letters* 106.21 (2011), p. 217401.
- [17] P Beaud et al. “Ultrafast structural phase transition driven by photoinduced melting of charge and orbital order”. In: *Physical review letters* 103.15 (2009), p. 155702.
- [18] A Caviezel et al. “Femtosecond dynamics of the structural transition in mixed valence manganites”. In: *Physical review. B, Condensed matter* 86.17 (2012), p. 174105.
- [19] H J Lee et al. “Optically induced lattice dynamics probed with ultrafast x-ray diffraction”. In: *Physical review. B, Condensed matter* 77.13 (2008), p. 132301.
- [20] Hirohiko Ichikawa et al. “Transient photoinduced hidden phase in a manganite”. In: *Nature materials* 10.2 (2011), pp. 101–105.

- [21] Z A Li et al. “A “checkerboard” orbital-stripe phase and charge ordering transitions in $\text{Pr}(\text{Sr}_x\text{Ca}_{2-x})\text{Mn}_2\text{O}_7$ ($0 \leq x \leq 0.45$)”. In: *Europhysics letters* 86.6 (2009), p. 67010.
- [22] Maximilian Eichberger et al. “Snapshots of cooperative atomic motions in the optical suppression of charge density waves”. In: *Nature* 468.7325 (2010), pp. 799–802.
- [23] Fabrizio Carbone, Oh-Hoon Kwon, and Ahmed H Zewail. “Dynamics of chemical bonding mapped by energy-resolved 4D electron microscopy”. In: *Science* 325.5937 (2009), pp. 181–184.
- [24] Fabrizio Carbone et al. “EELS femtosecond resolved in 4D ultrafast electron microscopy”. In: *Chemical physics letters* 468.4–6 (2009), pp. 107–111.
- [25] F Carbone et al. “A perspective on novel sources of ultrashort electron and X-ray pulses”. In: *Chemical physics* 392.1 (2012), pp. 1–9.
- [26] Yusuke Tokunaga et al. “Rotation of orbital stripes and the consequent charge-polarized state in bilayer manganites”. In: *Nature materials* 5.12 (2006), pp. 937–941.
- [27] Qing’an Li et al. “Reentrant orbital order and the true ground state of $\text{LaSr}_2\text{Mn}_2\text{O}_7$ ”. In: *Physical review letters* 98.16 (2007), p. 167201.
- [28] Brett Barwick et al. “4D imaging of transient structures and morphologies in ultrafast electron microscopy”. In: *Science* 322.5905 (2008), pp. 1227–1231.
- [29] Oh-Hoon Kwon et al. “Nanoscale mechanical drumming visualized by 4D electron microscopy”. In: *Nano letters* 8.11 (2008), pp. 3557–3562.
- [30] L. Piazza et al. “Ultrafast structural and electronic dynamics of the metallic phase in a layered manganite”. In: *Structural Dynamics* 1.1 (2014), p. 014501. DOI: 10.1063/1.4835116.
- [31] R F Egerton. “Electron energy-loss spectroscopy in the TEM”. In: *Reports on Progress in Physics* 72.1 (2009), p. 016502.

- [32] L Piazza et al. “Design and implementation of a fs-resolved transmission electron microscope based on thermionic gun technology”. In: *Chemical physics* 423.0 (2013), pp. 79–84.
- [33] Tad J Armstrong and Anil V Virkar. “Performance of Solid Oxide Fuel Cells with LSGM-LSM Composite Cathodes”. In: *Journal of the Electrochemical Society* 149.12 (2002), A1565–A1571.
- [34] C Hébert. “Practical aspects of running the WIEN2k code for electron spectroscopy”. In: *Micron* 38.1 (2007), pp. 12–28.
- [35] V J Keast. “Ab initio calculations of plasmons and interband transitions in the low-loss electron energy-loss spectrum”. In: *Journal of Electron Spectroscopy and Related Phenomena* 143.2–3 (2005), pp. 97–104.
- [36] <http://www.tcd.ie/Physics/people/Cormac.McGuinness/Cowan/>.
- [37] See supplementary material at <http://dx.doi.org/10.1063/1.4835116> for the details of the electronic structure calculations and the corresponding band diagram.
- [38] Fabrizio Carbone. “The interplay between structure and orbitals in the chemical bonding of graphite”. In: *Chemical physics letters* 496.4–6 (2010), pp. 291–295.

Chapter 3

Photo-induced near-field electron microscopy of nanostructures

In Chapter 1, Photo-induced near-field electron microscopy has been used for the characterization of the temporal resolution of the ultrafast microscope. In this chapter we will discuss some details about the technique itself and the constraints that should be fulfilled for make possible an energy gain by an electron transiting near an irradiated nanostructure.

In the second part we'll see how, combining some freedom in the configuration of the electron optics in the spectrometer and the ability of this technique to probe electric field distributions, it is possible to experimentally obtain a space-energy map that shows simultaneously wave-like and corpuscular behavior of an electromagnetic field supported by a surface plasmon.

Parts of this chapter are taken from *Simultaneous observation of the quantization and the interference pattern of a plasmonic near-field*, L. Piazza *et al*, Nature Communications, 6 6407, 2015, an extended introduction and more considerations are added.

Photons and electrons team up^{*}

The interaction between electrons and electromagnetic fields is a subject of research actually older than the official discovery of electrons themselves. German physicists Johann Hittorf and Eugen Goldstein observed and described what they called *cathode rays* in 1869 and 1876 respectively, but it was only in 1897 that J.J. Thomson showed that those rays were formed by a unique kind of negatively charged particles [2].

On the other hand, it is certainly true that the laser, from its invention in 1960 till its modern ultrafast and ultra-bright declinations, offered a unique tool for the study of matter and ceaselessly fueled innovative investigations.

Schilling and coworkers described first in 1974 the absorption of energy quanta by an electron beam, a process mediated by plasmons on the surface of a liquid indium sample. In their experiment the surface plasmons were induced by the incident beam of fast electrons itself and the result was a peak in the gain region of the spectrum of the reflected electrons (Figure 3.1). The separation between such a peak and the signal of the elastically scattered electrons was of about 8.4 eV, a value that mirrored to the well-known plasmonic absorption visible in the loss region of the same graph. They have shown, furthermore, that the efficiency of such an interaction critically depends on the angle between the electron beam and the plane that supports the surface plasmons ([3]).

Multi-photon absorption and emission in the presence of an intense electromagnetic field has been later observed by Weingartshofer and coworkers in 1977 ([4]). Their experimental setup was designed to study the interaction between an electron beam and a flux of Argon atoms under laser irradiation. The result of their spectroscopic observations was the symmetrical pattern of equally spaced peaks in the gain and loss region of the spectra depicted in Figure 3.2. The peaks were spaced by an energy matching the energy

^{*}García de Abajo, Nature 462.7275 (2009)[1].

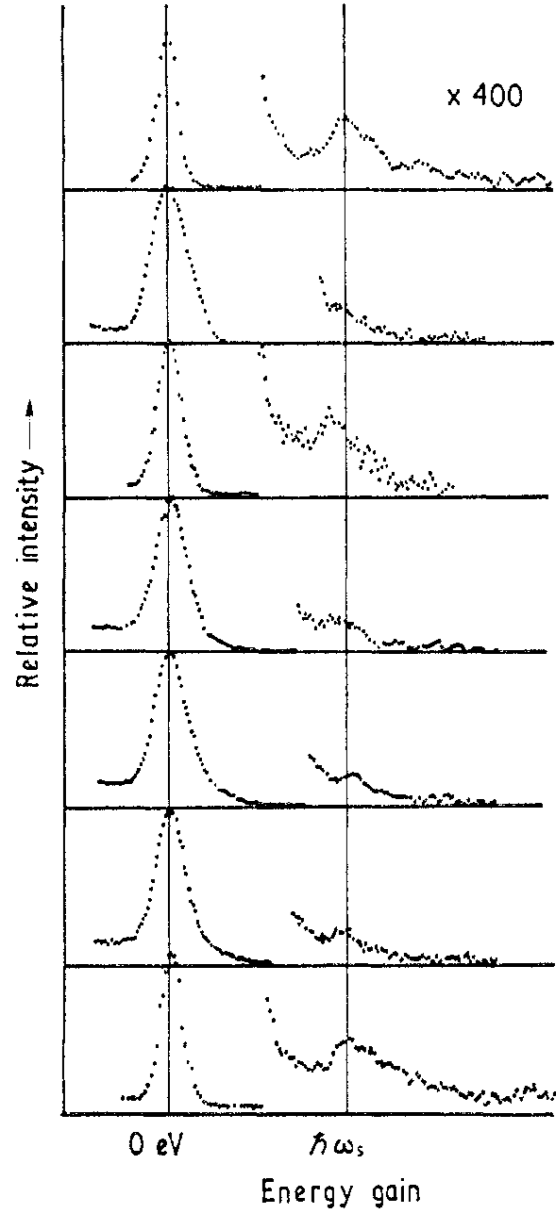


Figure 3.1: Series of energy gain spectra at an angle of incidence $\alpha = 88.5^\circ$. The peaks at $\hbar\omega_s = 8.4\text{eV}$ represent electrons which have gained one quantum of a surface plasmon. Image adapted from [3].

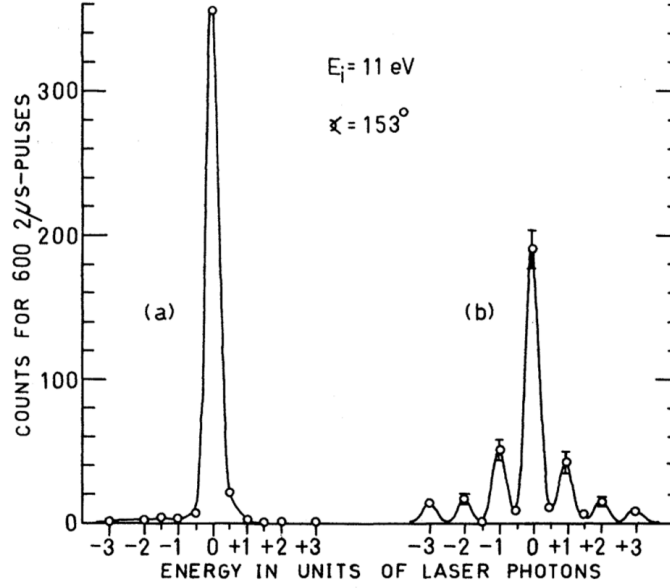


Figure 3.2: Energy-loss spectrum of e^- -Ar scattering. (a) Without laser field. (b) With laser field. Image adapted from [4].

of the photons generated by the CO_2 pulsed laser source and were present only when the Argon atoms and the infrared radiation were spatially and temporally superimposed to the electron beam.

In 2009 Barwick and coworkers reported multi-photon absorption and emission from plasmonic fields supported by nanostructures such as Carbon nanotubes and Silver nanowires and, at a later stage, by samples of different nature such as nanoparticles and biological samples like bacteria and protein vesicles [5, 6, 7]. The use of a post-column imaging energy filter and of an ultrafast laser source allowed an in-deep exploitation of the energy-gain process. With this setup not only the spectroscopic features of the interaction were accessible but also the real space distributions of the nanoscopic evanescent fields, their behavior in the picosecond timescale and the role played by the polarization of the incident laser field [5, 8].

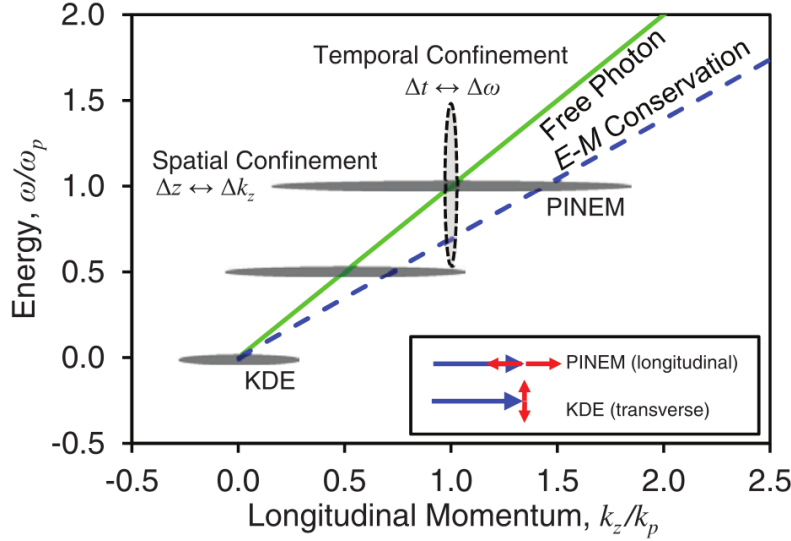


Figure 3.3: Energy-momentum conservation of free electron and free photon via momentum broadening (horizontal ellipses) due to spatial confinement and energy broadening (vertical ellipse) due to temporal confinement. The solid green line represents the dispersion relation of a free photon, and the dotted blue line represents the momentum change of a free electron at the given energy change. For PINEM, the electron changes its energy by a single-photon quantum and its momentum by a value larger than that of a free photon of the same energy. For the Kapitza-Dirac effect, the electron energy is unchanged, whereas the transverse momentum is changed by two quanta of photon momentum, and the longitudinal momentum is virtually unchanged (see the inset). Image adapted from [9].

Energy-momentum conservation

Net absorption/emission of photons by an electron in free space is forbidden due to energy/momentum conservation constraints. In the well-known Kapitza-Dirac effect [10, 11] an interaction with a standing wave still takes place in vacuum but it involves an even number of absorption and emission of photons, resulting in a zero energy exchange and only a transverse momentum variation for the scattered electrons [11].

To observe an interaction between electrons and photons with an effective exchange of energy it is necessary to introduce a spatial confinement for the electromagnetic field. This confinement, due to the Heisenberg's uncertainty principle $\Delta x_e \Delta p_e \geq \hbar/2$ imposes a spread of the momentum value that allows

Chapter 3. Photo-induced near-field electron microscopy

the necessary matching.

Figure 3.3 (adapted from the reference [9]) explains this concept; in the case of PINEM the gain in energy observed can be of tens of eV so, taking into account radiation in the visible or near infrared range, the confinement of the field has to be of micrometric to nanometric scale.

A spatial confinement of the electromagnetic field is necessary but not sufficient to guarantee an efficient coupling between photons and incident electrons.

Considering a photon of angular frequency ω_p and an electron with energy E_e after the absorption one should have:

$$E'_e = E_e + \hbar\omega_p \quad (3.1)$$

Since the energy of a relativistic electron is defined by:

$$E_e = \sqrt{c^2 p_e^2 + m_e^2 c^4} \quad (3.2)$$

if we represent

$$p_{\parallel} = \hbar k_p \sin \Theta \quad \text{and} \quad p_{\perp} = \hbar k_p \cos \Theta$$

as the two component of the momentum of the photon respect to the direction of propagation of the electron, the former relation becomes:

$$E_e + \hbar\omega_p = \sqrt{c^2(p_e + \hbar k_p \cos \Theta_c)^2 + c^2(\hbar k_p \sin \Theta_c)^2 + m_e^2 c^4} \quad (3.3)$$

where we call Θ_c the angle that supposedly satisfies the previous equation. Solving for Θ_c and considering that the group velocity of the electron $v_e = c^2 p_e / E_e$ and that the phase velocity of the photon $v_p = \omega_p / k_p$ we obtain the

following constraint:

$$\frac{v_p}{v_e} = \cos \Theta_c \leq 1. \quad (3.4)$$

This relation simply states that the phase velocity of the photon cannot exceed the group velocity of the electron. This is accomplished through the variation of k_p via the material, posing some restrictions on the properties of the dielectric function and on the angle Θ_c introduced before.

As showed in [9] a planar structure can sustain a limited plasmonic modes able to couple efficiently with incoming electrons, thus a structure with a more complex geometry able to sustain more plasmonic modes, such as a cylindrical nanowire or a spherical nanoparticle, is often required.

Finally, to obtain a detectable signal from this highly non-linear process, a high intensity of the stimulating field is necessary. In current instrumentation this is achieved confining in time the photon energy by means of the use of ultrashort laser pulses.

Simultaneous observation of the quantization and the interference pattern of a plasmonic near-field

Far-field electromagnetic radiation can be converted to localized electromagnetic energy through the excitation of so-called surface plasmon polaritons (SPPs) at the interface between a metal and a dielectric. The definition refers to the coupling between collective oscillations of electrons in the metal, i.e. surface plasmons, and the resulting radiated electromagnetic field, the polariton, which is evanescently confined in the direction perpendicular to the interface. The term polariton is used to define a field that is strongly coupled to a dipolar excitation, which in the case of SPPs is provided by the distribution of electrons in the metal[12]. While SPPs are bound to the metal surface in the perpendicular direction, they can propagate non-radiatively along the surface, and as such can be guided relatively unperturbed through bends, corners or virtually any arbitrary metallic nanostructure[13, 14, 15, 16]. Moreover, SPPs have been shown to be very sensitive to the refractive index of the local dielectric environment, allowing their properties to be tailored using applied electric or magnetic fields in composite nanomaterials systems.[17] In addition, in materials that exhibit exotic electronic properties due to dimensional confinement, SPPs exhibit unique features such as low loss propagation and an unusually high modal index [18, 19, 20]. Such phenomena are widely investigated because of their potential application in nanophotonic circuits, where sub-wavelength guiding of the electromagnetic field is crucial to miniaturization[21, 22].

For these reasons, a great deal of attention is currently devoted to the observation of SPPs at the nanoscale. Optical near-field techniques can be used to image evanescent fields on surfaces reaching sub-wavelength spatial resolution in the most advanced set-ups[23, 24, 25], but involve significant drawbacks in terms of signal intensity, the necessity of point-by-point acquisitions and the potential influence of the scanning tip on the electromagnetic near-

field being probed. In electron microscopy, imaging through electron energy loss spectroscopy (EELS) has proven successful in mapping SPPs confined by nanostructures with nm resolution[26, 27, 28], and recently Rossouw and Botton imaged electron-excited, Fabry-Pérot-type SPP standing waves in isolated nanowires using a combined scanning transmission electron microscopy (STEM)-EELS approach[29, 16].

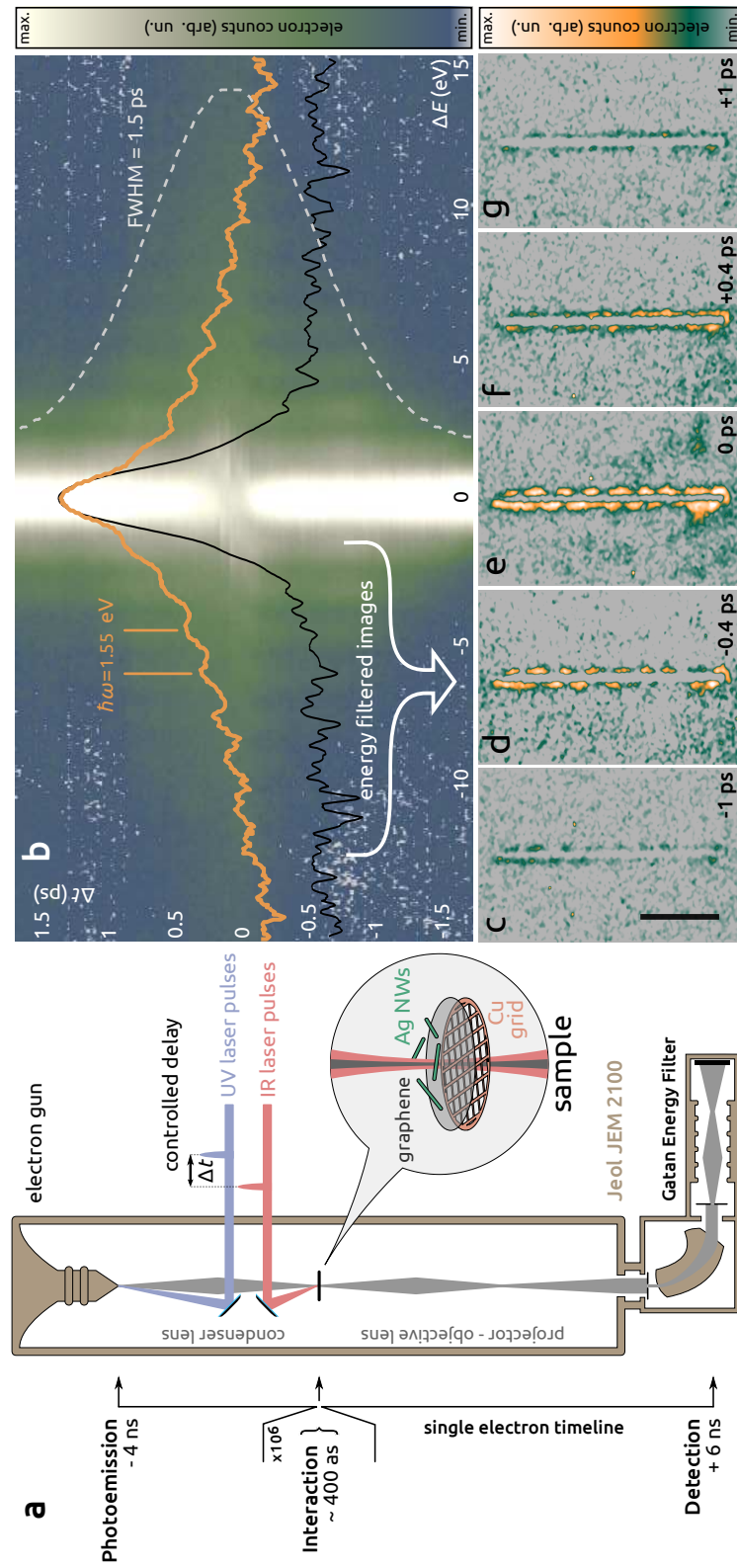
Alternatively, photoexcitation and subsequent EELS imaging of SPPs using the time-resolved photon-induced near field electron microscopy (PINEM) technique has recently demonstrated additional control of the SPP properties, as well as the possibility to film their evolution in the femtosecond (fs) time domain[30, 31]. These experiments allow the observation of SPPs in multiple dimensions; space, energy and time, yielding unprecedented insight into their fundamental properties.

In the present work a SPP standing wave is photoinduced on an isolated metallic nanowire using an intense fs laser pulse, and the ability to control its spatial interference pattern is demonstrated by tuning the polarization of the excitation light. A snapshot of the interaction between the imaging electrons and the SPP standing wave is taken using a new ultrafast-imaging methodology that utilizes an electron imaging filter[32] to form a 2D projection of one spatial coordinate versus electron energy. These energy-space-resolved images simultaneously yield both the quantization of the photoinduced SPP field and its characteristic Fabry-Pérot (FP) interference pattern, given by the one-dimensional confinement of the single nanowire.

Results

SPP imaging

When irradiated by light, isolated metallic nanowires have been shown to behave as quasi-one-dimensional plasmonic nano-antennas, whose radiation



Quantization and the interference of a plasmonic near-field

Figure 3.4: **PINEM on a single nanowire.** (a) A schematic of the experimental set-up. Light and electron pulses at a variable time delay are spatially overlapped on an isolated Ag nanowire suspended on a TEM grid with a few-layer graphene support layer. Probing electrons are detected using a CCD camera after passing through an electron imaging filter. (b) Map of the electron-energy loss intensity versus the relative time delay Δt between the optical pump and electron probe pulses, taken on a single photoexcited nanowire (5.7 μm length, $\simeq 67$ nm radius). Excitation wavelength and polarization angle are 800 nm and $\varphi = 45^\circ$, respectively. Energy spectra at negative ($\Delta t = -1.6$ ps, black trace) and zero delay ($\Delta t = 0$ ps, orange trace) are superimposed. The intensity in both the map and the spectra is plotted on a logarithmic scale. (c-g) Snapshots of an isolated nanowire at different time delays obtained using only the electrons that have gained energy; i.e. those in the region indicated by the white arrow in panel b. Electron counts are on a linear scale. The vertical scale bar in panel c corresponds to $2\mu\text{m}$ and holds for all images. Image adapted from [33].

patterns are governed by the properties of the excitation (wavelength, incident and polarization angles) and their geometry with respect to the orientation and aspect ratio of the wire[34, 35]. The incident light photoexcites propagating SPPs in the metallic nanowire whose back-and-forth reflections from the wire ends give rise to a SPP standing wave, making the straight nanowire the plasmonic equivalent of a FP nanoresonator[25]. In general, the confined electromagnetic fields of such SPP standing waves, whether electron- or photoinduced, are captured through scanning-based techniques such as combined STEM-EELS[29, 16, 36] or scanning near-field optical microscopy (SNOM)[37], which probe the electric near-field component perpendicular to the sample plane. Here, we alternatively employ a fundamentally different, field-of-view approach, based on ultrafast transmission electron microscopy (UTEM).

UTEM is typically performed by modifying a conventional transmission electron microscope (TEM) such that ultrashort bunches of imaging electrons, containing at most one particle each[38, 39], can be photoemitted from the cathode by fs laser pulses. Optical access is also provided for photoexcitation of the specimen, and the delay between the two pulse trains is controlled via an optical delay line, allowing for time-resolved optical-pump/electron-probe experiments (see Figure 3.4a and Methods)[39, 40]. When the specimen being imaged is a (metallic) nanostructure, the temporal and spatial evolu-

Chapter 3. Photo-induced near-field electron microscopy

tion of a photoinduced SPP standing wave can be visualized via the PINEM imaging technique[30, 31]. PINEM relies on the inelastic exchange of energy quanta between the photoinduced electromagnetic SPP wave and the relativistic imaging electrons, which probe the SPP electric field component along the electron propagation direction[41, 42, 43, 44, 45, 31]. In our experiments, Ag nanowires (~ 50 nm radius, few- μm length) are isolated and dispersed on a graphene-covered TEM grid and photoexcited using a pulsed 800 nm laser beam at a 5 mJ cm^{-2} fluence, corresponding to a peak excitation energy density of $\simeq 10 \text{ GW cm}^{-2}$. Under these experimental conditions excitation of SPPs by the electron probe beam is a much weaker effect, which can be considered entirely negligible[44]. The few-layer graphene substrate is used to efficiently dissipate the laser-induced heat.

Figure 1b shows the energy spectra of the probing electrons before and after interaction with an isolated, photoexcited Ag nanowire. The spectrum at negative delay ($\Delta t = -1.6 \text{ ps}$) shows the initial energy distribution of the electron bunches, i.e. the zero-loss peak (ZLP), whose full-width-half-maximum (FWHM) determines the spectral electron-energy resolution as better than 1.1 eV. By contrast, when the optical pump and electron probe are overlapped ($\Delta t = 0 \text{ ps}$), the interaction with the photoinduced SPP electric field leads to acceleration (deceleration) of the probing electrons, and the corresponding quantized gain (loss) of energy (peaks found at $\Delta E = \pm n \cdot \hbar\omega$). In the resulting electron-energy spectrum the (net) exchange of up to 9 energy quanta can be observed. The panel further depicts the continuous temporal evolution of this electron-energy spectrum as a function of Δt , showing a 1.5 picosecond (ps) FWHM cross-correlation of the optical pump and electron probe pulses. As was previously shown, when optimally configured for time-resolution the same system can readily achieve a sub-ps temporal cross-correlation.[39]

The electromagnetic field of the photoexcited SPP in the nanowire can be captured by using an imaging energy filter to select out only electrons that have gained energy (see white arrow in Figure 3.4b), and subsequently re-

forming an image. Repeating this procedure at different time delays produces a series of images (Figure 3.4c-g) of the temporal evolution of the SPP field, showing its interferometric standing wave pattern in the silver FP nanoresonator. This type of modal interference pattern reveals the wave character of the electromagnetic SPP field, and is typically observed when the properties of light excitation (wavelength and polarization) are close to a resonance condition of the excited nanowire.

Plasmonic nanoresonators

For symmetry reasons, light at normal incidence that is polarized parallel to the wire long axis exclusively excites odd order SPP modes, i.e. modes that have an odd number of SPP field nodes m [25]. By contrast, electron-excitation of SPPs involves no such symmetry-based selection rules, such that in STEM-EELS both odd and even order SPP modes can be excited. In order to be able to photo-excite even order SPP modes as well, one requires an excitation geometry where the light is incident at an oblique angle and the azimuthal angle between the light polarization and the wire long axis is nonzero[25]. In general, under such photo-excitation conditions (in s-configuration), different SPP modes can be excited at the same time. This can result in non-trivial photoinduced SPP field distributions, which require numerical simulations in order to reproduce and understand them[24]. As shown in Figure 3.5, these general selection rules are valid for the photoexcitation of SPPs in PINEM as well. First, we image a $3.4\text{ }\mu\text{m}$ long, $\simeq 45\text{ nm}$ radius nanowire, illuminated by s -polarized light with an azimuthal angle of $\varphi = 0^\circ$ with respect to the wire long axis, see Figure 3.5a-b. The resulting photoinduced SPP standing wave corresponds to an odd order mode ($m = 11$), in excellent agreement with preceding reports[25, 35, 24], and with our own finite element simulation (see Methods) shown in Figure 3.5c. The experimentally estimated SPP wavelength ($\lambda_{\text{SPP}}^{\text{exp.}} = 2d^{\text{av.}}$) and wavevector ($k_{\text{SPP}}^{\text{exp.}} = \pi/d^{\text{av.}}$) for this mode are $\simeq 615\text{ nm}$ and $\simeq 10.2\text{ }\mu\text{m}^{-1}$, respectively, from the average antinode distance $d^{\text{av.}} \simeq 308\text{ nm}$ in the standing wave pat-

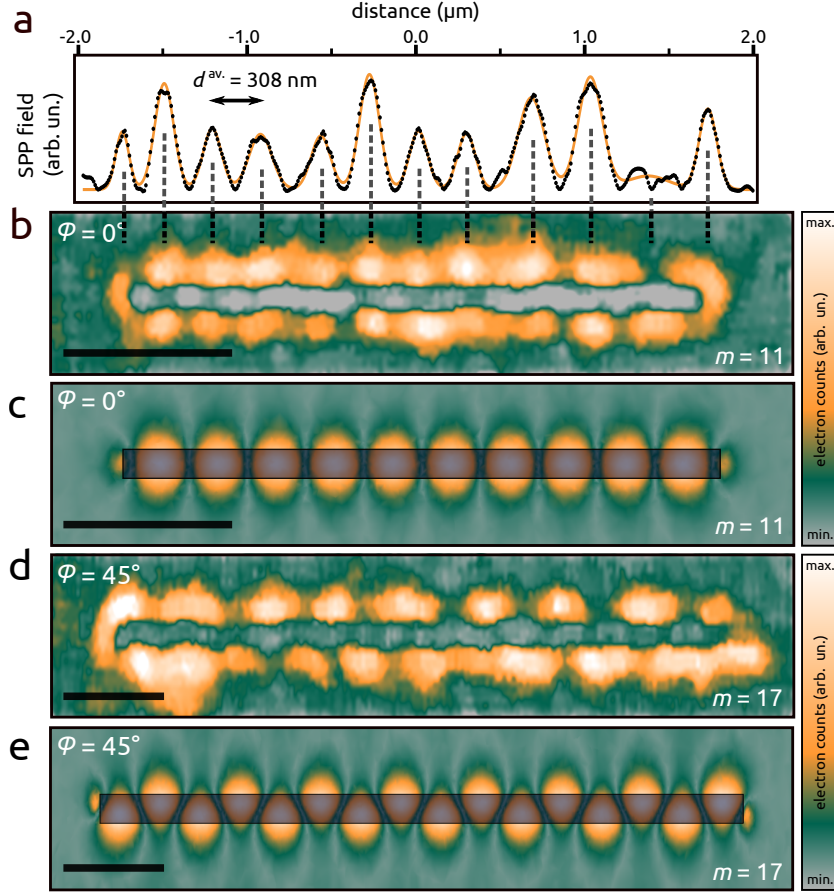


Figure 3.5: **Control of the surface plasmon-polariton field.** (a) Spatial variation of the interferometric SPP field along the axis of the nanowire imaged in panel b. Black data points depict the background-subtracted SPP field strength integrated along the transverse direction, with the average distance between antinodes $d^{av.}$ determined from a multi-Gaussian fit (solid line). (b) Experimental PINEM image of the photoinduced SPP field distribution on an isolated nanowire (3.4 μm length, ≈ 45 nm radius) with light excitation polarized parallel to its longitudinal axis (800 nm, $\varphi = 0^\circ$). The image was recorded at $\Delta t = 0$ ps, using only electrons that have gained energy. Electron counts in panels b-e are plotted using the same linear color scale. The scale bar corresponds to 1 μm. (c) Corresponding finite-element simulation of the SPP field ($|E_z|$ in the plane 10 nm below the wire) in the 800 nm, $\varphi = 0^\circ$ geometry. The shaded area indicates the spatial projection of the nanowire, and the scale bar corresponds to 1 μm. (d) Experimental PINEM image of the SPP field distribution (at $\Delta t = 0$ ps, using only electrons that have gained energy) on an isolated nanowire (5.7 μm length, ≈ 67 nm radius) under 800 nm, $\varphi = 45^\circ$ excitation. The scale bar corresponds to 1 μm. Different wires were used for the two polarizations. (e) Corresponding finite-element simulation of the SPP field ($|E_z|$ in the plane 10 nm below the wire) in the 800 nm, $\varphi = 45^\circ$ geometry. The shaded area indicates the spatial projection of the nanowire, and the scale bar corresponds to 1 μm. Image adapted from [33].

tern (see the spatial profile in Figure 3.5a). At an energy of 1.55 eV, this is in excellent agreement with both calculated and experimental dispersion curves of resonant SPP waves in silver nanoantennae[46, 29, 24, 16]. In general, the resonance condition of an order- m SPP mode in a one-dimensional FP resonator of length L can be written as[25, 29]:

$$\frac{2L}{\lambda_{\text{SPP}}} + 2\delta\theta = m, \quad (3.5)$$

where $\delta\theta$ is the SPP phase shift upon reflection from the resonator ends, which is often negligible for higher order modes[29, 24]. Calculating the expected SPP wavelength for a resonant mode of order $m = 11$ in an idealized one-dimensional FP resonator of length $L = 3.4\mu\text{m}$ ($\delta\theta = 0$) yields a value of 618.2 nm, which is in good agreement with the estimated $\lambda_{\text{SPP}}^{\text{exp.}}$. The slight difference, disregarding the estimation error margin, would imply a negative reflection phase shift $\delta\theta$ according to equation 3.5. However, it is more intuitively interpreted in terms of a shortened effective wire length $L^{\text{eff.}}$, resulting from the fact that the hemispherical wire caps were included in the determination of L [25, 29].

Next we illuminate a $5.7\mu\text{m}$ long nanowire using light polarized at a $\varphi = 45^\circ$ azimuthal angle, obtaining a non-trivial SPP field distribution in which antinodes of opposite phase are concentrated on alternating sides of the wire (Figure 3.5d). Under these excitation conditions, the nodal lines are clearly at an angle with respect to the long axis of the nanowire. As shown in Figure 2e, the features of this transversally asymmetric SPP mode ($m = 17$) are numerically accounted for by our finite-element simulations. To our knowledge, the experimental observation of such an asymmetric distribution of the SPP field using either SNOM or STEM-EELS techniques has never been reported. In principle these features could also be observed in SNOM experiments[25]. The absence of such asymmetric field distributions in STEM-EELS experiments is likely related to the differences between electron- and photoexcitation of SPPs in terms of mechanism and selection rules[43, 44, 45, 31, 36]. For photoexcited SPP modes, Dorfmueller *et al.*[25, 35] showed that while

odd order modes emit the strongest field in the direction perpendicular to the nanowire, thus maximizing the PINEM effect, the even order modes have a minimum of radiation in this direction, resulting in a more difficult detection. However, at the same time the relative dipole coupling strength of odd order modes was shown to quickly decrease with m , while staying fairly constant for even order modes. In our experiments, two different nanowires were used, in order to maximize the strength of the photoinduced SPP field in the different excitation geometries. The excellent agreement between the experimental and simulated SPP field distributions demonstrates the potential of controlling SPPs using an external light field.

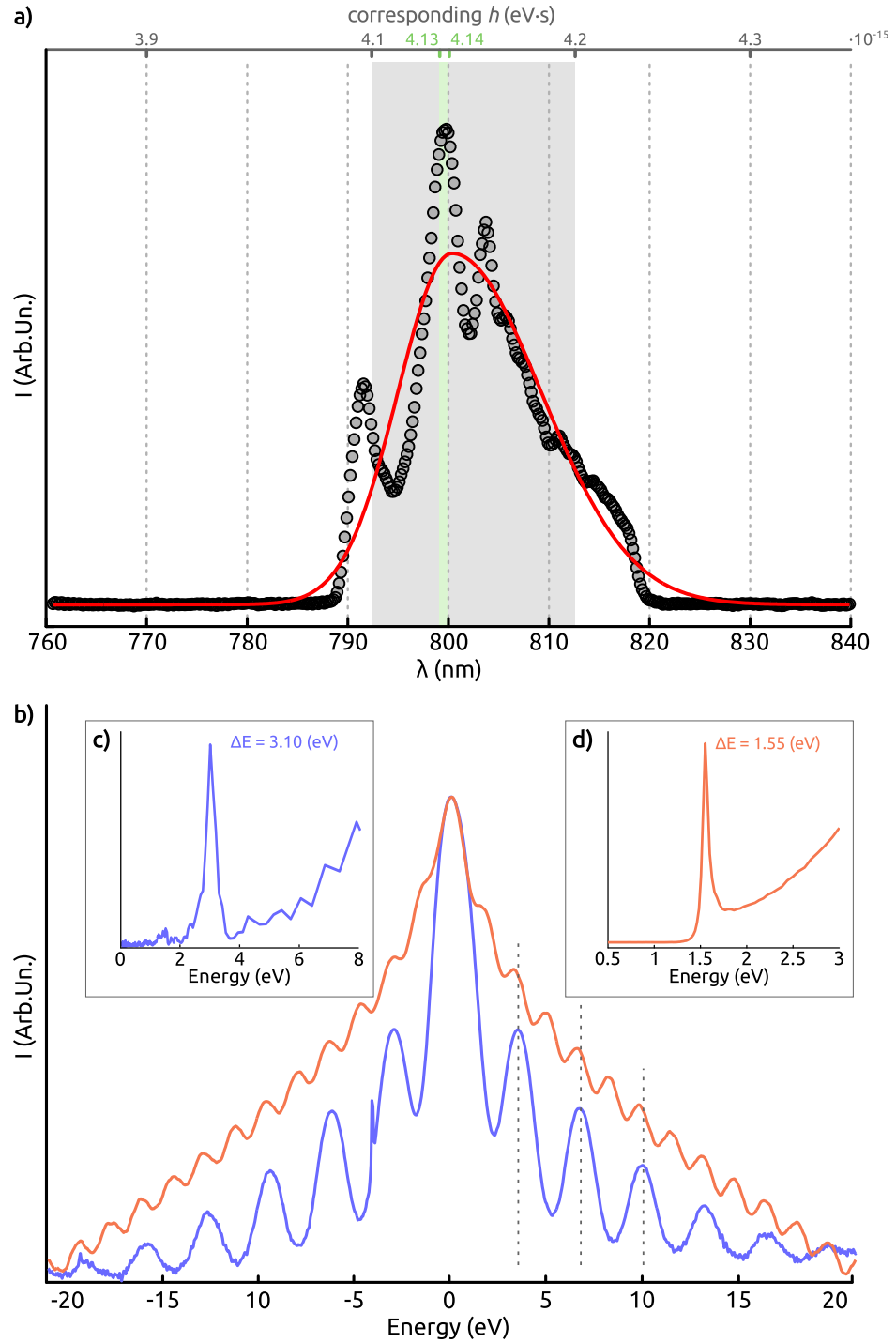
Experimental estimate of Planck's constant

Theoretically, electron energy loss spectroscopy (EELS) and electron energy gain spectroscopy (EEGS) can be treated in a similar formalism as stimulated absorption and either spontaneous or stimulated emission[16, 45, 41, 44]. While a complete description of the process would be in terms of quantum electrodynamics (QED), in practice the full machinery of QED is unnecessary to describe the interaction, and most treatments[45, 41, 44] of EELS/EEGS use a semiclassical formalism, which is still essentially quantum mechanical, because the experimental spectra cannot be reproduced without invoking Planck's constant in the form of a quantized energy gain/loss $\Delta E = \pm n \cdot h\nu$. To illustrate this point, we show that the spectrum in Figure 3.4b can yield Planck's constant itself. By taking the wavelength of the pump light pulse, the spectrum of which is depicted in Figure 3.6a, and determining the precise spacing between the multiple PINEM peaks ($\Delta E = 1.55$ eV, see Figure 3.6d), h can be obtained through the formula $h = \lambda \Delta E / c$. Underlining the robustness of this method, the corresponding PINEM spectrum from the same nano-structure, obtained when using a frequency-double pump (400nm), yields an equivalent estimation of h . The precision of the absolute value obtained for h depends on the combined accuracy in the determination of the laser central wavelength and the energy gain/loss peak spacing.

In our experiments, a 30 nm broad laser spectrum is used to induce a SPP whose k -vector lies parallel to the length of the nanowire on which it is confined. The combined uncertainty of localizing along the wire length ($\Delta x = 3\mu\text{m}$) a wave-packet with a $\Delta\lambda = 30$ nm yields a value $\Delta x\Delta p \simeq 9.3 \cdot 10^{-35}$ J · s, which is on the order of $\hbar/2$ ($5.3 \cdot 10^{-35}$ J · s). The near-field radiated by the photoinduced plasmon accelerates/decelerates the imaging electrons, resulting in their velocity distribution measured by the spectrometer. However, it should be noted here that the momentum imparted to the electrons along the z direction does not reveal the momentum direction of the SPP field imaged. The latter is determined by the k -vector of the field confined on the surface of the nanowire. The acceleration/deceleration of the electrons emerges from their interaction with the component of the electric field parallel to their propagation. In the electron propagation direction (z), the accuracy in measuring the changes in momentum imparted to the electrons by the field is given by the energy resolution of the experiment ($\Delta E = 1$ eV). The complementary variable in this case is the precision in the temporal localization of the plasmonic field on the nanowire, which is given by the time that the 200 keV electrons take to cross the wire and image the interaction with the field ($\Delta t = 400 \cdot 10^{-18}$ s). In this case, the combined uncertainty $\Delta t\Delta E \simeq 6.4 \cdot 10^{-35}$ J · s is also on the order of $\hbar/2$. One should note here that the temporal resolution of the experiment in this scenario plays no role other than providing the high peak intensities of the fields necessary for the interaction to occur.

Energy-space SPP mapping

After interacting with the photoinduced SPP field, the imaging electrons carry all the information about the exchange encoded in their spatial and energy distributions. In electron energy loss spectroscopy (EELS) and 2D energy-filtered imaging, one typically collapses one or more of these coordinates to obtain either a 1D energy spectrum (collapsing both spatial coordinates) or a 2D image (collapsing the electron energy). Instead, to simul-



Quantization and the interference of a plasmonic near-field

Figure 3.6: **Measurement of h .** **a**, The output spectrum of the Ti:Sapphire laser amplifier (grey symbols) is shown together with an asymmetric gaussian fit (split normal distribution, solid red line) at $\lambda = 800$ nm. The upper horizontal scale indicates the extracted h -value corresponding to the different wavelengths, given the value $E = 1.55$ eV determined in panel d. The green shaded area shows the λ -range corresponding to second decimal precision of h , and the light grey shading represents the λ -range corresponding to one decimal precision. **b**, PINEM spectra obtained photoexciting a silver nanowire with 800 nm light (red line) and 400 nm light (blue line). **c-d**, The Fourier transform of the PINEM spectra shown in panel b, yielding an energy spacing between the peaks of 1.55 eV and 3.10 eV.

taneously observe both the quantized spectrum and its spatial distribution, here we resonantly excite an odd SPP mode in an isolated nanowire and align the corresponding image such that the wire long axis is parallel with the vertical detector axis (see Figure 3.7a). By then collapsing only the perpendicular (horizontal) spatial coordinate, we obtain an image that contains spectroscopic information along the horizontal detector axis and spatial information along the vertical detector axis. The experimental energy-space map is shown in Figure 3.7b. In order to optimally resolve the inelastic exchange process, we zoomed in on a selected section of the nanowire (4.6 μm length, $\simeq 61$ nm radius, $\varphi = 0^\circ$). As is clear from the experimental image, taking a horizontal cut (horizontal dashed line) yields the quantized spectrum of the interaction between the SPP field and the imaging electrons. At the same time, by taking a vertical cut at an energy corresponding to one of the peaks in the energy spectrum (vertical dashed line), the spatial distribution of the interaction between single electrons and a discrete number of photons is obtained, Figure 3.7c, displaying the typical interference fringes of the resonant SPP standing wave. Though both the wave and particle character of SPPs were already observed separately in individual, tailored experiments[47, 48, 49], here we obtain a very direct and illustrative view of both aspects of the SPP field simultaneously in a single experiment.

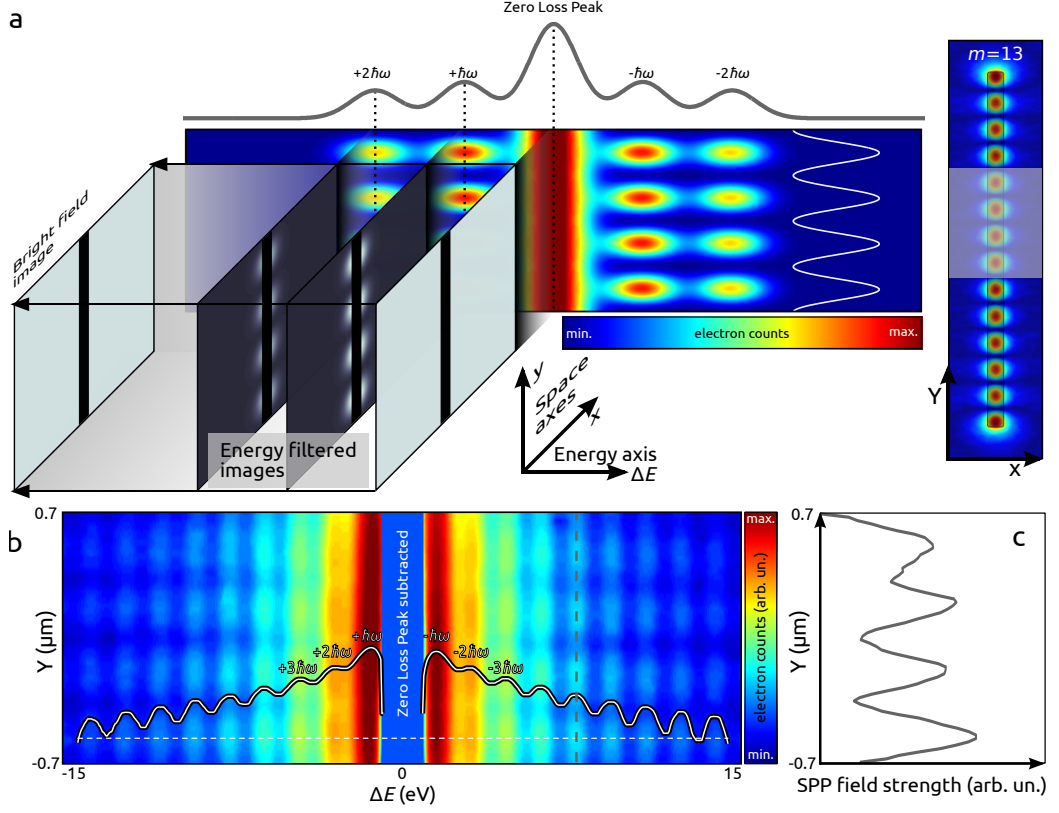


Figure 3.7: Energy-space imaging. (a) Conceptual representation of the energy-space resolved PINEM methodology. Rather than recording an energy-filtered 2D spatial map of the transmitted electrons (images on the left), or dispersing the electrons only in energy (spectrum on top), this method retains the spatial electron distribution along the vertical axis, while also dispersing the electrons according to their energy along the horizontal axis. Combined with the PINEM effect, this results in the vertical spatial variation of the photoinduced SPP field being duplicated at equidistantly spaced energy quanta, with an intensity envelope and energy resolution determined by the PINEM interaction strength and the ZLP-width, respectively. The vertical spatial variation here (solid white trace) corresponds to a selected part (white shaded area) of the simulated photoinduced field ($|E_z|$ in the plane 10 nm below the wire) of an isolated nanowire (black shaded rectangle, $4.6\mu\text{m}$ length, $\simeq 61$ nm radius, 800 nm excitation, $\varphi = 0^\circ$, $m = 13$), indicated on the right. Electron counts in both images are plotted on the same linear scale. (b) The experimentally obtained energy-space image, taken on a selected section of a photoexcited nanowire ($4.6\mu\text{m}$ length, $\simeq 61$ nm radius, 800 nm excitation, $\varphi = 0^\circ$, $\Delta t = 0$ ps) is displayed together with a horizontal cut (along the energy axis, white dashed line), showing the quantized energy dependence of the interferometric spatial distribution of the SPP field. A Gaussian-fitted ZLP peak was subtracted and the intensity (electron counts) is mapped on a logarithmic scale in both the image and the spectrum to enhance the contrast. (c) A vertical cross-section at the energy corresponding to the net exchange of five photons (grey dashed line in panel b) is shown, depicting the spatial distribution of the plasmonic field with its characteristic interference fringes. Image adapted from [33].

Discussion

It is important to clarify that the PINEM energy-space map shown in Figure 3.7b is fundamentally different from those previously obtained in STEM-EELS experiments[29, 16, 36, 50]. In the latter, the transient field of the fast electron probe excites all the different SPP modes across a wide energy range. Accordingly, the multiple peaks observed in the electron energy distribution correspond to the different odd and even order SPP resonances of the excited nanoresonator, and energy-filtered imaging centered on these different SPP resonances visualizes their correspondingly different spatial field distributions. By contrast, in PINEM the SPP modes are excited by light with a fixed wavelength, which selectively drives only the SPP modes at the corresponding energy, and even then only when they are symmetry-matched to the excitation geometry. Any optically driven SPP mode thus has an energy equal to that of the incident photons, which is retrieved as the energy-spacing of the series of equidistant peaks in the electron energy gain/loss spectrum of a PINEM experiment (see Figure 3.4b). Rather than being related to the different eigenmodes of the FP nanoresonator, these peaks correspond to the exchange of different discrete numbers of SPP-field quanta with the probing electrons. As a consequence, regardless of the relative electron energy at which one images, the observed SPP field distribution corresponds to the optically driven mode (see Figure 3.7b).

In order to explore the different SPP modes of the nanoresonator using PINEM, one would perform a series of PINEM imaging experiments while varying the wavelength of the light excitation. The simulation in Figure 4a, carried out for light polarized parallel to the wire long axis (2 μm length, 40 nm radius), illustrates the typical wavelength dependence of the strength of the photoinduced SPP field, and highlights the resonant SPP field distributions. In agreement with previous experiments and simulations[25, 35, 24], only odd order SPP modes are photoexcited in this $\varphi = 0^\circ$ excitation geometry. A PINEM experiment at a single wavelength allows one to selectively photoexcite a single SPP mode (circled in Figure 3.8a), which then exchanges

Chapter 3. Photo-induced near-field electron microscopy

energy quanta corresponding to that free space wavelength with the probing electrons, yielding the equidistantly peaked electron energy spectrum shown in Figure 3.8b. Aligning a nanoresonator supporting such a single photoexcited SPP mode along the vertical detector axis, and simultaneously projecting out the spatial and energy distribution of the probing electrons along the vertical and horizontal detector axes, respectively, yields the energy-space map that showcases the wave-particle duality of the SPP (see Figures 3b and 4b).

Due to the strong optical excitation in PINEM, even when the excitation wavelength falls between the SPP resonant conditions of a nanoresonator, the inelastic exchange of energy quanta can be observed. Corresponding energy-filtered PINEM images can thus provide the spatial distribution of the optically driven SPP near-field away from a FP resonance. This approach is in principle only limited by the optical damage threshold of the nanoresonator. The additional control offered by the tunability of the laser excitation intensity enables the possibility to enhance these off-resonance excitations, providing high contrast and high resolution images of their spatial field distribution. Another advantage of using PINEM to image plasmonic field distributions, in contrast to scanning-based conventional STEM-EELS imaging, is the capability of capturing the dynamics of the photoinduced SPP fields with fs resolution[30, 31].

Summarizing, in ultrafast energy-filtered PINEM imaging each pulse contains at most one electron to avoid space-charge broadening, and the electrons that exchanged quanta with the photoinduced SPP field carry the information about the interaction between one single electron and a discrete number of exchanged photons. An intriguing consequence is that by imaging the energy spectrum of such an exchange as well as its spatial distribution at the same time, one can obtain simultaneous information on complementary aspects of the confined electromagnetic field[51, 52, 53]. The wave aspect of surface plasmon polaritons was previously established in a SPP-analogue to Young’s famous double-slit experiment[47]. Furthermore, SPPs have also been shown

to be quantized in the same way as the free space electromagnetic field (i.e. light), manifesting similar quantum behavior including entanglement[54] and two-plasmon quantum interference[49, 55]. Recently, single surface plasmon polaritons were shown to exhibit both wave and particle behavior, in a set of individual measurements[48]. Our experiments provide a simultaneous observation of these two aspects of the SPP field in a single measurement and demonstrate the ability of a UTEM to image and control SPPs in multiple dimensions of space, energy and time, yielding further insight into their behaviour, and providing a unique playground for the observation of the fundamental properties of confined electromagnetic fields.

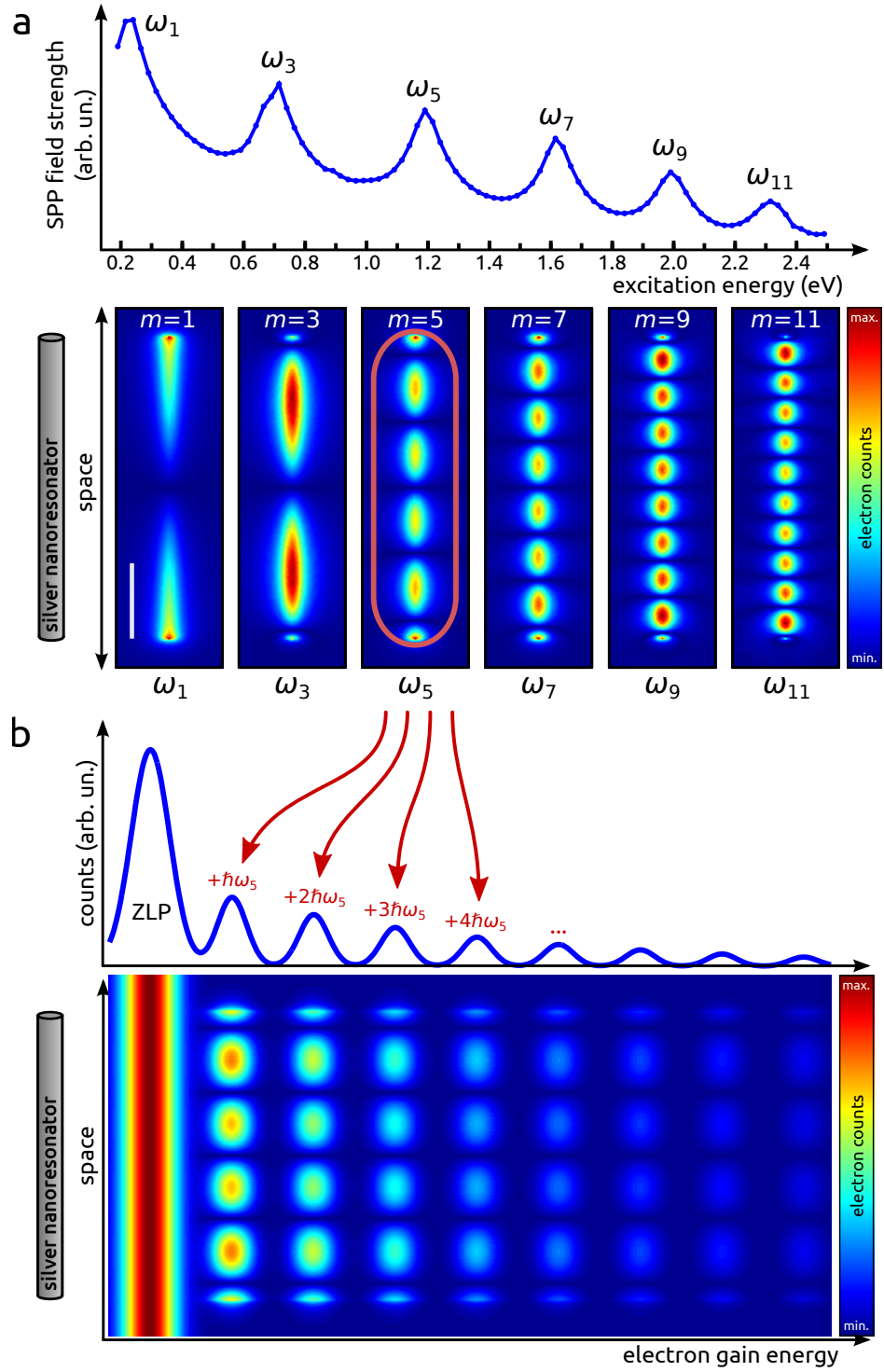
Methods

Sample preparation

Hemispherically capped silver nanowires (radii ~ 50 nm, varying lengths on the order of a few- μm)[56] were dispersed in dimethylformamide (DMF, Acros Organics, 99.95% purity) through ultrasonification for 10 minutes. Samples were prepared by dropcasting a single drop of the resulting suspension on a 300-mesh copper TEM grid covered by a few-layer graphene support film on lacey carbon (Ted Pella, 21740), immediately following ultrasonification. TEM-grids were then air-dried for a minimum of 4 hours before examination in the UTEM (at 295 K and $\sim 10^{-5}$ Pa) for identification and characterization of isolated silver nanowires.

Experimental apparatus

A 500 kHz train of linearly polarized, 800 nm, 80 fs light pulses was split to generate two beams. One of these beams was frequency-tripled to deliver few-nJ UV pulses that were used to photoemit electrons from the custom



Quantization and the interference of a plasmonic near-field

Figure 3.8: **Excitation energy dependent imaging versus energy-space imaging.** (a) Finite-element simulation of the excitation energy dependence of the photoinduced SPP field strength ($\log_{10} |E_z|$ integrated over the volume surrounding the nanowire) in a $\varphi = 0^\circ$ normal incidence excitation geometry. The simulated nanowire length and radius are $2\mu\text{m}$ and 40 nm , respectively. Representative spatial field distributions of the various odd-order SPP resonances are shown below ($|E_z|$ in the plane 10 nm below the wire), with electron counts plotted using the same linear color scale. The vertical scale bar in the image of the $m = 1$ SPP mode corresponds to 500 nm and holds for all images. (b) Selectively photo-exciting only one of the SPP modes of this wire (here $m = 5$) in a single wavelength PINEM experiment instead (at ω_5 , $\varphi = 0^\circ$) quantizes the energy exchange of its field distribution with the probing electrons, as shown in this conceptual PINEM energy-space map. The corresponding electron energy gain spectrum is depicted on the top. Electron counts in both the map and the spectrum are plotted on a linear scale. Though not shown here, a similar series of quantized features is present on the energy loss side of the ZLP in both the energy-space map and the spectrum. Image adapted from [33].

truncated-cone LaB_6 tip ($15\mu\text{m}$ diameter truncation plane, AP-Tech) of the thermionic electron gun in a modified JEOL JEM 2100 microscope.[39] The other 800 nm pulsed laser beam was passed through an optical delay line and focused on the sample in the UTEM at near-normal incidence such that photoexcitation in the field of view of the photoelectron beam was uniform. Corresponding optical fluences ranged between tens of $\mu\text{J cm}^{-2}$ and 5 mJ cm^{-2} . The experimental apparatus is equipped with a post-column Gatan Quantum GIF electron energy loss spectrometer (GIF)[32], and is pictorially represented in Figure 3.4a. A detailed description and characterization of the system can be found elsewhere[39]. For the PINEM experiments described in this work, the UTEM was operated at 200 keV in photoelectron mode. The GIF imaging camera was operated with a $0.05\text{ eV channel}^{-1}$ dispersion setting, and typical exposure times of the 2048×2048 pixel CCD sensor were 60 s for images and 10 s for spectra. PINEM energy spectra were aligned using a differential-based maximum intensity alignment algorithm, and where appropriate the zero loss peak (ZLP) was removed by subtraction of a fitted Gaussian line profile.

Finite-element simulations

The plasmonic near-field around the silver nanowires was calculated using a commercial fast finite-element software (COMSOL Multiphysics 4.3b, www.comsol.com), using the Wave Optics package, performing two sequential frequency domain studies. Nanowires were modeled as flat-ended cylinders of varying length and radius, whose complex and wavelength dependent refractive index was taken from Palik[57]. The nanoscatterer was surrounded by a rectangular volume of vacuum (index of refraction taken as 1), which itself was surrounded by perfectly matched layers (layer thickness 150 nm, minimum clearance to nanowire 250 nm) to absorb scattered light and minimize reflections. In a two-step calculation, first the distribution of the excitation electromagnetic field was calculated throughout the physical simulation volume (in the absence of the nanowire). The excitation was modeled as a linearly polarized plane wave incident on the rectangular input port above the scatterer (positive z) and absorbed at the corresponding output port below the scatterer (negative z). Floquet boundary conditions were imposed on the lateral boundaries of the simulation volume. The resulting electric field was then used as the background field in the second calculation, which solved for the electric field scattered by the nanowire. The maximum mesh element size on the nanowire surface was set to 30 nm, and the meshing of all other domains was chosen to optimize both the computational time and the accuracy of the calculation, similar to the procedure described by Miljković *et al.*[24].

References

- [1] F Javier García de Abajo. “Microscopy: Photons and electrons team up”. In: *Nature* 462.7275 (2009), p. 861.
- [2] J J Thomson. “XL. Cathode Rays”. In: *Philosophical Magazine Series* 5 44.269 (1897), pp. 293–316.

- [3] J Schilling and H Raether. “Energy gain of fast electrons interacting with surface plasmons”. In: *Journal of Physics C: Solid State Physics* 6.18 (1973), p. L358.
- [4] A Weingartshofer et al. “Direct Observation of Multiphoton Processes in Laser-Induced Free-Free Transitions”. In: *Physical review letters* 39.5 (1977), pp. 269–270.
- [5] Brett Barwick, David J Flannigan, and Ahmed H Zewail. “Photon-induced near-field electron microscopy”. In: *Nature* 462.7275 (2009), pp. 902–906.
- [6] David J Flannigan, Brett Barwick, and Ahmed H Zewail. “Biological imaging with 4D ultrafast electron microscopy”. In: *Proceedings of the National Academy of Sciences of the United States of America* 107.22 (2010), pp. 9933–9937.
- [7] Ayca Yurtsever and Ahmed H Zewail. “Direct visualization of near-fields in nanoplasmonics and nanophotonics”. In: *Nano letters* 12.6 (2012), pp. 3334–3338.
- [8] Ayca Yurtsever, J Spencer Baskin, and Ahmed H Zewail. “Entangled nanoparticles: discovery by visualization in 4D electron microscopy”. In: *Nano letters* 12.9 (2012), pp. 5027–5032.
- [9] Sang Tae Park, Milo Lin, and Ahmed H Zewail. “Photon-induced near-field electron microscopy (PINEM): theoretical and experimental”. In: *New journal of physics* 12.12 (2010), p. 123028.
- [10] P L Kapitza and P A M Dirac. “The reflection of electrons from standing light waves”. In: *Mathematical Proceedings of the Cambridge Philosophical Society* 29.02 (1933), pp. 297–300.
- [11] D L Freimund, K Aflatoon, and H Batelaan. “Observation of the Kapitza-Dirac effect”. In: *Nature* 413.6852 (2001), pp. 142–143.
- [12] M. Dressel and G. Grüner. *Electrodynamics of Solids: Optical Properties of Electrons in Matter*. Cambridge: Cambridge University Press, 2002, p. 474.

Chapter 3. Photo-induced near-field electron microscopy

- [13] William L. Barnes, Alain Dereux, and Thomas W. Ebbesen. “Surface plasmon subwavelength optics”. In: *Nature* 424 (2003), pp. 824–830. DOI: 10.1038/nature01937.
- [14] Stefan A. Maier and Harry A. Atwater. “Plasmonics: Localization and guiding of electromagnetic energy in metal/dielectric structures”. In: *J. Appl. Phys.* 98 (2005), p. 011101. DOI: 10.1063/1.1951057.
- [15] Ekmel Ozbay. “Plasmonics: Merging Photonics and Electronics at Nanoscale Dimensions”. In: *Science* 311 (2006), pp. 189–193. DOI: 10.1126/science.1114849.
- [16] David Rossouw and Gianluigi A. Botton. “Plasmonic Response of Bent Silver Nanowires for Nanophotonic Subwavelength Waveguiding”. In: *Phys. Rev. Lett.* 110 (6 2013), p. 066801. DOI: 10.1103/PhysRevLett.110.066801.
- [17] C. Clavero et al. “Magnetic field modulation of intense surface plasmon polaritons”. In: *Opt. Express* 18.8 (2010), pp. 7743–7752. DOI: 10.1364/OE.18.007743.
- [18] Bing Wang et al. “Strong Coupling of Surface Plasmon Polaritons in Monolayer Graphene Sheet Arrays”. In: *Phys. Rev. Lett.* 109 (7 2012), p. 073901. DOI: 10.1103/PhysRevLett.109.073901.
- [19] Johan Christensen et al. “Graphene Plasmon Waveguiding and Hybridization in Individual and Paired Nanoribbons”. In: *ACS Nano* 6.1 (2012), pp. 431–440. DOI: 10.1021/nn2037626.
- [20] Jianing Chen et al. “Strong Plasmon Reflection at Nanometer-Size Gaps in Monolayer Graphene on SiC”. In: *Nano Lett.* 13.12 (2013), pp. 6210–6215. DOI: 10.1021/nl403622t.
- [21] J. A. Dionne and H. A. Atwater. “Plasmonics: Metal-worthy methods and materials in nanophotonics”. In: *MRS Bull.* 37 (08 2012), pp. 717–724. DOI: 10.1557/mrs.2012.171.
- [22] V. J. Sorger et al. “Toward integrated plasmonic circuits”. In: *MRS Bull.* 37 (08 2012), pp. 728–738. DOI: 10.1557/mrs.2012.170.

-
- [23] Anatoly V. Zayats, Igor I. Smolyaninov, and Alexei A. Maradudin. “Nano-optics of surface plasmon polaritons”. In: *Phys. Rep.* 408.34 (2005), pp. 131–314. ISSN: 0370-1573. DOI: 10.1016/j.physrep.2004.11.001.
- [24] Vladimir D. Miljković et al. “Simulating light scattering from supported plasmonic nanowires”. In: *Opt. Express* 20.9 (2012), pp. 10816–10826. DOI: 10.1364/OE.20.010816.
- [25] Jens Dorfmueller et al. “Fabry-Pérot Resonances in One-Dimensional Plasmonic Nanostructures”. In: *Nano Lett.* 9.6 (2009), pp. 2372–2377. DOI: 10.1021/nl900900r.
- [26] A. Yurtsever, R. M. van der Veen, and A.H. Zewail. “Subparticle Ultrafast Spectrum Imaging in 4D Electron Microscopy”. In: *Science* 335 (6064 2012), pp. 59–64. DOI: 10.1126/science.1213504.
- [27] A. Yurtsever and A.H. Zewail. “Direct Visualization of Near-Fields in Nanoplasmonics and Nanophotonics”. In: *Nano Lett.* 12 (2012), pp. 3334–3338. DOI: 10.1021/nl301643k.
- [28] Jaysen Nelayah et al. “Mapping surface plasmons on a single metallic nanoparticle”. In: *Nat. Phys.* 3.5 (2007), pp. 348–353. DOI: 10.1038/nphys575.
- [29] D. Rossouw et al. “Multipolar Plasmonic Resonances in Silver Nanowire Antennas Imaged with a Subnanometer Electron Probe”. In: *Nano Lett.* 11.4 (2011), pp. 1499–1504. DOI: 10.1021/nl200634w.
- [30] Brett Barwick, David J. Flannigan, and Ahmed H. Zewail. “Photon-induced near-field electron microscopy”. In: *Nature* 462 (7275 2009), pp. 902–906. DOI: 10.1038/nature08662.
- [31] Sang Tae Park and Ahmed H. Zewail. “Photon-induced near-field electron microscopy: Mathematical formulation of the relation between the experimental observables and the optically driven charge density of nanoparticles”. In: *Phys. Rev. A* 89 (1 2014), p. 013851. DOI: 10.1103/PhysRevA.89.013851.

Chapter 3. Photo-induced near-field electron microscopy

- [32] Alexander Gubbens et al. “The GIF Quantum, a next generation post-column imaging energy filter”. In: *Ultramicroscopy* 110.8 (2010), pp. 962–970. ISSN: 0304-3991. DOI: 10.1016/j.ultramicro.2010.01.009.
- [33] L Piazza et al. “Simultaneous observation of the quantization and the interference pattern of a plasmonic near-field”. In: *Nature communications* 6 (2015).
- [34] Ezequiel R. Encina and Eduardo A. Coronado. “Plasmonic Nanoantennas: Angular Scattering Properties of Multipole Resonances in Noble Metal Nanorods”. In: *The Journal of Physical Chemistry C* 112.26 (2008), pp. 9586–9594. DOI: 10.1021/jp7120142.
- [35] Jens Dorfmueller et al. “Plasmonic Nanowire Antennas: Experiment, Simulation, and Theory”. In: *Nano Letters* 10.9 (2010), pp. 3596–3603. DOI: 10.1021/nl101921y.
- [36] Sean M. Collins et al. “Excitation dependent Fano-like interference effects in plasmonic silver nanorods”. In: *Phys. Rev. B* 90 (15 2014), p. 155419. DOI: 10.1103/PhysRevB.90.155419.
- [37] R. Esteban et al. “Direct Near-Field Optical Imaging of Higher Order Plasmonic Resonances”. In: *Nano Letters* 8.10 (2008), pp. 3155–3159.
- [38] A. H. Zewail and J. M. Thomas. *4D Electron Microscopy: Imaging in Space and Time*. London: Imperial College Press, 2009, p. 360.
- [39] L. Piazza et al. “Design and implementation of a fs-resolved transmission electron microscope based on thermionic gun technology”. In: *Chem. Phys.* 423.8 (2013), pp. 79–84. DOI: 10.1016/j.chemphys.2013.06.026.
- [40] L. Piazza et al. “Ultrafast structural and electronic dynamics of the metallic phase in a layered manganite”. In: *Structural Dynamics* 1.1 (2014), p. 014501. DOI: 10.1063/1.4835116.
- [41] A. Howie. “Photon-Assisted Electron Energy Loss Spectroscopy and Ultrafast Imaging”. In: *Microsc. Microanal.* 15.4 (2009), pp. 314–322. DOI: 10.1017/S1431927609090254.

-
- [42] F. J. García de Abajo and M. Kociak. “Electron energy-gain spectroscopy”. In: *New J. Phys.* 10.7 (2008), p. 073035. DOI: 10.1088/1367-2630/10/7/073035.
- [43] F. J. García de Abajo and M. Kociak. “Probing the Photonic Local Density of States with Electron Energy Loss Spectroscopy”. In: *Phys. Rev. Lett.* 100 (10 2008), p. 106804. DOI: 10.1103/PhysRevLett.100.106804.
- [44] Sang Tae Park, Milo Lin, and Ahmed H. Zewail. “Photon-induced near-field electron microscopy (PINEM): theoretical and experimental”. In: *New J. Phys.* 12.12 (2010), p. 123028. DOI: 10.1088/1367-2630/12/12/123028.
- [45] A. Asenjo-García and F. J. García de Abajo. “Plasmon electron energy-gain spectroscopy”. In: *New J. Phys.* 15.10 (2013), p. 103021. DOI: 10.1088/1367-2630/15/10/103021.
- [46] J.C. Ashley and L.C. Emerson. “Dispersion relations for non-radiative surface plasmons on cylinders”. In: *Surface Science* 41.2 (1974), pp. 615–618. ISSN: 0039-6028. DOI: [http://dx.doi.org/10.1016/0039-6028\(74\)90080-6](http://dx.doi.org/10.1016/0039-6028(74)90080-6).
- [47] Rashid Zia and Mark L. Brongersma. “Surface plasmon polariton analogue to Young’s double-slit experiment”. In: *Nat. Nanotechnol.* 2 (2007), pp. 426–429. DOI: 10.1038/nnano.2007.185.
- [48] Roman Kolesov et al. “Wave-particle duality of single surface plasmon polaritons”. In: *Nat. Phys.* 5.7 (2009), pp. 470–474. DOI: 10.1038/NPHYS1278.
- [49] James S. Fakonas et al. “Two-plasmon quantum interference”. In: *Nat. Photon.* 8.4 (2014), pp. 317–320. DOI: 10.1038/nphoton.2014.40.
- [50] Roman Walther et al. “Interslit Coupling via Ultrafast Dynamics across Gold-Film Hole Arrays”. In: *J. Phys. Chem. C* 118.20 (2014), pp. 11043–11049. DOI: 10.1021/jp503613t.

Chapter 3. Photo-induced near-field electron microscopy

- [51] Sacha Kocsis et al. “Observing the average trajectories of single photons in a two-slit interferometer”. In: *Science* 332.6034 (2011), pp. 1170–1173. DOI: 10.1126/science.1202218.
- [52] MD Davidović and AS Sanz. “How does light move? Determining the flow of light without destroying interference”. In: *Europhysics News* 44.6 (2013), pp. 33–36. DOI: 10.1051/epn/2013604.
- [53] Adrian Cho. “Breakthrough lost in coin toss?” In: *Science* 346 (6205 2014), pp. 22–23.
- [54] E. Altewischer, M. P. van Exter, and J. P. Woerdman. “Plasmon-assisted transmission of entangled photons”. In: *Nature* 418 (2002), pp. 304–306. DOI: 10.1038/nature00869.
- [55] G Di Martino et al. “Observation of quantum interference in the plasmonic Hong-Ou-Mandel effect”. In: *Physical Review Applied* 1.3 (2014), p. 034004.
- [56] Kylee E. Korte, Sara E. Skrabalak, and Younan Xia. “Rapid synthesis of silver nanowires through a CuCl- or CuCl₂-mediated polyol process”. In: *J. Mater. Chem.* 18 (4 2008), pp. 437–441. DOI: 10.1039/B714072J.
- [57] Edward D. Palik, ed. *Handbook of Optical Constants of Solids*. London: Academic Press Limited, 1998, p. 999.

Chapter 4

Perspectives in ultrafast electron microscopy

In the previous chapters we described some applications of ultrafast electron microscopy. These include ultrafast imaging, ultrafast diffraction, ultrafast spectroscopy and the possibility of combining them as in ultrafast energy-space mapping and energy-filtered ultrafast imaging. The landscape of systems that can be investigated in a fs-TEM is still vastly unexplored but in a field in such rapid evolution is nonetheless worth looking forward in to the future and imagine what are the possible technological evolutions for this technique.

The electron microscope components

Currently the main approach to ultrafast electron microscopy consist in the modification of a existing commercial TEM sobtituting the traditional

Parts of this chapter are taken from *A proposal for fs-electron microscopy experiments on high-energy excitations in solids*, L. Piazza *et al*, Micron, 63 4046, 2014, an extended introduction and more considerations are added.

Chapter 4. Perspectives in ultrafast electron microscopy

thermal-emission or field-emission process with a photo-emission mechanism. The hardware modifications necessary for propagating an ultrafast laser beam into the column depend on the particular brand and model of the microscope but it is common practice to generally limit the modifications as much as possible because of the advanced engineerization and the highly optimized proprietary solutions developed by individual companies in decades of work.

This is definitely a successful approach but it's hardly the optimal solution, preventing the optimization of the performances of the ultrafast microscopes over a certain boundary.

In traditional microscopy the electron beam brightness is generally the parameter chosen for describing its overall quality and a high value is necessary for high spatial and energy resolution. In the case of pulsed electron sources this concept should be extended and the phase space that describes the beam has two extra dimensions, adding to the transverse size and spread of the beam also the longitudinal components, directly connected to the final time resolution of the instrument. In [1] a new quantity has been proposed, the *coherent fluence*, described as:

$$N_C = \frac{\pi^2 \lambda^2 B \Delta t}{e}$$

where $\lambda = \frac{h}{\beta \gamma m c}$ is the relativistic electron wavelength, Δt is the pulse duration and B is the conventional brightness defined as

$$B = \frac{N e}{(\pi r^2)(\pi \alpha^2) \Delta t}$$

where N is number of electrons, r is the radius of the beam and α is the convergence angle.

The coherent fluence of an electron pulse (i.e. the relative volume in the phase space) is a constant of motion in an ideal system and can be used to describe the effect of electromagnetic lenses and their aberrations as well as the effect of *temporal lenses* like radio-frequency cavities, the effect of

apertures and energy filters.

This parameter is essential in case of single-shot operation because it determines the highest spatial resolution available in function of the amount of charge in every electron pulse [1]. In the case of few-electron operation, when the space-charge effects are reduced, it's still important to understand how a particular configuration of lenses alters the phase-front in time and space, giving the experimenter the ability to tailor the electron probe to the needs of a particular measurement. The ability to tradeoff coherence of the beam with signal-to-noise ratio at the price of a longer acquisition time, for example allows the acquisition of data when incoherent imaging based on the absorption of electrons by the sample is not feasible. The ability of using a spacially coherent beam is fundamental to be able to observe critical details in diffraction patterns, as the extraspots due to orbital ordering visible in image 2.1 of chapter 2, or for the case of Lorentz microscopy.

There are two possible ways to increase the spatial coherence, namely to reduce the emittance at the source decreasing the dimension of the source of emission or by blocking part of the beam with apertures in the column of the microscope. For operations in the femtosecond timescale it is not desirable to photo-emit many electrons with the idea of blocking the majority of them with apertures, since the space-charge and the Boersch effects at the source will irreversibly degrade the temporal and spatial properties of the electron bunch. For these reasons a lot of work has been done in this field and several configurations for photoemission from sharp tips [2, 3, 4, 5, 6] and some innovative schemes involving ultracold electron sources [7, 8] have been proposed. The latter, in particular, have not yet been interfaced to electron microscopes but they showed promising performances in combination with ultrafast diffraction setups, making a big step in the direction of obtaining an electron pulse whose density in the phase space is limited only by the physical constraints of the Pauli exclusion principle.

The creation of a well defined electron pulse in the gun is only the first step since it should be efficiently delivered to the sample, allowing the user of the

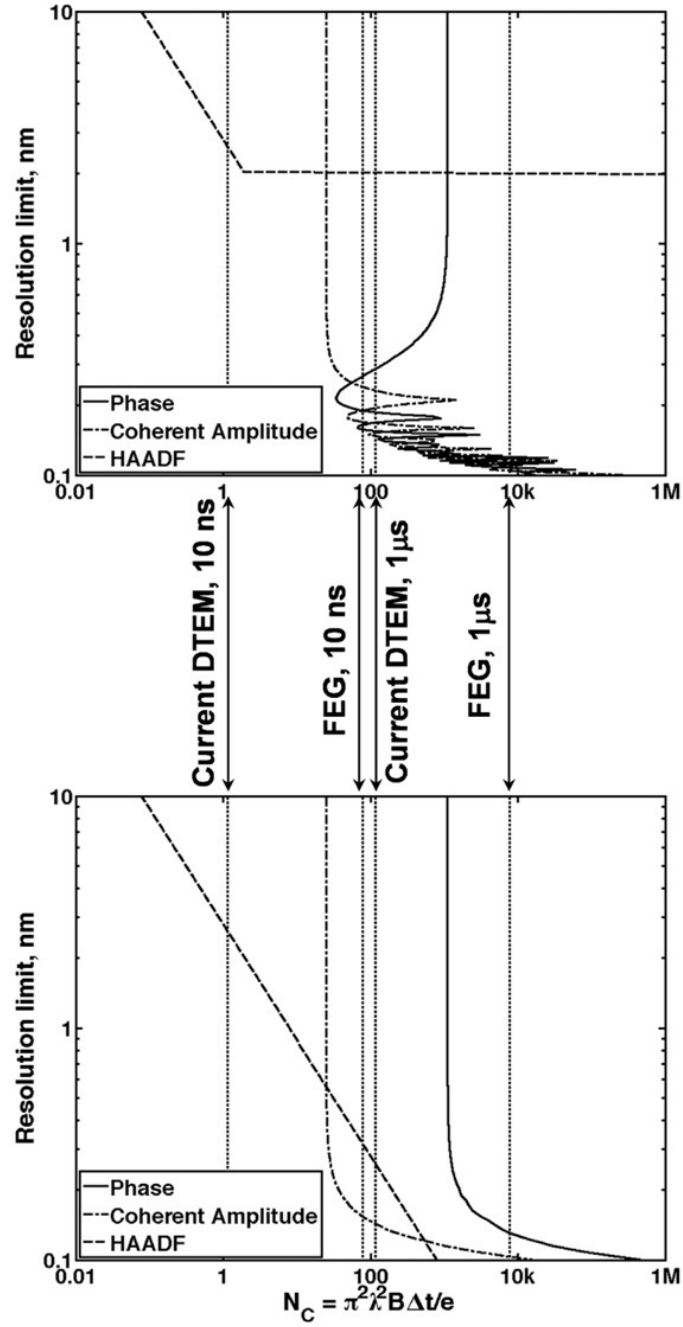


Figure 4.1: (Top) Cs-limited and (bottom) Cs-corrected resolution limits as a function of the scaled product of brightness and pulse duration (or coherent fluence) for single-shot imaging. Vertical dashed lines are four different N_C values. These curves are for ideal samples with 100% contrast in a 200 keV microscope; the curves for real samples will be shifted somewhat to the right. Adapted from [1].

Proposal for a high-energy excitation in solids.

microscope to choose between the variety of different operational modes. In comparison with the optical counterpart the quality of the electron lenses is very poor. In the last decades a big effort has been made by the microscopy community and particular electron-optics schemes has been developed [9], able to correct the first orders of the spherical and chromatic aberrations introduced by the solenoids, reaching a spatial resolution below the angstrom and an energy resolution on the order of 0.01 eV [10] . These complicated designs will eventually be very useful in the framework of ultrafast microscopy, increasing the overall quality of the electron beams also for pulsed operations.

Proposal for a high-energy excitation in solids.

The use of ultra-coherent pulsed electron sources and the complete control of the beam used to probe the sample is only one side of the medal, and in the framework of the evolution of ultrafast electron microscopy there is the possibility of rethinking also the way we perturb the sample and clock our time-resolved experiment.

Introduction

The development of fs lasers opened the possibility to investigate the temporal evolution of photoexcitation in solids and molecules. The research field of transient states in molecules has been referred to as femtochemistry [11], and ultrafast spectroscopy has been successfully applied to several domains including solid state and biological physics [12]. Despite the huge potential and the evident success of these techniques, some limitations to their applicability persisted over the years, confining them to specific situations. In a nutshell, while it is often possible to measure the value of a given physical quantity by a large choice of static techniques, the out-of-equilibrium nature of time-resolved techniques makes their output more specific and its theoret-

Chapter 4. Perspectives in ultrafast electron microscopy

ical modeling more challenging and less direct. This is due to the need of referencing in time the observable, which is typically done via photoexcitation, and therefore is an intimate characteristic of such experiments. There has to be a well-defined excitation in time to be able to probe the temporal evolution of a system. Naturally, when the ground state properties are already elusive, the description of its excitations and its out-of-equilibrium state is a further complication. In molecules, this issue has proven less severe than in solids because electronic excitations are more univocally described and have smaller coupling with the other degrees of freedom, allowing for a better description of the pump excitation process. On the contrary, if one considers strongly correlated systems, many-body effects induce a broad spectrum of complex electronic states extending all the way to the visible-light region [13, 14], often making the description of the photoexcitation challenging.

Recent advances in ultrafast technology provided a large variety of observables. Depending on the phenomenon investigated, nowadays time resolution between *ms* and *as* can be achieved with X-rays and electrons, giving direct information on both the structure and the chemistry of materials via either diffraction or spectroscopy [15]. Free-electron laser facilities guarantee a unique X-ray flux in a highly transversally coherent beam, capable of few fs time resolution [16, 17, 18], while state of the art electron-beamlines and transmission electron microscopes offer higher sensitivity and versatility at the cost of coherence and to a less extent time resolution [19, 20, 21, 22, 23, 24, 25, 26]. Despite this, transverse coherence can be increased using larger beamsizes.

In short, current ultrafast techniques allow the direct observation of the out-of-equilibrium properties of materials via both structural probes and broadband spectroscopy. The need for photoexcitation and consequently the observation of a perturbed system is a key aspect, especially for the study of complex materials, where a great challenge lies in the understanding and description of the lowest energy excitations of the ground state, which would seem logic to observe by the least perturbing possible probes. This said, a

great potential hides in time-resolved experiments: if the excitation is carefully prepared [27, 28], it can decay on a well-defined final state, and the real-time observation of the latter can have major advantages: i) not only the amplitude, but also the phase of the wave-function describing such a state can be obtained, ii) the temporal evolution of different many-body objects, i.e. their consequentiality, can also be obtained and therefore the evolution of a system through a phase transition can be described in much more detail [29]. The following two examples can clarify this point:

- **Graphite:** the phonon spectrum of graphite has been known for almost a century. Despite this, only recently it was discovered that some of the vibrational modes couple to the electronic structure in a particular sequence, giving rise to photoinduced structural changes that can even turn graphite into diamond during a few fs, a process that takes ages under extreme conditions in nature [30, 31, 32, 21, 33, 34]. These results shed new light on the dynamics of the structure of graphite which could not be inferred by the knowledge of its equilibrium properties.
- **High temperature superconductors:** In recent ultrafast experiments on high-temperature superconductors [28], 1.5 eV photons were used to induce a direct transition between the ground state of the material and higher energy electronic states, ascribed to the excitation of charge stripes and the Cu-O charge transfer bands [35, 36], see schematics in Fig. 4.2 B. In a conventional static Raman experiment, as depicted in Fig. 4.2 A, one can excite the system with a continuous wave (CW) photon beam at 1.5 eV and analyze the Raman-shifted outgoing photons, obtaining the energy spectrum of the low-energy excitations, structural and electronic. In a pump-probe experiment, the final state after impulsive excitation at 1.5 eV is the same as in a static Raman experiment. Only this time, instead of analyzing the outgoing photon, one probes the system with weak non-perturbing fs pulses while the excited state still survives (few ps after excitation). As a result, an equivalent of the Raman spectrum is obtained in the time domain,

Fig. 1 C,D, via the Impulsive Stimulated Raman Scattering mechanism (ISRS). This scenario is confirmed by the agreement between the data (FFT) and conventional Raman experiments [37], in Fig. 4.2 E,F. These results provided the first observation of the coherent oscillation of the Cooper pair condensate in the time domain.

The aim of this work is to propose a new class of experiments that can exploit the ISRS mechanism to provide a selective population of the different excited states and at the same time combine the advantages of pulsed X-rays and electron beams for the investigation of solids. Particular emphasis is put in the discussion on the advantages of a chemically selective excitation, as achievable via X-rays. In what follows, the technical requirements and the feasibility of experiments based on an X-ray photoexcitation and an EM probe will be discussed. A quantitative discussion of what type of excitations and physics can be probed in solids by such a technique is proposed. These ideas borrow concepts from the community of ultrafast technology, electron microscopy and condensed matter physics, and provide an interdisciplinary challenge aimed at exploiting the most recent technologies made available worldwide.

The role of the excitation in time-resolved experiments.

As was briefly introduced above, a key ingredient of this discussion is the preparation of the excited state via the photoexciting pulse. In fact, not only are X-rays a unique tool for probing materials and molecules, they also provide the possibility to create chemically selective excitations. Typically, ultrashort laser pulses in the visible light region are used as a pump because of their easy availability. In this energy range, temperature jumps, charge transfers, and phase transitions can be triggered. However, at these energies, the strong orbital hybridization makes the chemical selectivity of the pump absent in many systems, and in some cases like strongly correlated solids, it is often very hard to decipher the effect of light excitation in the sample,

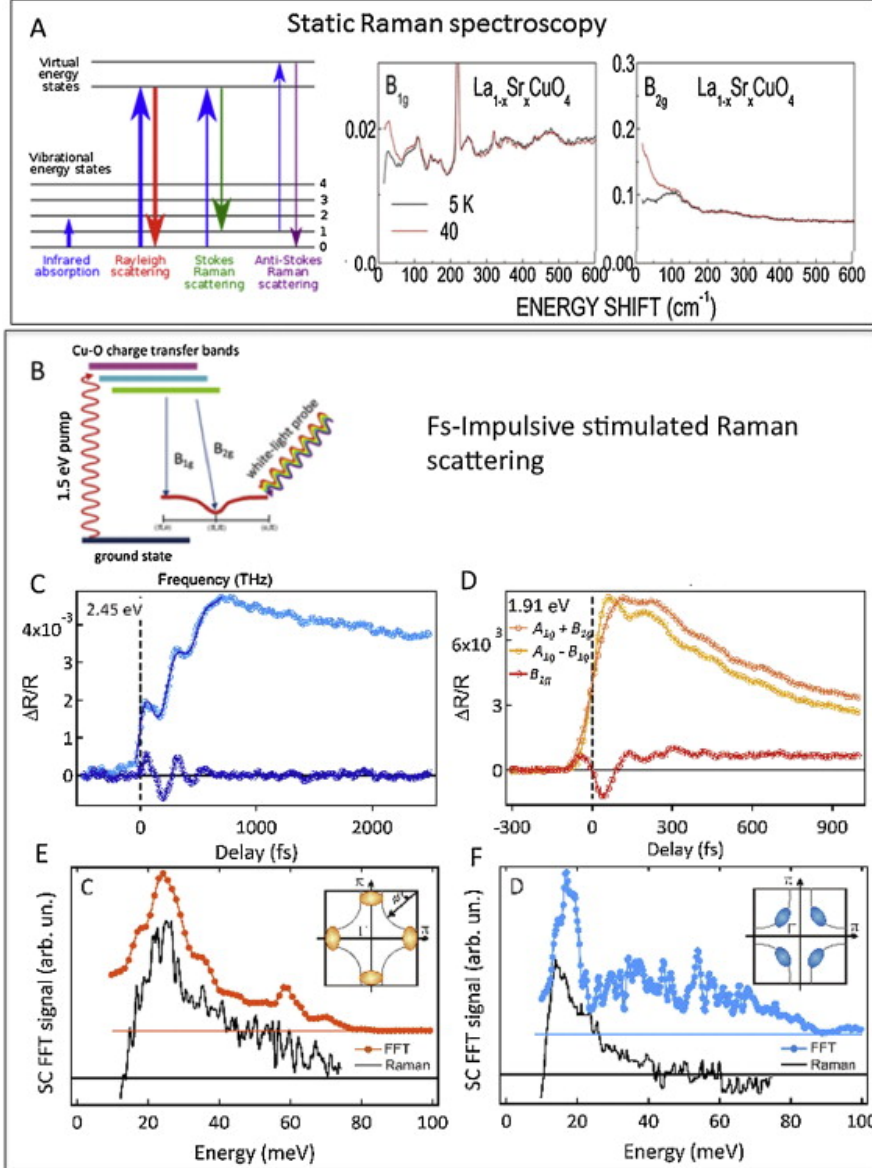


Figure 4.2: A schematics of a Raman experiment (left), and static Raman spectrum in a $\text{La}_{2-x}\text{Sr}_x\text{CuO}_4$ (LSCO) high temperature superconductor. B. Scheme of the Raman process involved in an ultrafast ISRS experiment. C, D temporal evolution of the optical susceptibility of LSCO in different Raman geometries, B_{1g} and B_{2g} respectively. E, F Fourier transform of the temporal traces and comparison with the static Raman spectra of the superconducting gap in LSCO. This figure is adapted from [28] and [37].

Chapter 4. Perspectives in ultrafast electron microscopy

since a thorough description of the static optical absorption can be lacking or be model dependent. Very novel and interesting experiments have been put forward where a more precise selectivity of the excitation has been obtained via the use of THz pump pulses [27]. In the low energy region of the infrared spectrum, light can excite selectively atomic motions, providing a way to distort "ad hoc" the structure of a system for probing its consequent dynamics. This approach takes advantage of the interaction between light and low-energy many-body bosonic excitations and allows a direct manipulation of collective modes in materials. However, because of the way THz pulses are generated and their intrinsic characteristics, sub-ps temporal resolution is often challenging. Another possibility to achieve selectivity, although local, in the excitation would be to use X-ray pulses tuned to specific core levels while monitoring the consequent dynamics with another photon or an electron pulse.

In the case of pump-probe experiments in high-temperature superconductors, it is clear that in certain circumstances one can regard a pump-probe optical experiment as a resonant Raman experiment. The main difference is that instead of detecting the outgoing photon and its polarization, to obtain the low-energy excitations spectrum, information is obtained directly in the time domain via an appropriate ultrafast probe. In the end, by Fourier transforming the time-domain probe signal, one ends up with a Raman spectrum. In addition, the time domain observation yields the phase of the probed state and its temporal evolution through phase transitions. In this context, as much as Resonant Inelastic X-ray Scattering (RIXS) provides additional information with respect to low-energy Raman experiments [38] thanks to chemical and orbital selectivity, an (X-ray pump)-(time resolved probe) experiment would take advantage of the same benefits. In RIXS, resonance with certain core-levels can greatly enhance the inelastic cross-section, i.e. the population of excited states; X-ray photons can also probe the dispersion of low-energy excitations and can even differentiate between different sites occupied by the same element, if they have distinguishable absorption features. In the energy range of the L-edge of transition metals, X-rays have

a penetration depth of few hundreds of nm, matching both the penetration depth of high energy electrons and infrared light. One of the main challenges of a RIXS experiment is the presence of a relatively broad elastic peak whose tail hides the lowest energy excitations (in the THz, meV regime). On the contrary, the technique is very effective for energy losses in the region of a fraction of an eV to a few eV. This behavior is complementary to the performance of time-resolved experiments, because in this case, the lowest energy (meV, THz) excitations translate into slower oscillations requiring few tens to few hundreds of fs time resolution. The high energy features like charge transfers instead are found in the eV region, requiring a temporal resolution within the single fs regime. This concept is depicted in Fig. 2, where we show the typical excitations observed via RIXS; the graph is adapted from [38], and a temporal scale was added to the top of the panel, making the correspondence between the energy of the electronic states and its consequent time-period. In one example, the low-lying orbital excitations (orbitons) which are speculated to hide from sight within the elastic peak of a conventional RIXS experiment may be visible in a time-resolved measurement as a hundreds of fs oscillation of the probed quantity. Moreover, looking at the example of the ultrafast response of LSCO, the THz Raman spectrum of a high-temperature superconductor was obtained through a time domain experiment, with no information on the dispersion of the observed features. Tuning the photoexcitation to an appropriate core-level and taking advantage of matrix elements and selection rules, one could perform an experiment that is sensitive also to the dispersion of the electronic states and, more importantly, will have a better chemical and orbital sensitivity. Chemical selectivity of X-rays has been also proposed to induce photodoping in materials through cascade decay processes of the electron hole pairs, or by directly promoting itinerant carriers in valence band orbitals [39]. This said, in any pump-probe experiment, a certain amount of unwanted excitations will be present. For example, ultrafast excitation of perovskites often results in strong coherent phonons being excited together with the electronic excitations (see the La vibration mode observed in Ref. [28] for example). However, the ability of an EM to combine diffraction, EELS, [40] and imag-

ing would give further ability to disentangle the different excitations during the probing.

Quantitative analysis of an X-ray pump-TEM probe experiment

The fs-TEM probe

Currently, fs-resolved TEMs operate in the regime of 1-10 electrons per pulse at repetition rates between 200 kHz and 2 MHz [41, 42]. Overall, the number of particles per second ranges from 10^5 to 10^7 , of which only 10 % are detected by the most common cameras. Since the temporal resolution is obtained by simple modification of commercial TEM columns, these machines preserve the versatility characteristics of TEMs and can operate in a variety of modes including imaging, diffraction and analytical microscopy. XFEL sources can on the other hand provide repetition rates between few Hz [43] and tens of kHz [44]. Therefore, to retain the same signal per second in the TEM probe, the electron pulses should contain between 10^3 and 10^4 particles each. To have such an amount of charge in a sub-ps pulse and yet retain the energy spread within few eV and the spatial coherence required for imaging and diffraction, a careful design of the TEM source and column is needed.

The spatial or transverse coherence length is given by $L_{\perp} \equiv \lambda/\Delta\theta$, with λ being the De Broglie wavelength and $\Delta\theta$ the uncorrelated angular spread. In order not to waste any electrons, the beam diameter D should be matched to the sample size. Then the proper figure of merit for spatial coherence (transverse beam quality) is the *relative* coherence length L_{\perp}/D , a conserved quantity which is inversely proportional to the normalized emittance ε_n : $L_{\perp}/D \approx \lambda_C/(4\varepsilon_n)$, with $\lambda_C = h/mc = 2.43$ pm the Compton wavelength. For amplitude contrast imaging at 100 keV with near-atomic resolution a relative coherence length around 10^{-3} is ideal, i.e. $\varepsilon_n \approx 0.5$ nm · rad. Similar numbers are required for the most demanding diffraction measurements, i.e.

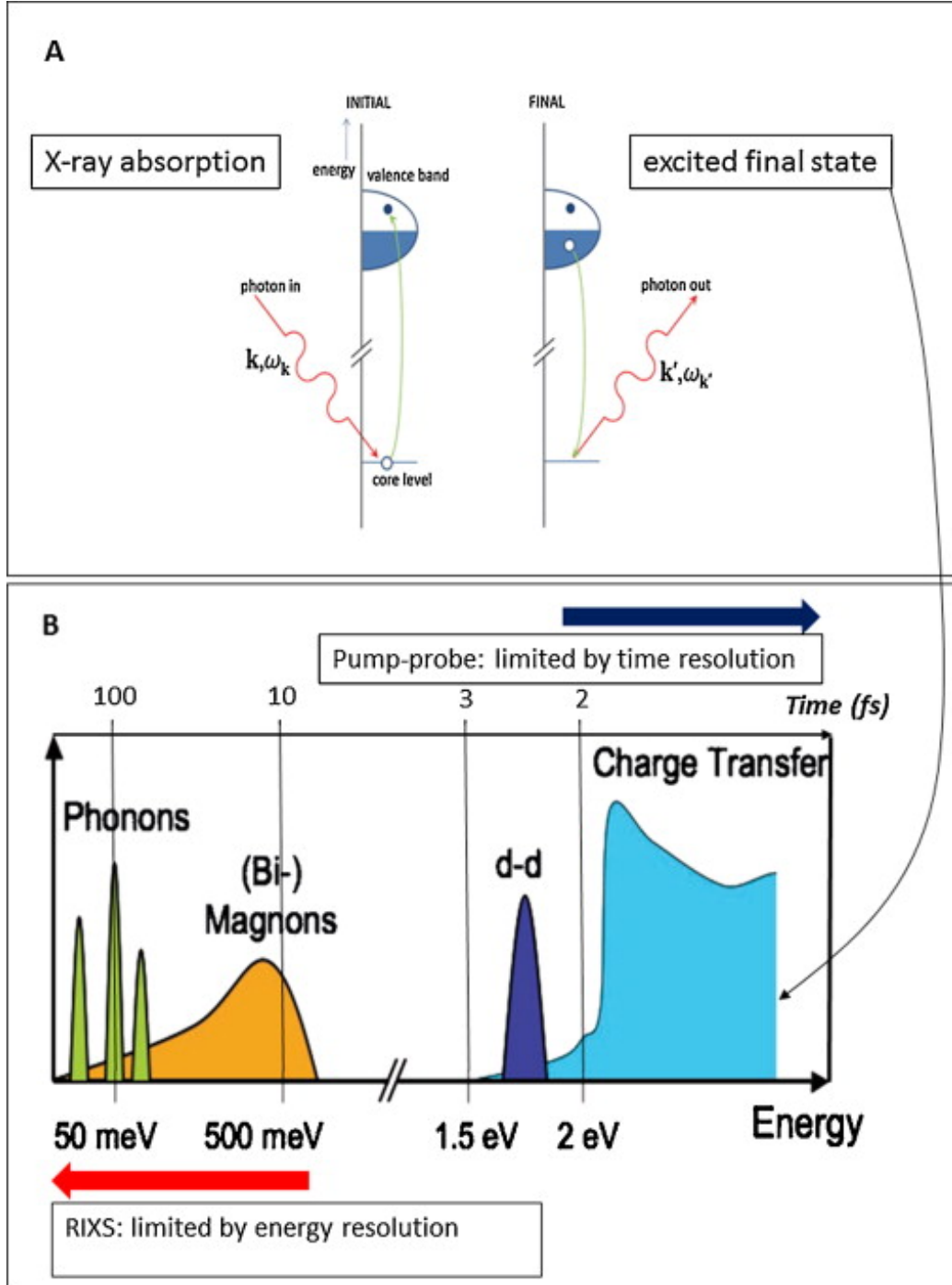


Figure 4.3: Top: X-ray absorption process and generation of a final excited state. Bottom: energy and temporal scale of final excited states, figure adapted from [38].

diffraction of micron-sized protein crystals or nano-diffraction of solid state samples. However, by properly correcting aberrations, imaging with sub-nm resolution is possible also with a completely incoherent source [45]. A normalized emittance of 0.5 nm·rad can in principle be achieved by photoemission with a micron diameter laser spot on the photocathode, as was recently demonstrated by Kirchner *et al.* using pulses containing only one electron [46]. To extract 10^3 electrons in a single pulse from a micron sized spot a field strength of a few tens of MV/m is required, which can be done quite straightforwardly, using an RF photogun. Alternatively, one could use the recently developed ultracold source, based on photoionization of a laser-cooled and trapped atomic gas [47, 48], which has already been demonstrated to deliver the required combination of charge and emittance in a picosecond pulse. Since the ultracold source allows a much larger source size for the same normalized emittance, smaller extraction fields are required and space charge problems are much less of an issue. Due to Coulomb forces the bunch will expand to many picosecond lengths during its passage through the TEM. Compressing the bunch back to sub-ps lengths will inevitably lead to an increase of the energy spread, as the product of uncorrelated energy spread ΔU and bunch length Δt – the longitudinal normalized emittance $\varepsilon_{\parallel} \approx \Delta U \Delta t / mc$ – is a conserved quantity in absence of nonlinear forces. The required longitudinal beam quality is $\Delta U \Delta t \approx 1 \text{ ps} \cdot \text{eV}$, corresponding by changing units to $\varepsilon_{\parallel} \simeq 0.5 \text{ nm} \cdot \text{rad}$, and, interestingly, very similar to the transverse beam quality requirement: the *relative* coherence should be approximately equal in all directions. Producing bunches with the required initial longitudinal emittance is not a problem using either regular photocathodes or the ultracold source. The challenge is to apply a compression technique which conserves transverse and longitudinal emittance while the originally dilute, many-ps bunch is converted into a dense, space-charge-dominated, sub-ps bunch.

In the past few years several bunch compression methods have been devised [49, 50, 23, 51]. Grzelakowski and Tromp recently proposed a particularly elegant method [52], which employs the mirror symmetry of a spherical electrostatic capacitor. As it is a passive, static device, no additional synchro-

nization is required, which is an important advantage. However, this method still needs to be proven experimentally. Here we consider the possibility of importing in time-resolved TEMs the same technique which has allowed a significant improvement in temporal resolution in ultrafast electron diffraction systems, that is longitudinal (temporal) focusing using a radiofrequency cavity [19, 53, 54]. It has been shown that the resonant electromagnetic fields in a radiofrequency cavity can be used to impart a velocity-chirp to the electron beam, thus reversing the longitudinal space charge expansion which otherwise limits the pulse length for larger number of particles. After passage through the cavity, the particles in the back of the pulse have higher velocity and can overtake the front of the pulse so that at the sample the beam reaches a longitudinal focus [49, 50, 23].

In the TEM, designing and tuning the radiofrequency cavity to achieve maximum compression is less straightforward than in simpler UED machines due to multiple transverse crossovers along the column.

To estimate the achievable beam parameters upon RF compression in a TEM, we simulated using the General Particle Tracer code the condenser stage of a TEM with a modified gun to allow photocathode illumination and dynamic time-resolved mode. The TEM column and the position of the lenses for the simulation were extracted from [55]. The results of the simulation without any radiofrequency cavity are in good agreement with the measurements of pulse length and energy spread carried out using the PINEM effect [41]. In Fig. 3, the experimental pulses duration (blue symbols) and energy spread (black symbols) of an uncompressed beam are shown as a function of the charge in the bunches together with the results of GPT simulations (blue and black lines).

Using this model, we can then investigate the effect of inserting a radiofrequency cavity for beam compression in the column. A radio-frequency TM_{010} mode cavity resonant at 3 GHz was inserted at $z=60$ cm from the virtual cathode source point to compress the bunch. Preliminary estimates indicate that it is possible to obtain 10^3 particles in < 200 fs at the sample with com-

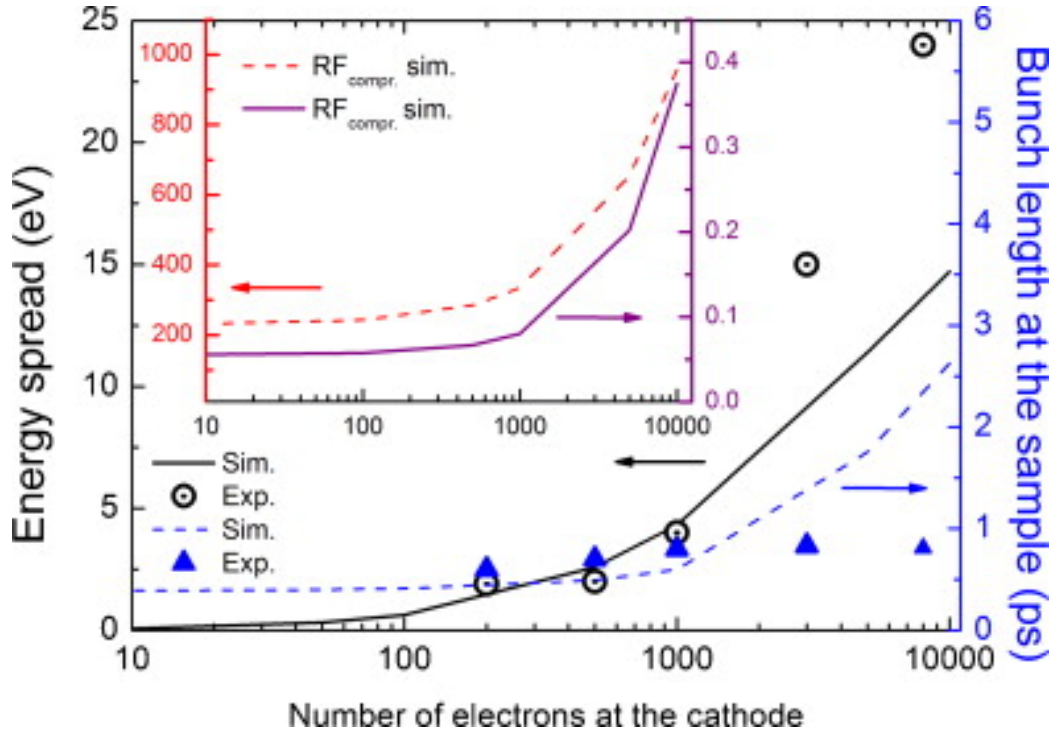


Figure 4.4: Electron pulses duration and energy spread as a function of the beam charge. Inset: bunches duration and energy spread for an RF compressed beam. Image adapted from [56].

parable transverse beam quality with current designs. Since the mechanism for compression is to accelerate the particles in the back of the beam and decelerate the ones in the front, a larger beam energy spread is induced by the cavity. This does not present a major problem for diffraction and imaging, although the latter can be affected by chromatic aberrations, but it certainly hinders the possibility of high resolution spectroscopy. With a combination of multiple (not just one) longitudinal lenses then one could design a "condenser" stage for the time-energy phase space and control both the beam bunch length and energy spread at the sample. We leave this possibility as a topic for further more detailed study. In the inset of Fig. 3, the pulses duration and energy spread are displayed for an RF compressed beam.

It is important to notice at this point that the imaging performances of such an instrument will be different from those of a conventional TEM. How-

ever, when combining space and time resolution, no technique exists which is capable of reaching fs and nm resolution in time and direct space simultaneously. There is a great deal of phenomena that could be investigated successfully with a spatial resolution of tens to hundreds of nm and fs temporal resolution. To name a few, direct imaging of magnetic domains and their motion could be performed. Also, the dynamics of the vortex lattice in superconductors, or the temporal evolution of charge domains and phase separation are topics for which the ability to combine time and direct-space imaging will be a breakthrough. In a TEM, bright field and dark field images already give a contrast to morphological features of a specimen, while in out-of-focus Lorentz microscopy enhanced contrast to magnetic domains and charge patterns can be obtained [57].

The XFEL pump

The impulsive stimulated Raman scattering effect has been exploited for the study of coherent structural and electronic excitations via the observation of changes in the optical constants [58, 28]. For visible-light pumps, absorbed fluences in the range of $100 \mu\text{J}/\text{cm}^2$ per pulse have been used for photoexcitation. In typical pump-probe experiments, such an excitation is found to produce a background of linearly excited particle-hole pairs on top of the desired Raman excitations. In the example from Ref [28], it was possible to obtain about 10^{-3} to 10^{-2} ISRS excited states per site, yielding a signal in the order of 10^{-3} in variation of the dielectric function. In recent fs-resolved electron scattering experiments signals of similar strength have been detected successfully.

To estimate the yield of the Raman excited particles per site for excitation with X-rays one needs to estimate how many photons are absorbed by the material at a given energy. For the example we used, LSCO, it is well known that the Cu L-edge (930 eV) provides a very good yield for resonant Raman experiments [38]. At this energy, the absorption of a 200 nm sample, ideal

Chapter 4. Perspectives in ultrafast electron microscopy

thickness for being transparent to 300 keV electrons, accounts for about the 70 % of the impinging beam [59]. For an XFEL pump, each pulse can be expected to contain around 10^{12} photons. If one considers these photons to be absorbed in a volume of $\pi \times 50 \times 50 \times 0.1 \mu\text{m}^3$, the number of photons absorbed per site can be as much as 10^{-1} . The fluorescence yield at the Cu L-edge is in the order of 10^{-2} , of which up to 20 % can be due to inelastic events [38, 60], leaving a net number of ISRS excitation per site in the order of 10^{-3} , in the range of the optical ISRS experiments. Such an excitation yield per pulse is expected to provoke changes in the spectroscopic and diffraction properties of the material in the order of the fraction of a percent, while we cannot make an estimate of the effects of such changes observable in imaging. The visibility of such a change depends in turn on the signal to noise ratio and integration time of the experimental set-up. In the optical experiments for example, these phenomena were resolved by summing as many as 1.6 million pulses at a repetition rate of 1 KHz for a total acquisition time of 20 minutes, having a shot to shot noise in the experimental probe at the percent level.

Based on these estimates, we argue that for a large and general class of pump-probe experiments aimed at investigating the properties of coherent modes, the combination XFEL-pump and electron-probe offers a competitive alternative to more standard optical pump-probe schemes.

The synchronization

Practically, X-ray pump/fs-TEM experiments would require the synchronization of a laser source to the X-ray source. The fs laser will serve as a drive for the TEM photocathode, allowing to generate electron bunches with different duration and charge via the photoemission process. Synchronization between a laser and an X-FEL source has been recently discussed, proposing different approaches that can lead to a stabilization of the relative delay between the sources in the order of the pulse duration itself [61, 62]. An

Proposal for a high-energy excitation in solids.

alternative way to solve the problem is offered by time-stamping each image, enabling data sorting in postprocessing the images. This has been successfully demonstrated at XFEL achieving sub-10 fs temporal resolution [63]. For ultrafast electron pulses time-stamping was pioneered for MeV electron diffraction setup using electro-optic sampling methods[64]. New techniques have recently been demonstrated to work also for non-relativistic electrons [65]. In addition, a RF-fs laser synchronization technique has been developed which allows the measurement of the phase of the amplified RF field in the cavity with respect to the fs laser pulse for each individual shot with 30 fs resolution [66]. Since the main cause of arrival time jitter is due to RF phase jitter of the compression cavity, the latter technique should allow accurate time-sorting of the individual images.

In the case discussed here, an extra complication arises from the need to use an RF electron gun in the TEM. Such a device requires the synchronization between an RF cavity and the laser source, which can be done also with high accuracy using the technique described in [66]. In total, the jitter of such a time-resolved experiment will be mainly affected by two components: the laser-XFEL jittering, and the laser-TEM jittering. Each of these two components has different sources: - the XFEL-laser jitter originates from the laser rep-rates instabilities, mainly due to temperature drifts in the cavity, and the intrinsic noise of the XFEL source. - The laser-TEM jitter is mainly caused by the synchronization between the RF cavity, temperature drifts plus the noise of the RF source, and the laser itself, temperature drift of the optical cavity. These sources of non-ideality can be considered to a first approximation as independent, and therefore, summed quadratically. Based on current technology available, the overall jittering of such a set-up will be expected to be about 50 % higher than the laser pulse duration.

Conclusions

In this chapter, we discussed the feasibility of combining ultrashort X-ray sources, currently under development, with an ultrafast TEM. The goal of these experiments is to provide a uniquely broad-band view of materials and nanostructures and their transformations happening in the fs time-scale. Such an approach would benefit from both most recent achievements in ultrafast science, i.e. time-resolved TEM and XFEL technology, and promises to deliver combined structural, spectroscopic and morphological information on an extraordinarily wide class of systems, ranging from bio-molecules to strongly correlated solids.

References

- [1] B W Reed et al. “The evolution of ultrafast electron microscope instrumentation”. In: *Microscopy and microanalysis: the official journal of Microscopy Society of America, Microbeam Analysis Society, Microscopical Society of Canada* 15.4 (2009), pp. 272–281.
- [2] B Barwick et al. “Laser-induced ultrafast electron emission from a field emission tip”. In: *New journal of physics* 9.5 (2007), p. 142.
- [3] M Boussoukaya et al. “High quantum yield from photofield emitters”. In: *Nuclear instruments & methods in physics research. Section A, Accelerators, spectrometers, detectors and associated equipment* 279.3 (1989), pp. 405–409.
- [4] C Hernandez Garcia and C A Brau. “Pulsed photoelectric field emission from needle cathodes”. In: *Nuclear instruments & methods in physics research. Section A, Accelerators, spectrometers, detectors and associated equipment* 483.1–2 (2002), pp. 273–276.

- [5] Peter Hommelhoff et al. “Field emission tip as a nanometer source of free electron femtosecond pulses”. In: *Physical review letters* 96.7 (2006), p. 077401.
- [6] Erik Quinonez, Jonathan Handali, and Brett Barwick. “Femtosecond photoelectron point projection microscope”. In: *The Review of scientific instruments* 84.10 (2013), p. 103710.
- [7] M Zolotarev, E D Commins, and F Sannibale. “Proposal for a quantum-degenerate electron source”. In: *Physical review letters* 98.18 (2007), p. 184801.
- [8] B J Claessens et al. “Ultracold electron source”. In: *Physical review letters* 95.16 (2005), p. 164801.
- [9] O L Krivanek et al. “An electron microscope for the aberration-corrected era”. In: *Ultramicroscopy* 108.3 (2008), pp. 179–195.
- [10] Ondrej L Krivanek et al. “Vibrational spectroscopy in the electron microscope”. In: *Nature* 514.7521 (2014), pp. 209–212.
- [11] Ahmed H Zewail. *Femtochemistry: ultrafast dynamics of the chemical bond*. Vol. 1. World Scientific, 1994.
- [12] Majed Chergui and Ahmed H Zewail. “Electron and X-Ray Methods of Ultrafast Structural Dynamics: Advances and Applications”. In: *ChemPhysChem* 10.1 (2009), pp. 28–43.
- [13] Pierre F Maldague. “Optical spectrum of a Hubbard chain”. In: *Physical Review B* 16.6 (1977), p. 2437.
- [14] W Stephan and P Horsch. “Optical properties of one-and two-dimensional Hubbard and tJ models”. In: *Physical Review B* 42.13 (1990), p. 8736.
- [15] F Carbone et al. “A perspective on novel sources of ultrashort electron and X-ray pulses”. In: *Chemical Physics* 392.1 (2012), pp. 1–9.
- [16] Henry N Chapman et al. “Femtosecond diffractive imaging with a soft-X-ray free-electron laser”. In: *Nature Physics* 2.12 (2006), pp. 839–843.

- [17] JB Rosenzweig et al. “Generation of ultra-short, high brightness electron beams for single-spike SASE FEL operation”. In: *Nuclear Instruments and Methods in Physics Research Section A: Accelerators, Spectrometers, Detectors and Associated Equipment* 593.1 (2008), pp. 39–44.
- [18] Y Ding et al. “Measurements and simulations of ultralow emittance and ultrashort electron beams in the linac coherent light source”. In: *Physical review letters* 102.25 (2009), p. 254801.
- [19] Giulia Fulvia Mancini et al. “Design and implementation of a flexible beamline for fs electron diffraction experiments”. In: *Nuclear Instruments and Methods in Physics Research Section A: Accelerators, Spectrometers, Detectors and Associated Equipment* (2012).
- [20] Bradley J Siwick et al. “An atomic-level view of melting using femtosecond electron diffraction”. In: *Science* 302.5649 (2003), pp. 1382–1385.
- [21] Ramani K Raman et al. “Direct observation of optically induced transient structures in graphite using ultrafast electron crystallography”. In: *Physical review letters* 101.7 (2008), p. 077401.
- [22] M Aidelsburger et al. “Single-electron pulses for ultrafast diffraction”. In: *Proceedings of the National Academy of Sciences* 107.46 (2010), pp. 19714–19719.
- [23] T Van Oudheusden et al. “Compression of subrelativistic space-charge-dominated electron bunches for single-shot femtosecond electron diffraction”. In: *Physical review letters* 105.26 (2010), p. 264801.
- [24] P Musumeci et al. “Capturing ultrafast structural evolutions with a single pulse of MeV electrons: Radio frequency streak camera based electron diffraction”. In: *Journal of Applied Physics* 108.11 (2010), pp. 114513–114513.
- [25] JB Hastings et al. “Ultrafast time-resolved electron diffraction with megavolt electron beams”. In: *Applied physics letters* 89.18 (2006), pp. 184109–184109.

- [26] M Eichberger et al. “Femtosecond streaking of electron diffraction patterns to study structural dynamics in crystalline matter”. In: *Applied Physics Letters* 102.12 (2013), pp. 121106–121106.
- [27] D Fausti et al. “Light-induced superconductivity in a stripe-ordered cuprate”. In: *science* 331.6014 (2011), pp. 189–191.
- [28] Barbara Mansart et al. “Coupling of a high-energy excitation to superconducting quasiparticles in a cuprate from coherent charge fluctuation spectroscopy”. In: *Proceedings of the National Academy of Sciences* 110.12 (2013), pp. 4539–4544.
- [29] Barbara Mansart et al. “Evidence for a Peierls phase-transition in a three-dimensional multiple charge-density waves solid”. In: *Proceedings of the National Academy of Sciences* 109.15 (2012), pp. 5603–5608.
- [30] Fabrizio Carbone et al. “Structural preablation dynamics of graphite observed by ultrafast electron crystallography”. In: *Physical review letters* 100.3 (2008). See also [67] and [68], p. 035501.
- [31] M Harb et al. “Picosecond dynamics of laser-induced strain in graphite”. In: *Physical Review B* 84.4 (2011), p. 045435.
- [32] Fabrizio Carbone, Oh-Hoon Kwon, and Ahmed H Zewail. “Dynamics of chemical bonding mapped by energy-resolved 4D electron microscopy”. In: *Science* 325.5937 (2009), pp. 181–184.
- [33] J Kanasaki et al. “Formation of sp^3 -Bonded Carbon Nanostructures by Femtosecond Laser Excitation of Graphite”. In: *Physical review letters* 102.8 (2009), p. 087402.
- [34] Angela Acocella, Fabrizio Carbone, and Francesco Zerbetto. “Quantum Study of Laser-Induced Initial Activation of Graphite-to-Diamond Conversion”. In: *Journal of the American Chemical Society* 132.35 (2010), pp. 12166–12167.
- [35] J Lorenzana and G Seibold. “Dynamics of metallic stripes in cuprates”. In: *Physical review letters* 90.6 (2003), p. 066404.

Chapter 4. Perspectives in ultrafast electron microscopy

- [36] S Uchida et al. “Optical spectra of $\text{La}_{1-2x}\text{Sr}_x\text{CuO}_4$: Effect of carrier doping on the electronic structure of the CuO_2 plane”. In: *Physical Review B* 43.10 (1991), p. 7942.
- [37] S Sugai et al. “Carrier-density-dependent momentum shift of the coherent peak and the LO phonon mode in p-type high- T_c superconductors”. In: *Physical Review B* 68.18 (2003), p. 184504.
- [38] Luuk JP Ament et al. “Resonant inelastic x-ray scattering studies of elementary excitations”. In: *Reviews of Modern Physics* 83.2 (2011), p. 705.
- [39] G Campi et al. “TEMPERATURE AND X-RAY ILLUMINATION EFFECTS IN OXYGEN DOPED La_2CuO_4 ”. In: *International Journal of Modern Physics B* 17.04n06 (2003), pp. 836–841.
- [40] Luca Piazza et al. “Ultrafast structural and electronic dynamics of the metallic phase in a layered manganite”. In: *Structural Dynamics* 1.1 (2013), p. 014501.
- [41] L Piazza et al. “Design and implementation of a fs-resolved transmission electron microscope based on thermionic gun technology”. In: *Chemical Physics* 423 (2013), pp. 79–84.
- [42] Ahmed H Zewail. “Four-dimensional electron microscopy”. In: *Science* 328.5975 (2010), pp. 187–193.
- [43] <http://www.elettra.trieste.it/FERMI/index.php?n=Main.Machine>.
- [44] https://www.xfel.eu/overview/facts_and_figures/.
- [45] SJ Pennycook and DE Jesson. “High-resolution incoherent imaging of crystals”. In: *Physical review letters* 64.8 (1990), p. 938.
- [46] FO Kirchner et al. “Coherence of femtosecond single electrons exceeds biomolecular dimensions”. In: *New Journal of Physics* 15.6 (2013), p. 063021.
- [47] WJ Engelen et al. “High-coherence electron bunches produced by femtosecond photoionization”. In: *Nature communications* 4 (2013), p. 1693.

-
- [48] AJ McCulloch et al. “High-coherence picosecond electron bunches from cold atoms”. In: *Nature communications* 4 (2013), p. 1692.
 - [49] Ernst Fill et al. “Sub-fs electron pulses for ultrafast electron diffraction”. In: *New Journal of Physics* 8.11 (2006), p. 272.
 - [50] T Van Oudheusden et al. “Electron source concept for single-shot sub-100 fs electron diffraction in the 100 keV range”. In: *Journal of Applied Physics* 102.9 (2007), pp. 093501–093501.
 - [51] Shigeki Tokita et al. “Single-shot femtosecond electron diffraction with laser-accelerated electrons: Experimental demonstration of electron pulse compression”. In: *Physical review letters* 105.21 (2010), p. 215004.
 - [52] Krzysztof P. Grzelakowski and Rudolf M. Tromp. “Temporal and lateral electron pulse compression by a compact spherical electrostatic capacitor”. In: *Ultramicroscopy* 130.0 (2013), p. 36.
 - [53] Meng Gao et al. “Mapping molecular motions leading to charge delocalization with ultrabright electrons”. In: *Nature* 496.7445 (2013), pp. 343–346.
 - [54] Robert P Chatelain et al. “Ultrafast electron diffraction with radio-frequency compressed electron pulses”. In: *Applied Physics Letters* 101.8 (2012), pp. 081901–081901.
 - [55] BW Reed et al. “Solving the accelerator-condenser coupling problem in a nanosecond dynamic transmission electron microscope”. In: *Review of Scientific Instruments* 81.5 (2010), pp. 053706–053706.
 - [56] L Piazza et al. “A proposal for fs-electron microscopy experiments on high-energy excitations in solids”. In: *Micron* 63 (2014), pp. 40–46.
 - [57] MJG Cottet et al. “Quantitative imaging of flux vortices in the type-II superconductor MgB₂ using cryo-Lorentz transmission electron microscopy”. In: *Physical Review B* 88.1 (2013), p. 014505.
 - [58] TE Stevens, J Kuhl, and R Merlin. “Coherent phonon generation and the two stimulated Raman tensors”. In: *Physical Review B* 65.14 (2002), p. 144304.

- [59] http://henke.lbl.gov/optical_constants/filter2.html.
- [60] M. O. Krause. “Atomic radiative and radiationless yields for K and L shells”. In: *Journal of Physical and Chemical Reference Data* 8.2 (1979), pp. 307–327.
- [61] Axel Winter. “Synchronization of Femtosecond Pulses”. In: *Proceedings of the 27th International Free Electron Laser Conference*. Stanford, California, 2005.
- [62] Jungwon Kim et al. “Drift-free femtosecond timing synchronization of remote optical and microwave sources”. In: *Nature Photonics* 2.12 (2008), pp. 733–736.
- [63] R Riedel et al. “Single-shot pulse duration monitor for extreme ultraviolet and X-ray free-electron lasers”. In: *Nature communications* 4 (2013), p. 1731.
- [64] CM Scoby et al. “Electro-optic sampling at 90 degree interaction geometry for time-of-arrival stamping of ultrafast relativistic electron diffraction”. In: *Physical Review Special Topics-Accelerators and Beams* 13.2 (2010), p. 022801.
- [65] M Gao et al. “Single shot time stamping of ultrabright radio frequency compressed electron pulses”. In: *Applied Physics Letters* 103.3 (2013), p. 033503.
- [66] GJH Brussaard et al. “Direct measurement of synchronization between femtosecond laser pulses and a 3 GHz radio frequency electric field inside a resonant cavity”. In: *Applied Physics Letters* 103.14 (2013), p. 141105.
- [67] Hyuk Park and Jian-Min Zuo. “Comment on Structural Preablation Dynamics of Graphite Observed by Ultrafast Electron Crystallography”. In: *Phys. Rev. Lett.* 105 (5 2010), p. 059603. DOI: 10.1103/PhysRevLett.105.059603. URL: <http://link.aps.org/doi/10.1103/PhysRevLett.105.059603>.

- [68] Fabrizio Carbone et al. “Erratum: Structural Preablation Dynamics of Graphite Observed by Ultrafast Electron Crystallography [Phys. Rev. Lett., 035501 (2008)]”. In: *Phys. Rev. Lett.* 106 (13 2011), p. 139901. DOI: 10.1103/PhysRevLett.106.139901. URL: <http://link.aps.org/doi/10.1103/PhysRevLett.106.139901>.

Conclusions

This doctoral work was dedicated to the installation of a laboratory of ultrafast microscopy at the École Polytechnique Fédérale de Lausanne. After the installation of the transmission electron microscope by the manufacturer's company, in collaboration with IDES we proceeded to do the necessary hardware modifications, interfacing the column and the gun of the microscope with the ultrafast laser setup. After the necessary optimization and fine tuning we demonstrated the capability of reaching an energy resolution of about 1 eV and a time-resolution of about 300 fs. The possibility of controlling independently the voltage applied to the Wehnelt cylinder and the excitation of the C0 lens proved to be an effective way for increasing the brightness of the instrument.

Several operational modes are available for static and stroboscopic measurements, and their complementarity allows to effectively study strongly correlated materials. We analyzed a $\text{PrSr}_{0.2}\text{Ca}_{1.8}\text{Mn}_2\text{O}_7$ sample, a layered manganite, and we reported direct observations of the interplay between the lattice and the electronic structure of the crystal. The coherence of the pulsed electron beam resulted to be sufficient for the studies in the metallic phase of the compound, while the characterization of the charge ordering dynamics using ultrafast diffraction will require some further optimization in the gun region of the microscope.

Ultrafast energy-filtered PINEM demonstrated to be a flexible technique for studying several categories of nanostructures. Focusing on a sample of silver

Conclusions

nanowires, we demonstrated the possibility of controlling the spatial configuration of the photo-induced near-field obtaining results in agreement with numerical simulations. Furthermore, exploiting the characteristics of a post-column energy filter we demonstrated the possibility of acquiring simultaneous information about particle-like and wave-like behavior of a surface plasmon-polariton.

Finally we discussed the feasibility of using ultrashort X-ray pulses as the source of photo-excitation for solid state samples. Imagining a facility that provides to the user such a broad range of wavelength would notably expand the field of application of this technique.

CURRICULUM VITÆ

LUCA PIAZZA

PERSONAL DATA

CURRENT POSITION

Laboratory for Ultrafast Microscopy
and Electron Scattering (LUMES)

Ecole Polytechnique Fédérale
de Lausanne (EPFL)

ADDRESS

EPFL campus
CHH2 555, Station 6
1015 – Lausanne
Switzerland



CONTACT

+41 764 35 03 82
luca.piazza@epfl.ch
piazza.luca@gmail.com

EDUCATION

PhD in Chemistry and Chemical Engineering — Swiss Federal Institute of Technology in Lausanne (EPFL, Switzerland)

Master degree in Condensed Matter Physics — University of Trieste (Italy)

Bachelor degree in Physics — University of Trieste (Italy)

RESEARCH EXPERIENCE

PhD in Ultrafast Electron Microscopy, prof. Fabrizio Carbone, EPFL, Lausanne.

The first part of the thesis has been devoted to setting up a laboratory for Ultrafast Electron Microscopy. After preparing the proper infrastructures's facilities an ultrafast Ti:Sapph Laser/Amplifier (Wyvern-X, KMLabs) and a commercial transmission electron microscope (Jeol JEM 2100) have been installed. A series of custom hardware modifications allowed the integration of the optical setup within the microscope enabling time-resolved imaging, electron diffraction and electron energy loss spectroscopy. To contemporary control the existing functionalities of the microscope and the parameters of the drive laser we developed with Matlab a user-friendly graphical user interface capable of controlling the experimental data acquisition and performing live data analysis.

In a second phase the Ultrafast Electron Microscope has been completely characterized to optimize temporal and spatial resolution of the microscope and the energy resolution of the electron energy loss spectrometer.

Once commissioned, the machine has been used to study several materials of scientific interest, strongly correlated electron systems, superconductors and metallic nanostructures.

Internship in the Laser Group of FERMI@Elettra, dott. Miltcho Danailov, Elettra, Trieste.

The subject of the project was related to studies of balanced optical cross-correlator for phaselocking of ultrafast laser oscillators which were under development at the FERMI@Elettra laser laboratory. This included work on setting up and testing different balanced optical schemes, characterization of their performance and completion of the related driving and control electronics. The set-up included both bulk and fiber optical components. The Matlab software needed to control the operations of the cross-correlator delay and perform live data acquisition has been successfully implemented.

Master degree in Condensed Matter Physics, prof. Fulvio Parmigiani, T-ReX, Trieste.

The project was focused on the commissioning and the characterization of a sub-ps X-ray Streak Camera (Hamamatsu Photonics). This is a diagnostic component of the X-ray Free Electron Laser FERMI@Elettra and is able to measure the pulse length of single X-ray pulses with high temporal resolution. An ultrafast Ti:Sapph laser has been used to characterize the machine, together with a compact HHG source assembled for this purpose.

Bachelor degree in Physics, prof. Silvio Modesti, TASC, Trieste.

I worked on the characterization of self-assembled semiconducting quantum dots samples differently doped. We used Cross-sectional Scanning Tunneling Microscopy (XSTM) to observe the distribution profile of the dopant atoms in the material.

TEACHING EXPERIENCE

- General Physics I (Bachelor in Civil Engineering), prof. Fabrizio Carbone
- General Physics II (Bachelor in Biology), prof. Tran Minh Tâm
- General Physics II (Bachelor in Civil Engineering), prof. Fabrizio Carbone
- General Physics I (Bachelor in Civil Engineering), prof. Davor Pavuna
- Advanced Physics II (Bachelor in Physics), prof. Ansermet Jean-Philippe

ACADEMIA

Articles

- *Principles and Implementation of an Ultrafast Transmission Electron Microscope*, **L. Piazza**, M. Cottet, D.J. Masiel, T. LaGrange and F. Carbone, *Proceedings of Microscopy & Microanalysis*, 18 (Suppl 2), 2012
- *Design and implementation of a fs-resolved transmission electron microscope based on thermionic gun technology*, **L. Piazza**, D.J. Masiel, T. LaGrange, B.W. Reed, B. Barwick, F. Carbone, *Chemical Physics*, 423 79–84, 2013
- *Ultrafast structural and electronic dynamics of the metallic phase in a layered manganite* **L. Piazza**, C. Ma, H. X. Yang, A. Mann, Y. Zhou, J. Q. Li, F. Carbone, *Structural Dynamics*, 1 014501, 2014
- *A proposal for fs-electron microscopy experiments on high-energy excitations in solids*, **L. Piazza**, P. Musumeci, O.J. Luiten, F. Carbone, *Micron*, 63 40–46, 2014
- *Simultaneous observation of the quantization and the interference pattern of a plasmonic near-field*, **L. Piazza**, T.T.A. Lummen, E. Quinonez, Y. Murooka, B.W. Reed, B. Barwick, F. Carbone, **Nature Communications**

Seminars and Conferences

- Invited seminar at the conference "Microscopy and Microanalysis", Phoenix, USA, Aug 2012
- Invited seminar at the conference "European Microscopy Congress", Manchester, UK, Sep 2012
- Invited seminar at the workshop "Cercle des Microscopiste JEOL", Poitiers, France, Mar 2013
- Seminar on Condensed-Matter Physics, EPFL Lausanne, Switzerland, Apr 2013
- Invited seminar at ELETTRA, Sincrotrone Trieste, Italy, Oct 2013
- Contributed seminar at the conference FEIS, Kew West, USA, Dec 2013
- Invited seminar at the workshop "Cercle des Microscopiste JEOL", Lille, France, Apr 2014

REFERENCES

Prof. Fabrizio Carbone
Laboratory for Ultrafast Microscopy and Electron Scattering
Faculty of Basic Sciences
École Polytechnique Fédérale de Lausanne
EPFL campus, CHH2 595, Station 6
1015 Lausanne
Switzerland
fabrizio.carbone@epfl.ch
+41 216 930 562

Prof. Fulvio Parmigiani
University of Trieste
Elettra Sincrotrone Trieste
S.S. 14, Km 163.5 in Area Science Park
34012 Basovizza, Trieste
Italy
fulvio.parmigiani@elettra.eu
+39 040 375 8428

Dr. Marco Zangrando
BACH - Beamline for Advanced diCHroism
FERMI@Elettra Optics group
S.S. 14, Km 163.5 in Area Science Park
34012 Basovizza, Trieste
Italy
marco.zangrando@elettra.trieste.it
+39 040 375 8401